Transient Oscillation Control Strategy for Type-4 Wind Turbines in Weak Grids

by

Hae Yeol Min

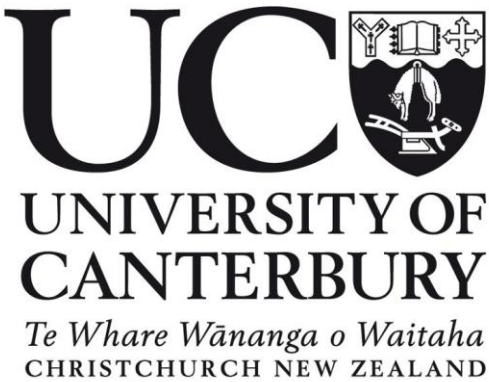

A thesis submitted to
The Department of Mechanical Engineering
in partial fulfilments of
the requirements for the degree of
Doctor of Philosophy
at
The University of Canterbury,
Christchurch, New Zealand

September 2019

CONTENTS

List of Figures

List of Tables

List of Symbols and Abbreviations

$\dot{x}_\iota$	a set of the system states
$f_i(\cdot)$	a particular function of the system
A	a system matrix
x	a set of state variables
u	an system input
v_{DC}	DC voltage
v_{abc}	grid voltage
i_{abc}	grid current
v_{dq}	transformed voltage in dq-frame
i_{dq}	transformed current in dq-frame
v_s	stator voltage of PMSG terminal
i_s	stator current of PMSG terminal
C_{dc}	Capacitance of DC-link capacitance
v_{Cdc}	DC-link capacitor voltage
R_{dc}	lump resistance of DC-link circuit
τ_{dc}	time constant of DC-link capacitor
I_{wt}	wind turbine rotor inertia
I_{pm}	generator inertia
T_{wt}	wind turbine torque
$T_{\mathrm{wt,fr}}$	force of friction of wind turbine rotor
T_{sh}	shaft torque
T_{pm}	electromagnetic torque of PMSG
$T_{\mathrm{pm,fr}}$	force of friction of PMSG
C_{sh}	coefficient of shaft stiffness
D_{wt}	coefficient of wind turbine damping
D_{pm}	coefficient of PMSG damping
D_{sh}	coefficient of shaft damping
θ_{wt}	position (angle) of wind turbine rotor
θ_{pm}	position (angle) of PMSG rotor
ω_{ar}	angular frequency of anti-resonant oscillation mode

ω_r	angular frequency of resonant oscillation mode
ω_s	synchronous rotor speed of PMSG
R_s	stator resistance
ψ_{pm}	flux linkage by permanent magnet
ψ_{sd}	flux linkage of d-axis
ψ_{sq}	flux linkage of q-axis
L_{sd}	inductance of d-axis
L_{sq}	inductance of q-axis
L_{sm}	stator mutual inductance
R_{sm}	stator mutual resistance
$\boldsymbol{z}(i)$	measured voltage vector
$\boldsymbol{H}(\cdot)$	a relation function between the state and the measurement value
$\boldsymbol{w}_m(i)$	additive white Gaussian noise
$\boldsymbol{Q_m}(i)$	covariance matrix
$w(t)$	cross-correlation function of signals in time-domain
$\boldsymbol{u}(i)$	control input vector
v_{dq_syn}	synthesised input vector of voltage
i_{dq_syn}	synthesised input vector of current
WT	wind turbine
WTG	wind turbine generator
PMSG	permanent magnet synchronous generator
DFIG	doubly-fed induction generator
EM	electromagnetic
EKF	extended Kalman filter
UKF	unscented Kalman filter
VSI	voltage source inverter
MSC	machine-side converter
PLL	phase-locked loop
SCR	short-circuit ratio
SSR	sub-synchronous resonance
SSCI	sub-synchronous control interaction
MPPT	maximum power point tracking

ABSTRACT

This thesis describes the transient oscillation control strategy developed for wind turbine systems interconnected to a weak grid, which can cause nonlinear oscillations during the post-fault period.

Problems with existing wind turbine system modelling and their control structures are analysed. The first problem is the power balance equation (PBE) used in the WT system modelling, which fails to describe the transient condition of the isolated AC and DC operating condition. The second problem is the conventional feedback control input based on the WT system model, which is based on the PBE, resulting in sub-synchronous control interactions and system oscillations.

Recently, many sub-synchronous control interaction (SSCI) cases have been found between the electronic components with their controllers in Type-3 doubly-fed induction generator (DFIG) based wind turbines with a series compensated transmission lines. The impact of SSCI problems has been escalated since the Electric Reliability Council of Texas (ERCOT) event of 2009, where a faulted transmission line and subsequent outage kept the 450 MW DGIF based wind farm radially connected into a series compensated network. It caused a massive DFIG wind farm failure and series capacitor damage due to the oscillation build-up after the fault was cleared. In addition, the wind farm experienced crowbar failure due to the increase in this current oscillation in DC-link circuits. Therefore, there is an urgent need to mitigate these oscillation problems.

The wind turbine system modelled in this thesis is for the two-port based modular structure of wind turbine (WT) systems. The input values of each module are inherited from the previous module, which eliminates all assumptions of the input conditions, except wind speed. The mechanical system model is validated with torsional oscillation (TO) cases, and the electrical system model is validated with SSCI cases.

The new control strategy developed in this thesis consists of: (1) a transient model of DC-link during a grid fault; (2) cross-correlation to estimate the time-delay between the grid and generator voltages; and (3) the Kalman filter for estimating the voltage and the angle of the

PMSG. These modelling and control formulation methods are outlined, and the proposed control strategy is presented. A three-phase fault is applied in the simulation to demonstrate the ability to mitigate the system oscillation during the post-fault period. In addition, the voltage characteristics of the DC-link capacitor response are examined with, and without, crowbar protection. Control performance is simulated with MATLAB/SIMULINK and justified with another well-documented WT system with the SSCI problem via three-phase grid fault simulations.

The overall outcome is a modelling and control methodology for an increasingly new WT technology. The approach is generalisable to other WT types and systems. As reliance on WTs and wind energy increases, the problems addressed in this thesis will be increasingly common, and demand solutions like those presented here.

ACKNOWLEDGEMENTS

I sincerely thank my supervisors, Prof. Geoffrey Chase (University of Canterbury, New Zealand) and Prof. Xiaoqi Chen (Swinburne University of Technology, Australia) for their valuable guidance, constructive advice and support during the course of this research.

Finally, I would like to express my deepest appreciation and love to my family for their support and encouragement.

Don't put yourself down. You're truly unique, just like everyone else.

1
INTRODUCTION

Wind power is one of the fastest-growing sources of renewable energies in the world. Wind turbine modelling is the essential tool and foundation for analysis, design, optimasation, and control of these complete systems. Wind turbine systems are very different from conventional generation plants in which the wind cannot be controlled. More specifically, the system is driven by a noise-like input in which the instantaneous wind speed determines the point of wind turbine operation. In addition, the wind turbine (WT) is interconnected to a grid, which brings in further nonlinear dynamics. These factors make wind turbine systems substantially different from most traditional power systems [1].

1.1 Overview

This thesis looks at grid-connected converter systems in WT applications. When the WT system is operating in the steady-state, the behaviour of the system is deterministic [25]. However, when the system experiences specific large perturbations, whether caused by electrical or mechanical disturbances, or a combination of both, the behaviour of the system may have nonlinear characteristics, which may lead to the system becoming unstable [18]-[20]. In this case, small-signal based stability prediction methods may, or may not, satisfactorily predict system stability, depending on the control limit and capability of the wind turbine system [26]-[29].

Many wind farm failures are related to large-signal disturbances, which introduces more significant interactions between system components and other interconnected synchronous systems [18], [20], [28], [30]. The definitions of a small disturbance and large disturbance are important and defined [31]:

A ***small disturbance*** is a disturbance for which the set of equations describing the power system may be linearised for system analysis.

A ***large disturbance*** is a disturbance for which the equations describing the power system cannot be linearised for system analysis. Large disturbances are usually referred to as "transient [32]."

For analysing the stability of large-signal disturbances, transient stability analysis should be performed, because controllers are designed for local components and are not designed to handle large disturbances, such as grid faults.

1.2 Industry Drive

Unplanned system shutdown represents one of the main cost drivers of any grid-connected wind farm [13], [14]. If a wind farm experienced severe disturbances or other unidentified problems, it usually ends up with a series of exhausting lawsuits between the electricity consumer, wind farm owner, operator, and grid owner for the cost and losses. Reliability analysis and scheduled maintenance only reduce the fundamental problem, rather than providing a corrective solution.

Historical failure and downtime data of over 4300 wind turbines ranging between 300 kW, and 3 MW is presented by Reder et al. [2] from the Technical Research Centre of Finland (VTT)

data [3]. However, the author does not discuss nor identify underlying causes, such as grid faults or other large disturbances, to these wind turbine component breakdowns. It is mainly because the transmission system operator (TSO) keeps its power system event logs in a confidential manner, which is not accessible. This non-disclosure makes it very difficult for researchers and engineers to analyse the correlation between large disturbances, wind turbine components, and the apparent effects or falures.

Model development of relatively newer WTs, such as a Type 4 direct-drive WT system with full power converters, makes it very difficult to analyse the effect of faults on both the grid and the WT sides. The existing modelling method for this Type 4 WT does not accurately describe the dynamics of the WT and control systems, but it also has much more complex fault response characteristics governed by the proprietary controls of the back-to-back converters and WT generator [4], [5]. From a system control and protection point of view, it is essential to model a system that including realistic WT models with large signal behaviours, which how these WT systems are affected by different events or faults. However, almost all real-world WT models are manufacturer-specific and proprietary in most cases. Even for the same WT models from, significantly different control parameters or algorithms may be employed across WT systems.

The National Renewable Energy Laboratory (NREL) released a report on subsystem reliability of wind turbine components [6]. This report is based on the database obtained from various private and public sectors from different countries [7]-[11] and different manufacturers. This report indicates the average number of failures occurring in the control systems was about 12% per wind turbine, and the average downtime per failure is ~1.5 hours.

In Denmark, Technical University of Denmark (DTU) and Risø National Laboratory (RNL) released an analytical report after 13 years of a survey called, "*Mapping of grid faults and grid codes*" [12], based the grid faults and their impacts on the grid-connected wind turbine. The report identified grid-connected wind turbines are more frequently subjected to grid faults. Although it does not mention specifically which wind farms experienced losses due to grid faults, various grid faults, such as single- or three-phase faults, can occur any part of the grid. These faults are mostly associated with short-circuits and transient voltages. They are either symmetrical or unsymmetrical [55] and characterised by the magnitude of the transient voltage [3] and by the time duration of the fault [6]. The evaluation of grid faults, and their impact on WT systems and distribution loads requires a shared understanding of the grid fault types and their frequency change [24].

A mapping of grid faults in different countries is provided in [12], [13]. In this report, statistics regarding the grid faults in the grid of the Nordic European countries, Norway, Denmark, Finland, and Sweden, are presented and analysed. According to the report, the most common faults per year in the period 2000 to 2005 are located on transmission lines. During this period, the single-phase fault type had the highest probability of occurrence compared with other fault types [14]. However, the three-phase grid fault has the most significant impact on the WT system, causing large downtimes [24]. Further studies on grid faults and wind turbine system support the results of this investigation [14].

1.3 Large Disturbances in Wind Farm

Large disturbances in wind farms are due to faults on either the grid or the generator side. When faults occur, protection systems are activated to avoid any penetration of short-circuit current to other subsystems by isolating only the components under fault, while leaving as much of the network as possible still in operation. The typical duration of faults are 100 to 200 ms, but it can be as long as several seconds [15].

Large disturbances or transients are severe faults, such as three-phase short-circuits on the transmission network [19]. In wind farms with weak grid interconnection, voltage and current oscillation problems have been observed in the post-fault stage [16], [17]. Interestingly, the sub-synchronous control interaction (SSCI) was also observed during a fault, although the author did not specify what type of fault it was [18]. More details about the weak grid are described in Chapter 3.

The transient response initiated by these severe faults involves electromechanical interactions and control interactions mentioned in sub-synchronous resonance problems. The system behaviour of the transient response is very complex to analyse. From a system point of view, transient response and stability is a highly nonlinear and boundary problem [19], [33], [34]-[36]. Conventional small-signal modelling and stability analysis methods used by the majority of the power electronics community cannot describe such nonlinear phenomena [37].

In modern transmission and distribution systems, an automatic recloser operated by protective relays is commonly used to attempt to restore the system operating condition in the event of a fault. This automatic recloser has become more common on wind farms as more wind farms are connected to the grid [38]. Thus, there is an urgent need for full system models to analyse

and optimise these nonlinear dynamics during grid faults to optimise WT and wind farm performance.

1.4 Motivation

Current modelling methods of WT systems allows the input of the individual module to be assumed, such as all these control methods assume the DC-link voltage is constant, which is controlled by the grid voltage [55]-[64]. In real WT systems, the DC-link voltage is always fluctuating even though the magnitude of the fluctuation may be very small. It lacks the inherited property of the input condition, such as oscillation from the previous module. The loss of inherited property in the system model causes two main problems: (1) untraceable system behaviours during the transient oscillation, where the magnitude of the oscillation exceeds the operating range, and (2) the uncertainty of their control performance.

1.5 Objectives

The aim of this research is to: 1) develop a transient model of the DC-link; and 2) develop a transient oscillation control strategy for type-4 WT system applications.

1.6 Contributions

The main contributions of this thesis can be summarised in two groups:

I. A novel DC-link circuit model describing inherited current and voltage dynamics from wind turbine generators

a) *Modelling and analysis of the WT system platform*

As the basic, yet most fundamental component of the thesis, electrical system modelling and analysis of a DC-link dynamics as an inherited platform from both the wind turbine generator and the grid is proposed. The DC-link design process is presented in an unconventional way, with wind farm connected to a weak grid, with non-constant DC-link voltage and current inherited from the WT generator, and with the isolated grid from the voltage source inverter (VSI) during grid faults. The DC-link system is analysed using MATLAB & SIMULINK® software in the design process to validate the optimum system to be controlled.

b) *Simulation*

The simulation of the WT systems interconnected to a weak grid, aiming for offline analysis and system performance during large-signal disturbances is investigated. For this purpose, the platform is modelled and simulated based on the real physical parameters of the WT systems using MATLAB & SIMULINK®. The fault ride-through capability problem associated with the WT model-based linear control system is discussed.

In addition, the control interaction between the VSI and WTG, and how it governs the ride-through capability of the WT systems in terms of post-fault conditions of three-phase balanced faults, is discussed. The control interaction in the DC-link capacitor is introduced in the form of mathematical and electrical circuit representations without small-signal assumptions that DC quantities (current and voltage) are constant. Since no small-signal assumption is made, various operating points of the WT system states are estimated by using a Kalman filter.

Simulation of the real-world environment, physical model, sensor locations, and control system are achieved in MATLAB & SIMULINK. The new control strategy is formulated, simulated, and validated concerning the real-system parameter-based model. Exact modelling and simulation allow efficient and accurate development, testing, and validation of the WT system before implementation on real systems.

II. Novel control method with synthesised input signal

The control of VSI is an essential part of WT systems as an interface instability problem after relatively longer grid faults of over 100~120ms. In this thesis, a control strategy to prevent the system instability due to induced oscillation has been proposed to achieve traceable control responses and prescribed oscillation behaviours to mitigate stability problems. The new control input is defined based on the measurable system parameters of WT systems, rather than average linear or typical linear WT models.

Simulations have been performed to validate the result using wind turbine system modelling [20], [39]-[44]. Control performance is improved during the post-fault system condition compared to the conventional linear controls used these days [45]-[48].

Transient instability in a wind farm is perhaps one of the least probable, yet most severe, event any power system can encounter during operation. It may cause unintentional system islanding/disconnection from the grid, multiple outages in different locations and even

wide-spread blackouts [21], [22], [49]-[51]. One of the main reasons to control the WT transient instability problem is to determine the critical clearing time (CCT) for specified fault conditions at a pre-fault stage and predict wind farm stability. If the calculated CCT is longer than the time required by protection relays, the system can lose synchronisation. If so, the coordination of the relays, loads, and generators can be adjusted to increase the system stability margin.

The control strategy to mitigate system oscillations for VSI and WTG after grid faults can be considered the most significant contribution of this thesis. However, modelling the platform to duplicate the oscillation phenomena as the base tool of this research is essential to carry out the rest of the research work. Analysis of fluctuating grid voltage penetrating through VSI and PMSG controls to interact with electrical and mechanical counterparts is considered one of the main challenges in wind energy in terms of control system design [52], [53]. It requires utterly different perspectives than those conventional *dq*-frame referenced control structures [4], [23], [27]. The developed control strategy in this thesis can be applied to any existing type-4 WT platform without replacing the existing controllers.

1.7 Thesis Outline

This thesis consists of six chapters. The description of each chapter is provided as the following.

Chapter 1 – ***Introduction***

This chapter briefly presents the problems of existing modelling and control methods of the WT systems. The impact of these modelling and control methods can lead the WT system to severe failures, such as the ERCOT events, is discussed.

Chapter 2 – ***Literature Review***

Existing WT system modelling methods are presented. The main focus of the modelling in the chapter is the back-to-back converter. Also, the overview of available control methods of the back-to-back converters is presented.

Chapter 3 – ***System Modelling***

A complete model of the permanent magnet synchronous generator (PMSG) based Type-4 WT system using the two-port structure is presented in this

chapter. The new model of a transient DC-link, which is described only with DC parameters, is also presented.

Chapter 4 – ***Simulation***

The developed WT system model is verified via torsional oscillation (TO) simulation for the mechanical system and sub-synchronous control interaction (SSCI) simulation for the electrical system with its controls. Various system oscillations from the simulation result are discussed.

Chapter 5 – ***Control***

Based on the simulation result in Chapter 4, a new control strategy is proposed. The control strategy is applied to the oscillating WT systems to validate the control performance. In addition, the control is applied to a well-documented doubly-fed induction generator (DFIG) based WT exhibiting the oscillation behaviour.

Chapter 6 – ***Conclusion***

This chapter summarises the objective, contributions, and work presented in this thesis. Also, future works after this thesis work are presented.

1.8 Summary

The problem and its effect of large-signal disturbances in WT systems are outlined in this chapter. Grid faults are prevalent disturbances in a power system in general. It suppresses the grid voltage, and interact with the generators causing oscillations in the WT system and grid. Traditional modelling methods of back-to-back converters and fault-tolerant control algorithms share similar small-signal modelling techniques and control structure to each other. Thus, a new method to mitigate the transient oscillation of the back-to-back converter and its control strategy is proposed.

All simulations in this thesis are in the time-domain with discrete models for computations.

2
LITERATURE REVIEW

Approaches to the mathematical modelling of wind turbine (WT) systems are typically designed on a component-by-component basis, due to the complexity of the system. For the member of physically connected components with many feedback/feed-forward loops, decoupling the WT system into a set of cascaded components is particularly time consuming and complex, because the connectivity of dynamic subsystems imposes many physical limits and mathematical constraints on the multiple variables of the WT system [65]. These restrictions lead to differential-algebraic equations (DAE) for the system model [66], where the differential equations describes the physical characteristics of each component of the system, and the algebraic equations represent the characteristics of the system. The differential equations describing conservation of electro-mechanical energy, Kirchhoff and Ohm's laws governing general behaviours of the component are quite consistent, whereas the algebraic equation describing the system characteristics may not be as consistent as each component. Thus, it complicates the modelling, analysis and design of controls for large WT systems.

2.1 Problem Statement

Conventional linear system analysis and control theory applied component-wise may be locally valid, such as in the proximity of some steady-state system condition or operating point. Characterising the real system structure of physically connected components in the algebraic equation is very difficult. In addition, a large-scale and complexity of interactions between all components used in WT systems, many modelling approaches and techniques are quite inaccurate. Finally, the primary good of modelling WT system is to better understand the impact of significant nonlinear perturbations away from known stable operating points. These issues are significant challenges to be answered in the power system community.

The transmission line or cable impedance has become a vital element between remote wind farm locations and the grid. It leads to changes in the interconnection environment where increasing number of large wind farms are interconnected to weak grids [129]. The weak grid consists of an AC system with a low short-circuit ratio (SCR $\leq$ 5). Thus, the problem is to analyse the behaviour of system interactions under large disturbances.

For instance, the effect of substantial changes in the transmission line system may not be identified on local component dynamic behaviour, such as converter systems. Endo et al. have shown the ill-conditioned voltage from the interconnection node interacts with the locally linearised behaviour of small controlled perturbations and can eventually lead the system to be unstable [66]. Thus, are those situations of practical interest occur when a large disturbance penetrates through subsystems and may induce non-periodic oscillatory behaviour due to uncoordinated control interactions that do not meet physical system requirements, such as PLL and controller saturation.

2.2 Modelling of Type-4 Wind Turbine Systems

The modelling of a complete wind turbine system is extensive and complex, involving various parts of a wind turbine model. These diverse system elements include the WT blades to the rotor, drivetrain, permanent magnet synchronous generator (PMSG), back-to-back converters, and others. The Type-4 WT system model used here is validated via simulations using MATLAB and SIMULINK.

2.2.1 Permanent magnet synchronous generator

A wind farm is a large-scale power system with many electronic and mechanical components operating at different frequencies. The grid operates at 50 Hz, but the generator and turbine

may operate at much lower frequencies. Thus, as larger-scale wind turbines are being developed nowadays, the direct-drive permanent magnet synchronous generator (PMSG) based wind farms and their control algorithms have become a major issue.

In particular, direct-drive PMSG-based wind turbine systems do not have a gearbox. In traditional gearbox-operated wind turbines, the blade rotates a shaft connected through a gearbox to the generator. Direct-drive wind turbine eliminates the second- or higher-order differential equation which is possibly the most complicated part of the machine and the highest maintenance part of the wind turbine system, thus improving reliability. For this reason, the use of direct-drive has been increasing for permanent magnet-based generators. For example, Siemens has made and released their 6 MW direct-drive systems with a permanent magnet synchronous generator [66].

The entire model scheme of modern wind turbine systems using direct-drive PMSG, a back-to-back converter and a drivetrain system is shown in Figure 2.1

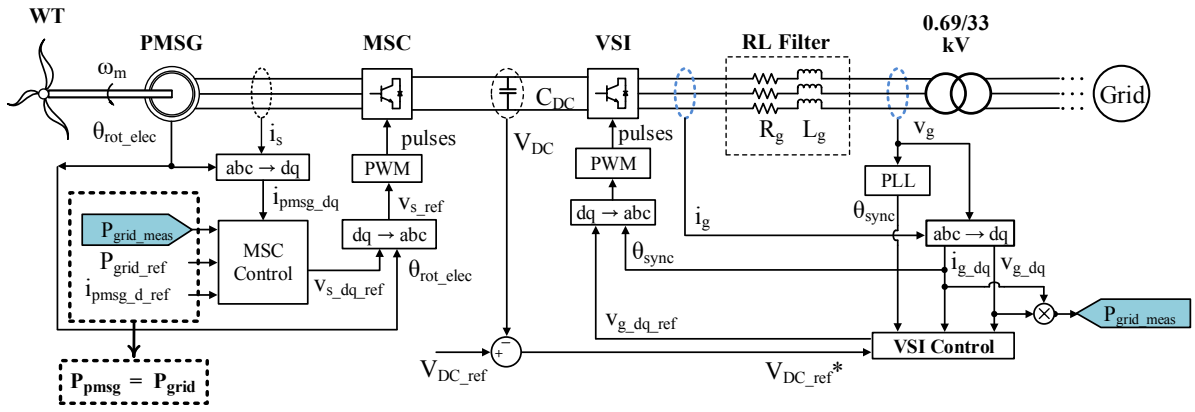

Figure 2.1: Typical components of wind farm branch with direct-drive PMSG based wind turbine generators

The WT converts the wind into the mechanical power by generating the torque, and the PMSG converts the mechanical power into the electrical power. The MSC, either a rectifier or converter, converts the AC voltage from the generator terminal into DC voltage and regulates the speed of the PMSG to control the current. The inverter controls converting the DC voltage to match the grid frequency and voltage level. By controlling the inverter voltage, the active and reactive power injection into the grid can be controlled at the desired level.

2.2.2 Back-to-back converter

The back-to-back converter refers to a set of AC-DC and DC-AC converters with a cascaded connection. Converter operation is based on switching action. During a switching cycle, several switching positions are configured and a set of differential equations are developed based on the circuit configuration and algebraic equations for input-to-output relationships. The exact model of any switching power converter is nonlinear in nature but can be modelled as a set of piecewise linear, as shown in Figure 2.2.

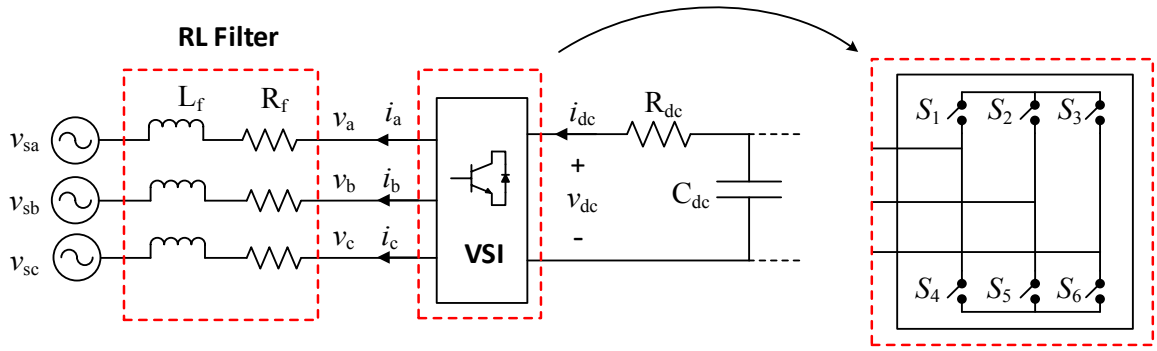

Figure 2.2: The basic three-phase VSI circuit

Different power converters have their mathematical models relating to their system dynamics. The differential equation describing the switching converter operation can be written as:

$$\dot{x}_i = f_i(x, u, t), \qquad i = 0, 1, 2, \dots, n \tag{2.1}$$

where $\dot{x}$ represents a set of the system states, which typically are the filter current and voltage, *u(t)* and the subscript *i* denote the system input vector, which can be either voltage or current and the switching position of converter circuits.

At the end of this section, an example of a voltage source converter (VSC) model is provided to clarify how the differential Equation (2.1) describes the converter operation.

Assuming the switching action is ideal, the switching position implies a discrete set of states, which makes the discrete-time analysis methods preferable. For the perfect switching operation, intermittent switching states that increase switching uncertainty are neglected. In addition to the switching operation, nonlinearities arise because semiconductor elements, such as diodes and transistors, are highly nonlinear [130], as are based power electronic components and

passive elements, such as inductors and transformers. In the past, various linear modelling techniques of switching power converters have been developed [92]-[97].

2.2.3 Modelling methods of switching converters

i. state space averaging (SSA)

Middlebrook et al. proposed *a general unified approach to modelling* any particular switching converter called *state space averaging* (SSA) method [67], which is still one of the most widely used modelling and analysis methods for many switching converters these days. SSA characterises the small-signal response at different switching stages of a switching converter in a set of linear time-invariant (LTI) states, as shown in Table 2.1 and 2.2. Each state represents the duty cycle ratio of the switching converter at different voltage levels. Therefore, the complete SSA model is defined by a set of switching states based on the duty cycle ratio of the converter system.

Table 2.1: VOLTAGES AS A FUNCTION OF SWITCHING POSITIONS.

switching position			**line-to-line voltage**			**phase voltage**		
$S_1 = S_4$'	$S_2 = S_5$'	$S_3 = S_6$'	$v_{ab}(t)$	$v_{bc}(t)$	$v_{ca}(t)$	$v_a(t)$	$v_b(t)$	$v_c(t)$
0	0	0	0	0	0	0	0	0
0	0	1	0	$-v_{dc}$	v_{dc}	$-v_{dc}/3$	$v_{dc}/3$	$2v_{dc}/3$
0	1	0	$-v_{dc}$	v_{dc}	0	$-v_{dc}/3$	$2v_{dc}/3$	$-v_{dc}/3$
0	1	1	$-v_{dc}$	0	v_{dc}	$-2v_{dc}/3$	$v_{dc}/3$	$v_{dc}/3$
1	0	0	v_{dc}	0	$-v_{dc}$	$2v_{dc}/3$	$-v_{dc}/3$	$-v_{dc}/3$
1	0	1	v_{dc}	$-v_{dc}$	0	$v_{dc}/3$	$-2v_{dc}/3$	$v_{dc}/3$
1	1	0	0	v_{dc}	$-v_{dc}$	$v_{dc}/3$	$v_{dc}/3$	$-2v_{dc}/3$
1	1	1	0	0	0	0	0	0

Table 2.2: BASIC COMPARISON OF DIFFERENT STATE SPACE MODELLING APPROACHES.

Nonlinear state space	$\dot{x}(t) = f_i(x(t), u(t), t)$ $y(t) = g_i(x(t), u(t), t)$	No linearisation
Linear time-invariant (LTI)	$\dot{x}(t) = Ax(t) + Bu(t)$ $y(t) = Cx(t) + Du(t)$	Linearisation around a single equilibrium point
Linear time-periodic (LTP)	$\dot{x}(t) = A(t)x(t) + B(t)u(t)$ $y(t) = C(t)x(t) + D(t)u(t)$	Linearisation around a single periodic state

ii. generalised state space averaging (GSSA)

Sanders et al. extended the SSA method to a more *generalised state space averaging* (GSSA) in switching converters [72], which can process unrestricted types of waveforms. This method is based on a time-dependent Fourier series expansion on a given waveform for a sliding window. GSSA is extensively used with sliding mode control techniques [131]-[135], which is based on the current state of the switching position. Generally, the GSSA model can be obtained by eliminating higher-order terms in the Fourier series. For example, the GSSA method can capture the low-frequency behaviour of a switching converter by retaining only the DC coefficients, and eliminating insignificant all other terms. The result of the GSSA method reduces the limitation of SSA [98].

Later, Lehmann et al. pointed out the drawbacks of the SSA model by including the "switching frequency effects", such as harmonics due to switching transients, into the conventional average converter model [73]. These transient terms are described with a second-order polynomial term, which corrects the DC offset error and thus, improves "the accuracy of the closed-loop stability and performance of the SSA method [73]." This approach provides clarification on the relationship between the original switching converter and the average model by approximating the solution of the switching converter using Fourier series within an arbitrary accuracy. This modelling method accommodates PWM converters very well because it relates to the duty cycle ratio of the switching period.

In addition to [67]-[98] in modelling and analysis techniques for switching converters, the most effort of modelling switching converters has been drawn to small-signal modelling techniques [99]-[105], [131]-[135]. For instance, Verghese et al. derived the SSA based small-signal model that and compared to the experiment data samples to obtain a relationship between the dynamics of perturbations and various operating conditions near the steady-state operating point [76]. This "small-signal sampled-data model" significantly improved the SSA methods by adding the sampling effect and small perturbations to the steady-state condition, which was observed from the experiment data, due to switching transients. It enabled to predict the boundary of stability using pole-zero analysis. However, this method is too complicated in obtaining a simple periodic solution [106], which makes it difficult to analyse a general behaviour of converters.

iii. harmonic state space (HSS)

Harmonic state space (HSS) modelling of power converters had been developed [68]-[71] based on the harmonic domain (HD) modelling [75]. A general theory of the HD is to represent the coupling effects between different harmonic frequencies in the steady-state. The HSS extends the HD models in the sense that HD models are strictly limited to describe harmonics in the steady-state, whereas the HSS captures the evolution of harmonics from perturbed systems. The HSS modelling in a linear time-invariant (LTI) approach allows the traditional control methods [107]-[109] to be used. Hwang et al. [71] showed that the HSS is capable of evaluating the coupling of harmonics during transient events in an experimental setup. Based on this HSS modelling, a linear control method [75] has been developed.

iv. large signal model of switching converter

Voltage source converter (VSC) of the grid-side is presented. The basic VSC is given in [77]. It is modified to a voltage source inverter (VSI) with negative current flowing from PMSG to the grid for the WT application shown in Figure 2.2. In addition, PWM modulation and control methods are not included in this report.

For an ideally balanced voltage source and impedance, $v_a + v_b + v_c = 0$. In this example, only the fundamental frequency components of the VSI voltages are considered. There are eight possible switching combinations of S_1, S_2 and S_3, as shown in Table 2.1.

From Table 2.1, the line-to-line voltages can be expressed:

$$v_{ca}(t) = -v_{ab}(t) - v_{bc}(t) \tag{2.2}$$

Similarly, the line-to-line voltages can be expressed in terms of switching position and DC voltage:

$$v_{ab} = (S_1 - S_2) \cdot v_{dc} \tag{2.3}$$

$$v_{bc} = (S_2 - S_3) \cdot v_{dc} \tag{2.4}$$

$$v_{ca} = (S_3 - S_1) \cdot v_{dc} \tag{2.5}$$

Defining:

$$S_x = S_1 - S_2 \tag{2.6}$$

$$S_y = S_2 - S_3 \tag{2.7}$$

$$S_z = S_3 - S_1 \tag{2.8}$$

Equations (2.3) to (2.5) become:

$$v_{ab} = S_x \cdot v_{dc}(t), \quad S_x \in \{-1, 0, 1\} \tag{2.9}$$

$$v_{bc} = S_y \cdot v_{dc}(t), \quad S_y \in \{-1, 0, 1\} \tag{2.10}$$

$$v_{ca} = S_z \cdot v_{dc}(t), \quad S_z \in \{-1, 0, 1\} \tag{2.11}$$

The current dynamics can be written in the differential equation form:

$$L_f \frac{di_{abc}}{dt} + R_f \cdot i_{abc} = v_{sabc} - v_{abc} \tag{2.12}$$

The equation of the power between the AC and DC sides is defined:

$$P_{grid} + P_f = v_{dc} \cdot i_{dc} \tag{2.13}$$

where P_{grid} is the power into the grid and P_f is the power loss from the RL filter. The DC current, i_{dc} is expressed:

$$i_{dc} = \frac{v_{dc}}{R_{dc}} + C_{dc} \frac{dv_{dc}}{dt} \tag{2.14}$$

VSI capacitor resistance, R_{dc}, and switching losses are lumped into R_{dc} [78]. By substituting Equation (1.13) into Equation (1.12), the DC voltage dynamics can be written:

$$P_{grid} + P_f = v_{dc} \cdot \left(\frac{v_{dc}}{R_{dc}} + C_{dc} \frac{dv_{dc}}{dt}\right) \tag{2.15}$$

$$\frac{dv_{dc}}{dt} = \frac{P_{grid} + P_f}{C_{dc} v_{dc}} - \frac{v_{dc}}{C_{dc} R_{dc}} \tag{2.16}$$

where:

$$P_{grid} = v_a \cdot i_a + v_b \cdot i_b + v_c \cdot i_c \tag{2.17}$$

$$P_f = R_f \left[{i_a}^2 + {i_b}^2 + {i_c}^2\right] + L_f \left[i_a \frac{di_a}{dt} + i_b \frac{di_b}{dt} + i_c \frac{di_c}{dt}\right] \tag{2.18}$$

The current is expressed:

$$i_{dc} = S_1 \cdot i_a + S_2 \cdot i_b + S_3 \cdot i_c \tag{2.19}$$

Noting the sum of currents must be zero, the combination of all switching positions must be described with two switches. From Table 2.1, when both S_x and S_y are equal to 1 and -1, all combinations of switching position excluding zero DC voltage at $\{S_1, S_2, S_3\} = \{0,0,0\}$ and $\{1,1,1\}$ results in Equations (2.8) and (2.11) being eliminated. However, Equation (2.19) also needs to be reduced since the S_z term is eliminated. Problematically, S_x is expressed in terms of S_1 and S_2, and S_y is expressed in terms of S_2 and S_3. This issue results in three unknown parameters, S_1, S_2 and S_3, and two equations. Thus, a new term $S_{\hat{x}}$ is introduced by combining S_x and S_y as $S_{\hat{x}} = S_x + S_y$. From this variable change, a new set of switching functions are defined:

$$S_{\hat{x}} = S_1 - S_3 \tag{2.20}$$

$$S_y = S_2 - S_3 \tag{2.21}$$

Substituting Equation (2.20) into Equation (2.21) gives:

$$i_{dc}(t) = i_a(S_{\hat{x}}) + i_b(S_y) \tag{2.22}$$

The synchronous rotating reference frame transformation [110], which is known as Park's transformation [79], is used to express the system equations in a *dq0*-frame. The assumption behind the rotating reference frame transformation is the *d*-coordinate coincides with the rotor flux vector of rotating systems. Therefore, the quadrature component of flux, as well as its derivative, is cancelled.

This approach is beneficial for vector-oriented control since it allows the control of only one flux component, which is the *d*-axis component instead of both the *d*- and *q*-axis components. The *dq0*-transformation conversion can be found in [80], and the resulting transformation of Equations (2.12) and (2.16) can be expressed in terms of switching functions from Equations (2.20) and (2.21) as:

$$\frac{di_d}{dt} = -\frac{R_f \cdot i_d}{L_f} + \omega i_q + \frac{v_d - v_{sd}}{L_f} \tag{2.23}$$

$$\frac{di_q}{dt} = -\frac{R_f \cdot i_q}{L_f} - \omega i_d + \frac{v_q - v_{sq}}{L_f} \tag{2.24}$$

$$\frac{di_0}{dt} = -\frac{R_f \cdot i_0}{L_f} + \frac{v_0 - v_{s0}}{L_f} \tag{2.25}$$

$$\frac{dv_{dc}}{dt} = \frac{1}{C_{dc}}\begin{bmatrix} S_{\hat{x}} & S_y \end{bmatrix}\begin{bmatrix} i_d \\ i_q \end{bmatrix} - \frac{v_{dc}}{C_{dc}R_{dc}} + \frac{i_f}{C_{dc}} \tag{2.26}$$

where i_f is the current from the power loss on the RL filter, which is expressed:

$$p_f = \frac{3}{2}\cdot R_f\left(i_d^2 + i_q^2 + 2\cdot i_0^2\right) + \frac{3}{2}\cdot L_f\left(i_d\frac{di_d}{dt} + i_q\frac{di_q}{dt} + 2\cdot i_0\frac{di_0}{dt}\right) \tag{2.27}$$

Equations (1.20)-(1.23) can be written in the form of Equation (1.1), $\dot{x}_i = f_i(x,u,t)$ yielding:

$$\dot{x}_i = \{f_1, f_2, \dots f_i\}, \quad i = 1,2,3,\dots,n \tag{2.28}$$

$$\dot{x}_1 = \frac{dv_{dc}}{dt} = \frac{1}{C_{dc}}\begin{bmatrix} S_{\hat{x}} & S_y \end{bmatrix}\begin{bmatrix} i_d \\ i_q \end{bmatrix} - \frac{v_{dc}}{C_{dc}R_{dc}} + \frac{i_f}{C_{dc}} \tag{2.29}$$

$$\dot{x}_2 = \frac{di_d}{dt} = -\frac{R_f\cdot i_d}{L_f} + \omega i_q + \frac{v_d - v_{sd}}{L_f} \tag{2.30}$$

$$\dot{x}_3 = \frac{di_q}{dt} = -\frac{R_f\cdot i_q}{L_f} - \omega i_d + \frac{v_q - v_{sq}}{L_f} \tag{2.31}$$

$$\dot{x}_4 = \frac{di_0}{dt} = -\frac{R_f\cdot i_0}{L_f} + \frac{v_0 - v_{s0}}{L_f} \tag{2.32}$$

where $x = \{v_{dc}, i_d, i_q, i_0\}$, $u = \{i_f, v_{sd}, v_{sq}, v_{s0}\}$, and v_{sd}, v_{sq} and v_{s0} are *d*-, *q*- and *zero*-axis components of the AC source voltage, and v_d, v_q and v_0 are the VSI terminal voltages.

These differential equations describe a converter circuit based on the switching function. These sets of differential equations can be expressed in terms of the nonlinear state space shown in Equation (2.28), or the linear state space forms, where both are shown in Table 2.2.

Further descriptions and mathematical derivations of LTP theory can be found in [81], and its application on a grid converter model can be found in [75], [82].

2.3 Controls Used in Wind Farm

Some of the available control methods used in wind farms are discussed in this section.

2.3.1 Control of permanent magnet synchronous generator

The most common control method used in direct-drive permanent synchronous generator (PMSG) system is sensorless control [111]. Different sensorless control methods [111]-[116] have been developed to detect the accurate rotor angle without the position sensor. Among

these sensorless control methods, there are a few methods for low-speed PMSG [83], [84]. Typically, either field-oriented control (FOC) or direct torque control (DTC) in which both are defined in [117], is used to control the PMSG. Implementing these conventional control algorithms requires the information of the rotor position and angular speed is needed.

Instantaneous rotor position and angular speed data can be obtained from an encoder installed on the drivetrain. However, according to Ribrant et al., speed sensors increase the hardware complexity [85]. In addition, the sensor mounted on the rotor has to withstand the constant mechanical vibration of the rotor shaft during operation. This vibration reduces the reliability of the sensor in measuring accurate positions, and it often fails to measure. Statistically speaking, the average failure of the sensor, control and electrical systems including converters are 14.1, 12.9 and 17.5 per cent, respectively, for all Swedish wind turbine failures which occurred between the years 2000 and 2004. The PMSG model in the Appendix I is based on [86], [87], and the control algorithm is based on [88].

2.3.2 Control of converter

The main component of power electronics is the power converter for AC to DC conversion and the inverter for DC to AC conversion, which produces a desired electric power (or energy) conversion by controlling the system variables, such as voltages and currents. These converters rely on their control systems to switch devices ON and OFF. Therefore, applying the appropriate control method is essential to the converter system to obtain the desired overall performance.

Often control methods for power electronics are developed solely based on individual power electronic circuits, such as a converter circuit, but not as a complete system. It led researchers to make heavy assumptions in their component modelling. Either input or output is assumed to be constant values, or both of them are assumed constant to characterise the input-to-output relationship. Usually, these constant values refer to a steady-state operating point or a desirable fixed set point.

However, real physical systems do not always operate at a fixed set point. The operating point can vary due to the full operating range. Notwithstanding this observation, conventional linear control methods have been hugely successful in most real system applications. Hence, it must be true many systems can be well approximated by linear models.

Thus, considering nonlinear and linear controls:

- Linear control applies to systems which can be described by linear differential equations. When system parameters do not change with time, it is called a linear time-invariant (LTI) system. In general, the time-domain system response is transferred to another domain using mathematical methods, such as the popular Laplace and Fourier transforms [118]. The mathematical description of the system leads to solutions of the system response, such as frequency response, gain, resonant frequencies, poles, zeros and more. Linear control uses these solutions of the system response to control the system output.
- Nonlinear control applies to systems which can be described by nonlinear differential equations, such as those shown in Section 1.3.2. System parameters may vary (time-variant) or may not vary (time-invariant) with time, as shown in Table 2, and have nonlinear characteristics which may or may not have any solution or have multiple solutions. There are some modelling methods, such as the LTP modelling technique [81], to analyse such a system. Generally, these nonlinear methods are more complicated and less popular. Often the application of a nonlinear method only applies to specific systems, such as communications and signal processing.

  In power system transient stability, theories have been developed using nonlinear system analysis, such as the Lyapunov theory [119]. In general, nonlinear systems are analysed using numerical computations on computer simulations. Nonlinear methods can be applied to input-constrained linear systems [89]-[91] in exceptional cases if the solution at the steady-state operating condition is the point of interest.

In power electronics and power systems, two typical analysis domains are used: time and frequency (or a hybrid of both). When a nonlinear system in the time-domain is linearised around a periodic state in the frequency domain, it is referred to as an LTP system modelling [81]. Once the system is linearised, the system model can be converted back to the time-domain again.

As an example, harmonic state space (HSS) modelling of power converter systems in [68]-[71], [82] use a linear system analysis of harmonic coupling effects. HSS shows the characteristic harmonics, and their coupling, in the power converter system can be directly captured. Thus, linear control methods have been developed as in [69] based on this HSS modelling. The linear control method based on the linear converter model is quite effective and efficient for many real-world systems [120]-[122].

However, if the linear system with a linear controller (or multiple linear controllers) behaves as a nonlinear system, the controllability of the system by the controller becomes questionable. In particular, the linear controller is not designed to handle nonlinear characteristics of the system. In addition, the underlying causes of any nonlinear behaviour of the system are not identifiable from these linear systems and controls [123].

Despite all the effort of developing small-signal modelling [124] and linear system analysis [125] of switching converters, they require a significant simplification of the actual system to reduce the amount of mathematical complexity, which makes it difficult to derive all the properties of the system components with satisfactory accuracy. Indeed, linear system analysis, including piece-wise linear system analysis in a small operating window, in time or frequency domain also describes nonlinear characteristics, such as limit cycles and multiple equilibria of second- or higher-order systems in many cases [126].

The point is there is a need for precise theoretical work occupies the transitional ground in generality and applicability between linear and nonlinear system modelling and controls is needed. Such a theory would serve as a starting point for more mathematical studies and the development of applications in large scale systems such as wind farms.

2.4 Summary

In this section, linear and nonlinear system analysis, modelling and control are explored. Linear system modelling and analysis provide efficient evaluations of general system behaviours around the steady-state operating point, whereas nonlinear system modelling and analysis provide entire system behaviours.

In this thesis, both linear and nonlinear system modelling is used for WT system modelling depending on the assumptions made to a specific component. For controller, linear control strategy is used with newly developed control inputs. However, the synthesis of the control input generation is a nonlinear signal basis.

3
SYSTEM MODELLING

This chapter presents the fundamental system modelling used in this thesis. Each system component primarily consists of a two-port structure. Small-signal assumptions, such as a constant DC-link voltage, are not made. The pitch control of the blade of the WT is obtained from the average model [136]-[138].

3.1 Interface of Grid Connection

The basis of interconnecting the WT to the grid is a two-port system, as shown in Figure 3.1. It comprises seven main elements. Due to the inheritance of the transient behaviour in Port D and E, these two ports are modelled as a transient vector. The input is the wind velocity, and the output is the interaction with the grid in Port G.

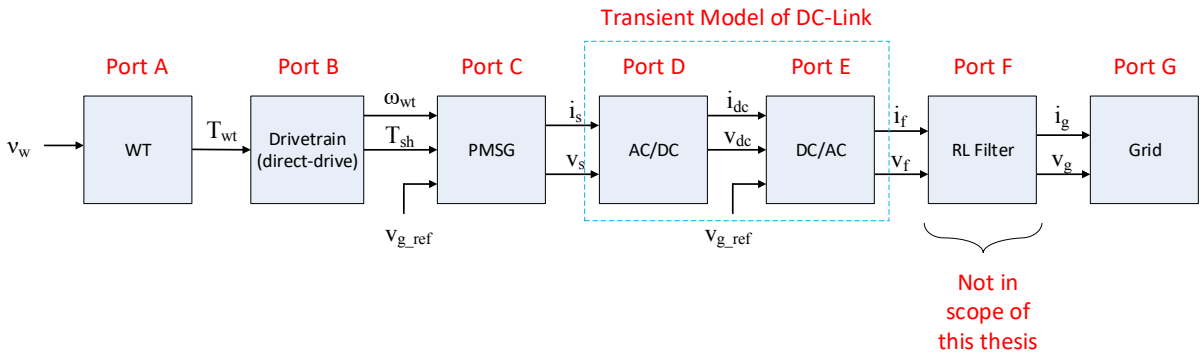

Figure 3.1: Two-port system model - cascaded WT system components.

The system models from Port A to Port C used in this thesis is the same model used in [20].

3.2 Wind Turbine

The variable speed wind turbine (WT) model shown Figure 3.2 from Port A is obtained from the average model [136]-[138] in this thesis, since it is available. Various manufacturers have different values of T_{wt}, which are not feasible to obtain due to confidentiality.

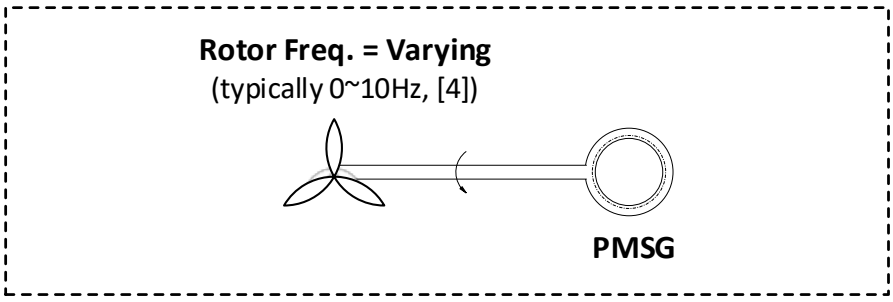

Figure 3.2: Frequency of WT.

The average model of the maximum available power and torque of the wind turbine are defined [136]:

$$P_{wt} = \frac{1}{2}\rho v_w^3 \pi R^2 C_p \tag{3.1}$$

$$T_{wt} = \frac{P_{wt}}{\omega_{wt}} \tag{3.2}$$

$$= \frac{1}{2}\rho v_w^2 \pi R^3 C_t \tag{3.3}$$

where: P_{wt} is the extractable wind power [Watt] from wind turbine,

ρ is the air density [kg/m^3],

v_w is the wind speed [m/s],

R is the radius of the rotor in [m],

C_p is the power coefficient,

C_t is the torque coefficient.

C_p is a statistical measure of wind turbine output-to-input power ratio. The input is the convertible wind power flowing into the wind turbine blades at continuously changing wind speed, and the output is the total electrical power produced by the wind turbine system. It is also referred to the overall efficiency of the complete system, which consists of the turbine blades, the shaft, gearbox, the generator, and other power electronic components used by the wind power industry in these systems.

The coefficient, C_p, must be provided by the WT manufacturer because the C_p value of a particular wind turbine is system-specific, and varies with operating conditions, such as wind speed, pitch angle, turbine speed, and other system parameters. Thus, it is usually given at various wind speeds in the system specification. The C_p value is governed by the Betz's limit [137] around 0.593, and the value of C_t is defined as a function of C_p:

$$C_t = \frac{C_p}{\lambda} \tag{3.4}$$

$$\lambda = \frac{\omega_{wt} \cdot R}{v_w} \tag{3.5}$$

where λ is the tip speed ratio, ω_{wt} is the angular velocity of the turbine rotor and v_w is the wind speed.

The tip speed ratio is the ratio of the circumferential velocity of the rotor at the blade tip and the wind velocity v_w in front of the rotor blade [137]. Substituting Equations (3.4) and (3.5) into Equation (3.3), the torque equation becomes:

$$T_{wt} = \frac{1}{2\omega_{wt}} \rho v_w^3 \pi R^2 C_p \tag{3.6}$$

where ω_{wt} is the wind turbine rotor speed [rad/s].

3.3 Drivetrain

Typically, the optimal performance of the overall system is delivered by using closed-loop feedback controllers. These controllers receive the position data of the rotor from the encoder to control and actuate the pitch angle of the blades. To understand the dynamics of the drivetrain, and how the stiffness of the shaft causes mechanical oscillations in the drivetrain, the following 2-DOF model shown in Figure 3.3 is considered.

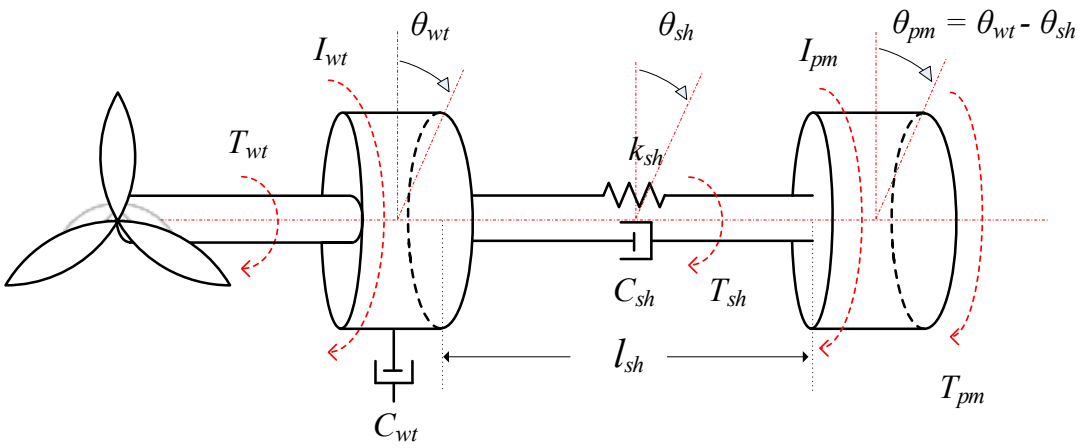

Figure 3.3: 2-DOF model of direct-drive drivetrain system.

For this 2-DOF system, a dynamic equation of motion can be expressed in a second-order differential equation. It is derived from the torque equation:

$$T = I \cdot \alpha \tag{3.7}$$

where T is the torque applied to the drivetrain, I is the rotational moment of inertia, and α is the angular acceleration.

The angular acceleration of the drivetrain is a second-order derivative of the angle/position obtained from the encoder. All torque values are calculated on one side of each mass, and thus the angular acceleration is defined:

$$\alpha = \frac{d^2\theta_{wt}}{dt^2} \tag{3.8}$$

The torque equations for the WT and PMSG become:

$$I_{wt} \cdot \frac{d^2\theta_{wt}}{dt^2} = T_{wt} - T_{sh} - T_{wt,fr} \tag{3.9}$$

$$I_{pm} \cdot \frac{d^2\theta_{pm}}{dt^2} = T_{sh} - T_{pm} - T_{pm,fr} \tag{3.10}$$

The equation for the instantaneous torque of WT is given in [138]. The equation of angular acceleration for the PMSG is similar to Equation (3.9). However, the torque applied to the PMSG is directly transferred from the shaft and counter electromagnetic (EM) torque. Therefore, there is no external torque applied on PMSG, T_{pm}, other than inherited from the shaft, T_{pm} is 0. Thus, Equation (3.10) becomes:

$$I_{pm} \cdot \frac{d^2\theta_{pm}}{dt^2} = T_{sh} - T_{pm,fr} \tag{3.11}$$

The equations for the shaft torque and the frictional torque are thus defined:

$$T_{sh} = k_{sh}(\theta_{wt} - \theta_{pm}) + C_{sh}\left(\frac{d\theta_{wt}}{dt} - \frac{d\theta_{pm}}{dt}\right) \tag{3.12}$$

$$T_{wt,fr} = C_{wt}\left(\frac{d\theta_{wt}}{dt}\right) \tag{3.13}$$

$$T_{pm,fr} = 0, \quad \text{since there is no spring on the PMSG rotor.}$$

where: I_{wt} = wind turbine rotor inertia [kg·m^2],

I_{pm} = generator inertia [kg·m^2],

T_{wt} = wind turbine torque [N·m],

$T_{wt,fr}$ = force of friction of wind turbine rotor [N·m],

T_{sh} = shaft torque [N·m],

T_{pm} = electromagnetic torque of PMSG [N·m],

$T_{pm,fr}$ = force of friction of PMSG [N·m],

k_{sh} = coefficient of shaft stiffness [N/m],

C_{wt} = coefficient of wind turbine damping [N·s/m],

C_{sh} = coefficient of shaft damping [N·s/m],

θ_{wt} = position (angle) of wind turbine rotor [rad], and

θ_{pm} = position (angle) of PMSG rotor [rad].

By substituting Equations (3.12) - (3.13) into Equations (3.10) and (3.11), the dynamic torque equations are obtained, yielding:

$$I_{wt} \cdot \left(\frac{d^2\theta_{wt}}{dt^2}\right) = T_{wt} - \left[k_{sh}(\theta_{wt} - \theta_{pm}) + C_{sh}\left(\frac{d\theta_{wt}}{dt} - \frac{d\theta_{pm}}{dt}\right)\right] - C_{wt}\left(\frac{d\theta_{wt}}{dt}\right) \quad (3.14)$$

$$I_{pm} \cdot \left(\frac{d^2\theta_{pm}}{dt^2}\right) = k_{sh}(\theta_{wt} - \theta_{pm}) + C_{sh}\left(\frac{d\theta_{wt}}{dt} - \frac{d\theta_{pm}}{dt}\right) \quad (3.15)$$

where $\theta = \theta_{wt} - \theta_{pm}$, which is the angular displacement between the WT rotor and PMSG rotor. Therefore $\dot{\theta} = \dot{\theta}_{wt} - \dot{\theta}_{pm}$ and $\ddot{\theta} = \ddot{\theta}_{wt} - \ddot{\theta}_{pm}$.

The equations are expressed as differential equations in terms of WT rotor position angle where the input torque is applied. The idea behind the equation is that this particular wind turbine is sensorless, and thus only the position of the WT and PMSG rotors is available via encoders.

As seen in Equations (3.14) and (3.15), the coefficient of shaft stiffness is coupled with the angular displacement. Thus, larger stiffness of the shaft increases the force applied in the drivetrain. For a flexible shaft, with a lower stiffness, the shaft twists. As a result, one end of the shaft rotates relative to the other, end inducing shear stress in the shaft.

Rearranging Equations (3.14) and (3.15), the drivetrain system equations of motion are derived:

$$T_{wt} = I_{wt}\ddot{\theta}_{wt} + (C_{wt} + C_{sh}) \cdot \dot{\theta}_{wt} - C_{sh}\dot{\theta}_{pm} + k_{sh}\theta_{wt} - k_{sh}\theta_{pm} \quad (3.16)$$

$$0 = I_{pm}\ddot{\theta}_{pm} + C_{sh} \cdot \dot{\theta}_{pm} - C_{sh}\dot{\theta}_{wt} + k_{sh}\theta_{pm} - k_{sh}\theta_{wt} \quad (3.17)$$

Equations (3.16) and (3.17) are a two degree of freedom system containing a fourth-order characteristic equation, which gives a second-order polynomial. This polynomial has complex solutions due to the relatively low damping due to shaft flexure.

By taking the Laplace transform of Equations (3.16) and (3.17), the equations of motions are expressed in terms of frequency:

$$\begin{bmatrix} T_{wt}(s) \\ 0 \end{bmatrix}$$

$$= \begin{bmatrix} I_{wt}s^2 + (C_{wt} + C_{sh})s + C_{sh} & -C_{sh}s - k_{sh} \\ -C_{sh}s - k_{sh} & I_{pm}s^2 + C_{sh}s + k_{sh} \end{bmatrix} \begin{bmatrix} \theta_{wt}(s) \\ \theta_{pm}(s) \end{bmatrix} \quad (3.18)$$

The damping coefficient term D_{wt} is coupled with D_{sh} contributing the damping oscillation in the drivetrain system. These damping coefficient terms are called cross-coupled damping [145]. When there is positive cross-coupled damping, a deflection causes a reaction force, displacing the shaft horizontally as if applying a vertical force. If the damping coefficients are significantly large enough to make the mechanical system unstable, WT operation needs to be shut down immediately before any severe damage occurs [143].

The damping of WT and PMSG with low-frequencies refers the torsional vibration exerted on the structure, which is critically damped and does not impact the natural frequency in this case. If the damping of WT and PMSG is significant, it may lead to the failure of the WT structure [144]. Therefore, the effect of damping of the WT and PMSG on the resonant frequencies can be negligible [139], and the angular frequencies are defined:

$$\omega_{ar} = \sqrt{\frac{k_{sh}}{I_{pm}}} \quad (3.19)$$

$$\omega_r = \sqrt{k_{sh}\left(\frac{I_{wt} + I_{pm}}{I_{wt}I_{pm}}\right)} \quad (3.20)$$

The, the equation of motion in Equation (3.18) then becomes:

$$\frac{\theta_{wt}}{T_{wt}}(s) = \frac{1}{(I_{wt} + I_{wt})s^2}\left(\frac{I_{wt}s^2 + C_{sh}s + k_{sh}}{\frac{I_{wt}I_{pm}}{I_{wt} + I_{pm}}s^2 + C_{sh}s + k_{sh}}\right)$$

$$= \frac{A\left(\frac{s^2}{\omega_{ar}^2} + \frac{2\gamma_{ar}s}{\omega_{ar}} + 1\right)}{s^2\left(\frac{s^2}{\omega_{ar}^2} + + \frac{2\gamma_{ar}s}{\omega_{ar}} + 1\right)} \quad (3.21)$$

$$\frac{\theta_{pm}}{T_{wt}}(s) = \frac{1}{(I_{wt}+I_{wt})s^2}\left(\frac{C_{sh}s + k_{sh}}{\frac{I_{wt}I_{pm}}{I_{wt}+I_{pm}}s^2 + C_{sh}s + k_{sh}}\right)$$

$$= \frac{A\left(\frac{C_{sh}}{k_{sh}}s + 1\right)}{s^2\left(\frac{s^2}{\omega_r^2} + + \frac{2\gamma_r s}{\omega_r} + 1\right)}$$

$$= \frac{A(\tau s + 1)}{s^2\left(\frac{s^2}{\omega_r^2} + + \frac{2\gamma_r s}{\omega_r} + 1\right)} \tag{3.22}$$

where [145]:

$$A = \frac{1}{I_{wt}+I_{pm}}$$

$$\tau = \frac{C_{sh}}{k_{sh}}$$

$$\gamma_{ar} = \frac{C_{sh}}{2\sqrt{k_{sh}I_{pm}}}$$

$$\gamma_r = \frac{C_{sh}}{2\sqrt{k_{sh}\left(\frac{I_{wt}I_{pm}}{I_{wt}+I_{pm}}\right)}}$$

The angular frequencies, ω_{ar} and ω_r represent the oscillation modes, where the interaction between WT and PMSG occur. The resonant frequencies, ω_{ar} and ω_r are the anti-resonant and the resonant frequencies, respectively.

The peaks of ω_{ar} and ω_r of the system are the anti-resonant and resonant frequencies when the WT system exhibits resonant behaviours. At ω_{ar}, the PMSG rotor rotates with an equal and opposite torque from the WT rotor resulting in the oscillation of PMSG. It implies that the exciting force of the oscillation from the WT is "absorbed" [140] by physically coupled mechanical components, such as a shaft between the PMSG and WT rotors. The vibration of the WT is absorbed through the valley in the frequency response. The rotational inertia from the PMSG behaves as a vibration absorber, which absorbs the oscillations from the WT. Thus,

the coupled components act as an additional restraint to the system at the anti-resonant frequency.

At ω_r, the WT and PMSG rotors are at the peak of the resonant frequency. Thus, the force from the WT and PMSG become amplified in the drivetrain system, and both the WT and PMSG rotors oscillate together. It translates into structural vibrations in the WT nacelle.

3.4 Permanent Magnet Synchronous Generator

The equivalent circuit of the permanent magnet synchronous generator (PMSG), is shown in Figure 3.4. It is based on the transient model of permanent magnet synchronous machine (PMSM) [146]. Any change in the magnetic flux of the rotor magnet would cause an induced electromotive force (EMF), which results in a circulating current in the magnet.

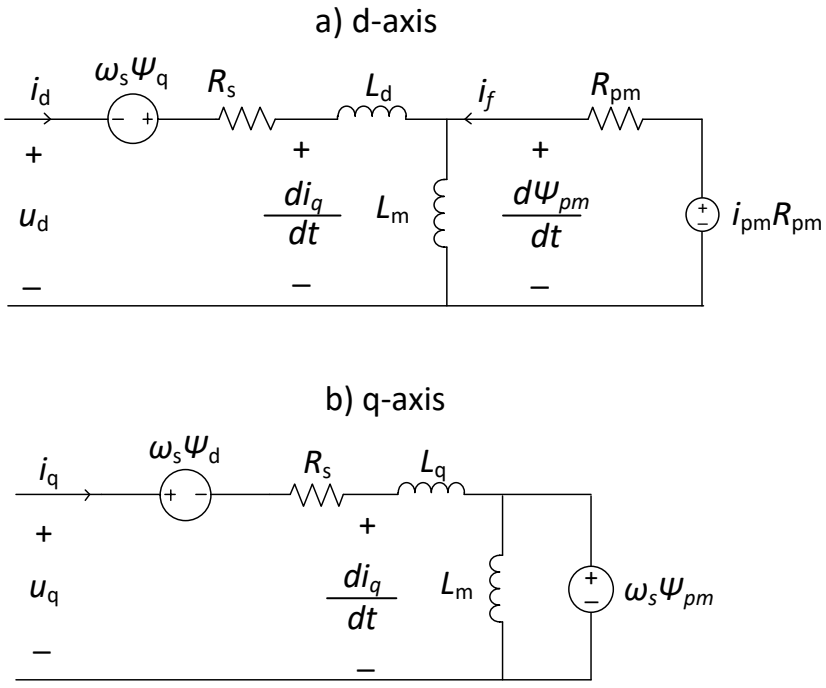

Figure 3.4: PMSG circuit representation.

Sebastian *et al.* [86] stated "… *assuming that the penetration depth δ at the maximum frequency of concern is large in comparison with the magnet's radial thickness, each magnet can be considered approximately as a conducting loop of length* l_r*, angular span 2α, having a resistance* R'_m." When transferred across the air gap to the equivalent number of direct-axis

stator turns, it represents as a mutual resistance R_m, connected across the direct-axis magnetising inductance L_m. The mutual resistance, R_m, is defined [86]:

$$R_m = \left(\frac{4N_s}{\pi \sin \alpha}\right)^2 \cdot \frac{R'_m}{n} \tag{3.23}$$

where n is the number of pole pairs and N_s is the number of turns in the stator winding.

Since the magnet-to-core interface is mainly a non-conducting adhesive, this path can be ignored [86]. Based on the circuit model without the zero-sequence component, the equation of voltage in dq-axis is expressed:

$$v_{sd} = R_s i_{sd} - \omega_s \psi_{sq} + (L_{sd}+L_{sm}) \frac{di_{sd}}{dt} \tag{3.24}$$

$$v_{sq} = R_s i_{sq} - \omega_s \psi_{sd} + \left(L_{sq}+L_{sm}\right) \frac{di_{sq}}{dt} + \omega_s \psi_{pm} \tag{3.25}$$

where: $\psi_{sd} = (L_{sd}+L_{sm}) \cdot i_{sd}$ and $\psi_{sq} = \left(L_{sq}+L_{sm}\right) \cdot i_{sq}$.

Substituting ψ_{sd} and ψ_{sq} into Equations (3.24) and (3.25), respectively, yields the current dynamics in state form:

$$\frac{di_{sd}}{dt} = \frac{v_{sd} - R_s i_{sd} + \omega_s i_{sq}\left(L_{sq}+L_{sm}\right)}{L_{sd} + L_{sm}} \tag{3.26}$$

$$\frac{di_{sq}}{dt} = \frac{v_{sq} - R_s i_{sq} + \omega_s i_{sd}(L_{sd}+L_{sm}) - \omega_s \psi_{pm}}{L_{sq} + L_{sm}} \tag{3.27}$$

Where: ω_s = the synchronous rotor speed of PMSG [rad/s],

R_s = the stator resistance [ohm],

ψ_{pm} = the flux linkage by permanent magnet [Wb],

ψ_{sd} = the flux linkage of d-axis [Wb],

ψ_{sq} = the flux linkage of q-axis [Wb],

L_{sd} = the inductance of d-axis [H],

L_{sq} = the inductance of q-axis [H],

L_{sm} = the stator mutual inductance [H], and

R_{sm} = the stator mutual resistance [H].

The electromagnetic torque, T_{pm_EM} [N·m] of the PMSG is calculated:

$$T_{pm\_EM} = 1.5n\left[\psi_{pm} i_{sq} + \left(L_{sd} - L_{sq}\right) \cdot \underbrace{i_{sd} i_{sq}}\right] \tag{3.28}$$

PMSG EM torque is the dq-axis current

Ideally, T_{pm_EM} should be equal and opposite of the mechanical T_{wt} in Equation (3.10), i.e. T_{wt} - T_{pm_EM} = 0 if the losses in the drivetrain system are negligible.

There are numerous turbines and generator torque controllers available. However, many of these controllers are proprietary and thus not publicly available. This work uses the generic WT pitch control and torque control algorithms given in [138], with resonant controller tuning techniques used in [142], which are directly implemented for the low- and variable-speed WT. The torque control of the PMSG is achieved by setting the torque:

$$T_{pm\_EM} = K\omega_s^2 \tag{3.29}$$

where the gain K is defined in [141].

Assuming v_w, ω_{wt}, and ρ are given, the equation of K becomes:

$$K = \frac{1}{2}\rho\pi R^5 \left(\frac{C_{p\_max}}{\lambda_{pm^*}^3}\right) \tag{3.30}$$

where $C_{p\_\max}$ is the maximum achievable power coefficient by the turbine, R is the radius of the rotor or the length of the blade [m], ρ is the air density [kg/m^3], and λ_{pm^*} is the tip speed ratio at $C_{p\_\max}$.

The generator control is based on the assumption the d-axis is perfectly aligned with ψ_{pm}. The q-axis current is used to control the electromagnetic (EM) torque of the PMSG. Thus, d-axis reference current i_{sd}^* is set to zero, whereas the q-axis reference current i_{sq}^* is computed:

$$i_{sq}^* = \frac{2}{3n\psi_{pm}} T_{pm}^* \tag{3.31}$$

3.5 Machine-Side Converter

The machine-side converter (MSC) used in this thesis is a three-phase full-wave rectifier, as shown in Figure 3.5. The rectifier reverses the voltage with negative polarity to the positive periodically to convert AC to DC, as shown in Figure 3.6. Thus, only the current controller for the PMSG is considered.

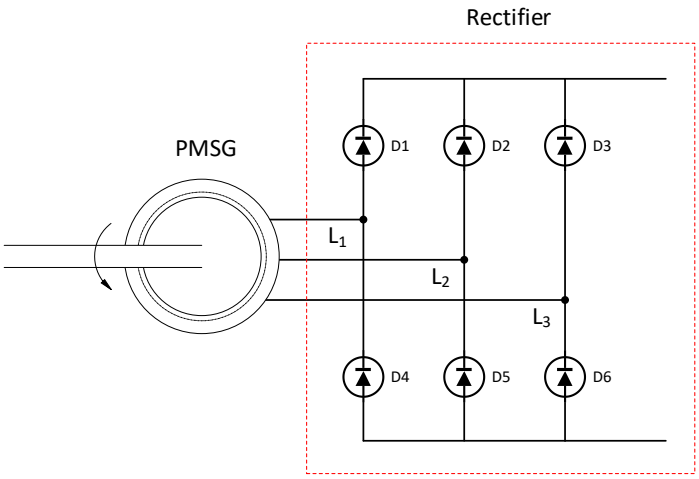

Figure 3.5: Rectifier connected to the PMSG terminal

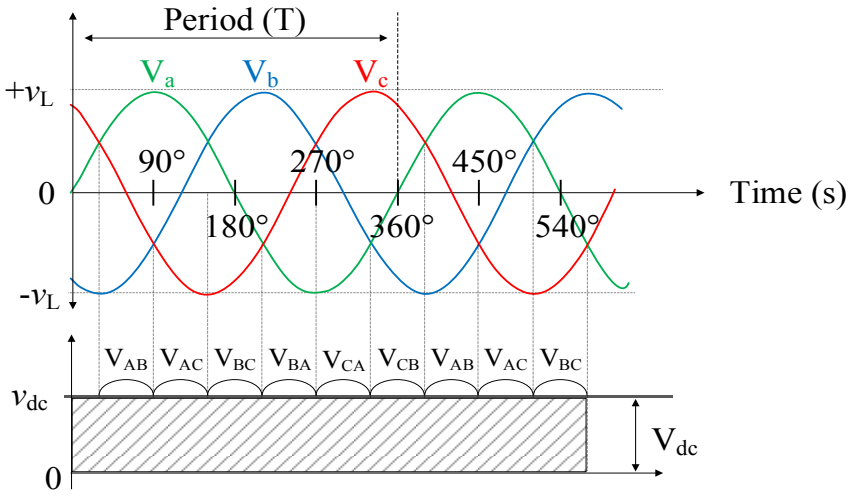

Figure 3.6: Rectifier conduction waveform

For the three-phase full-wave rectifier, the PMSG terminal voltages, V_a, V_b and V_c, with a phase shift of the 120° give:

$$V_a = V_{peak} \cdot \sin(\omega t) \tag{3.32}$$

$$V_b = V_{peak} \cdot \sin(\omega t - 120°) \tag{3.33}$$

$$V_c = V_{peak} \cdot \sin(\omega t + 120°) \tag{3.34}$$

The average DC voltage v_{dc} of the 3-phase half-wave rectifier is given [147]:

$$v_{dc} = 2 \cdot \frac{3\sqrt{2}}{\pi} \cdot v_L \tag{3.35}$$

where v_L is the root mean squared (rms) line voltage of the PMSG terminal.

3.6 Grid-Side Voltage Source Inverter

The voltage source inverter (VSI) model for the wind farm used in this thesis is based on the power balance equation (PBE): DC input = AC output. The PBE eliminates the switching function between DC and AC, which makes it easy to solve. However, the new model of the VSI does not use the grid filter parameters, R_f and L_f as the conventional PBE. It eliminates the variable i_{abc} from the grid, which cannot be used as a control input during a fault condition or islanding operation. During the fault the voltage and current from the grid are undesirable values, and they should not be used as inputs of the control. The new VSI model starts with:

$$P_{in} = P_{out} \tag{3.36}$$

where P_{in} is the DC power entered to the VSI, and P_{out} is the power measured at the RL fileter shown in Figure 3.7, respectively, defined:

$$P_{out} = v_{abc} \cdot i_{abc} \tag{3.37}$$

$$P_{in} = v_{dc} \cdot i_{dc} = v_{abc} \cdot i_{abc} \tag{3.38}$$

where P_{ac} is the active power from the PMSG terminal, and P_{dc} is the measured power at the DC-link.

The loss of DC-link circuit is represented by placing a lump resistor value R_{dc} shown in Figure 3.7. The current, i_{dc}, is defined:

$$i_{dc} = C_{dc} \frac{dv_{Cdc}}{dt} - \frac{v_{Cdc}}{R_{dc}} \tag{3.39}$$

Substituting Equation (3.39) into Equation (3.38), the following equation for the power balance equation is obtained.

$$v_{dc}\left(C_{dc}\frac{dv_{Cdc}}{dt}-\frac{v_{Cdc}}{R_{dc}}\right)=v_{abc}\cdot i_{abc} \tag{3.40}$$

Since $v_{abc}\cdot i_{abc}=v_{dc}\cdot i_{dc}$, Equation (3.40) becomes:

$$v_{dc}\left(C_{dc}\frac{dv_{Cdc}}{dt}-\frac{v_{Cdc}}{R_{dc}}\right)=v_{dc}\cdot i_{dc} \tag{3.41}$$

The DC voltage dynamics can be written:

$$\begin{aligned}\frac{dv_{Cdc}}{dt}&=\frac{v_{dc}\cdot i_{dc}}{C_{dc}\cdot v_{dc}}+\frac{v_{dc}\cdot v_{Cdc}}{C_{dc}\cdot R_{dc}\cdot v_{dc}}\\&=\frac{1}{R_{dc}\cdot C_{dc}}\cdot v_{Cdc}+\frac{1}{C_{dc}}\cdot i_{dc}\end{aligned} \tag{3.42}$$

where $R_{dc}\cdot C_{dc}$ is a time constant, τ_{dc}, to charge and discharge the DC-link capacitor, can be obtained from the capacitor manufacturer.

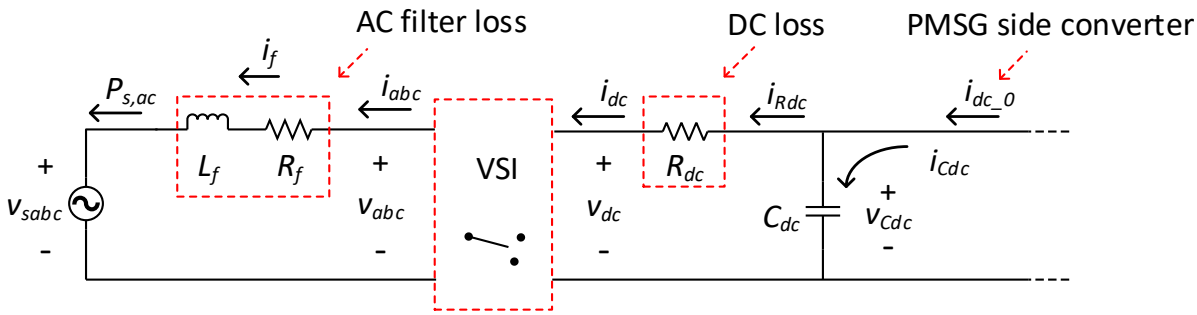

Figure 3.7: RL-filter VSI connected to the grid.

3.7 Transient DC-Link Model

The purpose of DC-link is to connect a rectifier/converter on the generator side and an inverter on the grid side. The capacitor filters our small variations of the two voltages from the converter and inverter. The DC link is simply the capacitor connection between these two converter circuits, as shown in Figure 3.8.

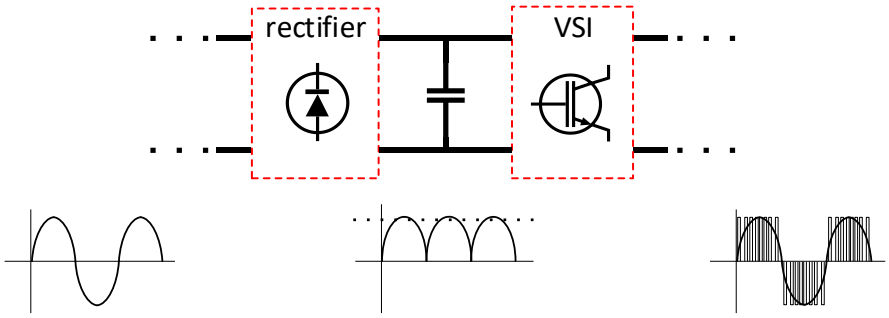

Figure 3.8: The DC-link.

The previous section describes the voltage dynamics of the DC-link. In this section, the current dynamics are described. The current is not assumed to be constant, but treated as an inherited vector from the PMSG.

3.7.1 Current dynamics of DC-link

In the previous section, the DC link voltage dynamics were described using the power balance method. However, it does not consider the inherited current from the generator via MSC during transient events when the grid is faulted. For wind turbine applications, the grid behaves as a swing source, rather than a voltage source or power supply, as shown in Figure 3.9. The swing source is a term used to represent power grid, which can behaves as a load, voltage source or both in power systems analysis software.

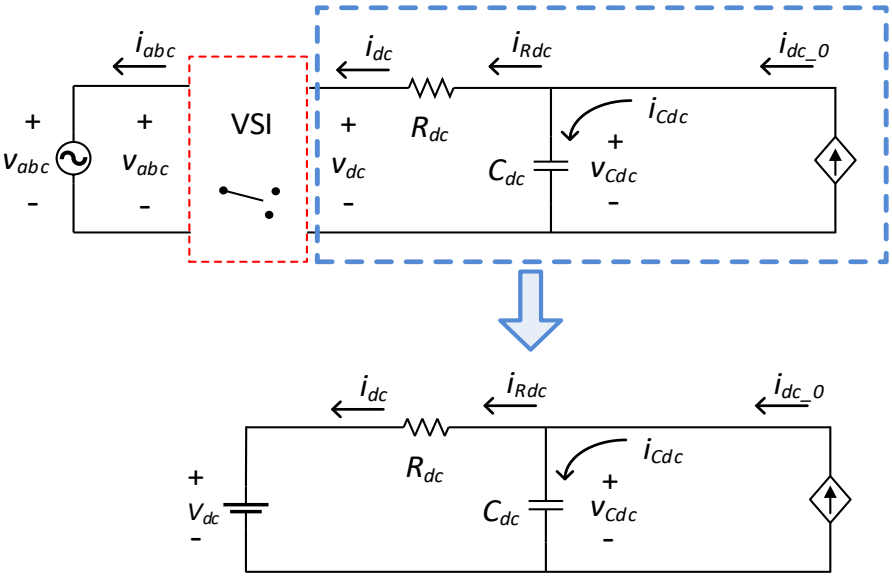

Figure 3.9: The equivalent RC circuit of DC-link in the steady-state condition.

For wind turbine applications, the voltage on the DC link capacitor is the voltage from the grid and the PMSG generator. The DC link circuit is modelled as an RC circuit with both voltage and current sources. The voltage source is from the grid, and the current source is from the generator. The DC link circuit can be derived by using the superposition method. However, during a grid fault, the grid-side of the VSI is disconnected, which makes the PBE no longer valid, as shown in Figure 3.10.

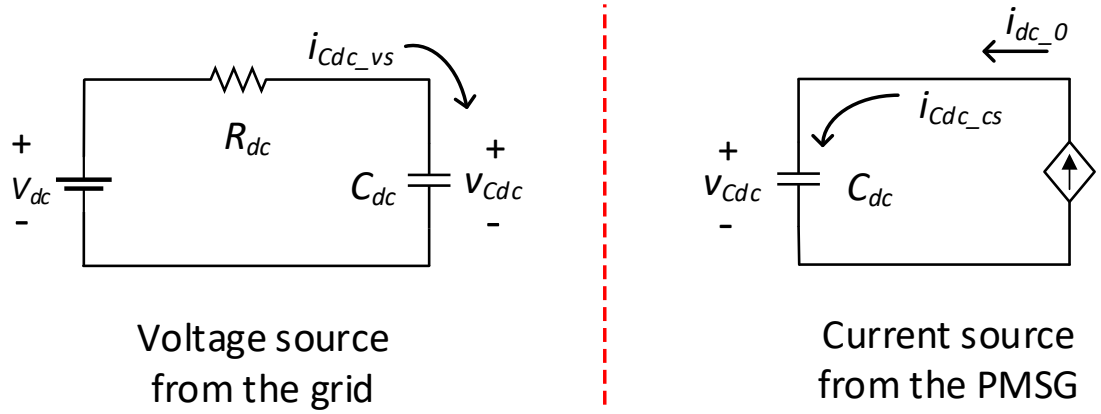

Figure 3.10: Superposition method of an RC circuit with voltage and current sources.

Figure 3.10 depicts the DC link voltage v_{cdc} depends on both the grid and generator voltages. In the majority of small-signal modelling, typically for HVDC applications, the DC link voltage is considered as a constant voltage because it stays nearly constant during the steady-state operating condition. However, for large-signal modelling, the grid voltage and the generator voltage do fluctuate significantly during large-signal disturbances.

The magnitude of voltage fluctuation depends on the location and type of faults. For instance, if the fault occurs on the grid side, the voltage on the grid side drops to the minimum fault ride-through requirement. In this case, the generation system must stay connected to transmission system under certain operational voltage levels.

The most significant problem with this steady-state based circuit model is the control of the VSI and PMSG are based-on this steady-state condition. Thus, conventional small-signal models with PBE work well only for the steady-state circuit, and possibly for very short grid faults. In additions, to obtain the solutions to the steady-state equation, the DC capacitor voltage, v_{Cdc}, is treated as a constant, rather than variable. The capacitor voltage remains nearly

unchanged during the steady-state, but it is not constant during transient events. Therefore, the transient model should only be described with DC quantities, as shown in Figure 3.11.

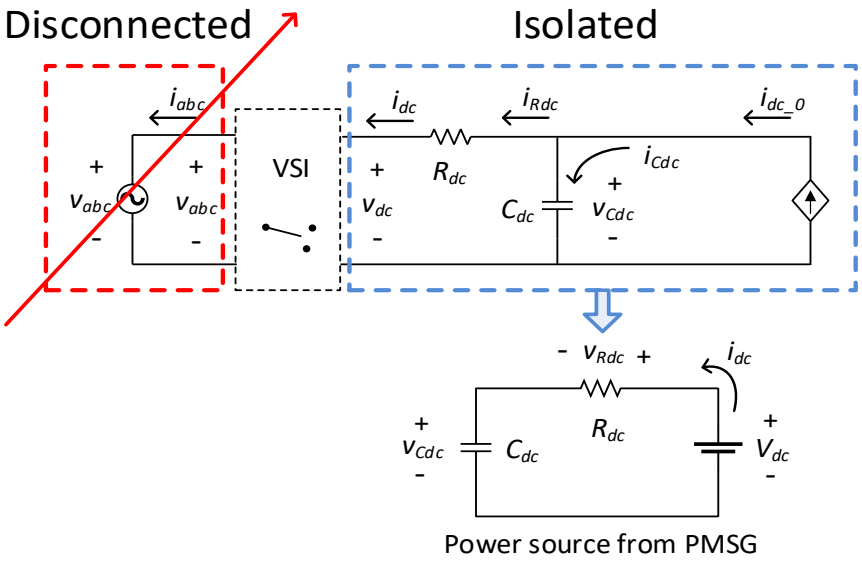

Figure 3.11: DC-link condition during the grid fault

When the WT system is in an islanding condition, PMSG becomes a power supply, in which V_{dc} and i_{dc} are inherited from the PMSG. v_{Cdc} is the voltage of the DC capacitor. The DC capacitor appears to be a short circuit between VSI and PMSG and the current inherited from the PMSG is restricted only by the resistor R_{dc}. Using Kirchhoff's voltage law (KVL), the voltage drop across the DC-link circuit is defined:

$$R_{dc}\frac{di_{dc}}{dt}+\frac{i_{dc}}{C_{dc}}=\frac{dv_{dc}}{dt}$$

$$\Rightarrow \quad \frac{di_{dc}}{dt}=-\frac{1}{C_{dc}}i_{dc}+\frac{1}{R_{dc}}\frac{dv_{dc}}{dt} \tag{3.43}$$

where: $i_{dc}=\frac{v_{dc}}{R_{dc}}e^{-t/\tau_{dc}}$.

Combining Equations (2.26), (2.27), (3.42) and (3.43), the complete state equations of the system become:

$$\dot{x}_1=\frac{di_{dc}}{dt}=-\frac{1}{C_{dc}}i_{dc}+\frac{1}{R_{dc}}\frac{dv_{dc}}{dt} \tag{3.44}$$

$$\dot{x}_2 = \frac{dv_{Cdc}}{dt} = \frac{1}{R_{dc} \cdot C_{dc}} \cdot v_{Cdc} + \frac{1}{C_{dc}} \cdot i_{dc} \tag{3.45}$$

$$\dot{x}_3 = \frac{di_d}{dt} = -\frac{R_f}{L_f} \cdot i_d + \omega i_q + \frac{v_d - v_{sd}}{L_f} \tag{3.46}$$

$$\dot{x}_4 = \frac{di_q}{dt} = -\frac{R_f}{L_f} \cdot i_q - \omega i_d + \frac{v_q - v_{sq}}{L_f} \tag{3.47}$$

Equations (3.44) and (3.45) describe the transient dynamics of back-to-back converters, and Equations (3.46) and (3.47) describe the PBE between the WT and grid when they are connected. Note that Equations (2.26) and (2.27) are obtained from the previous chapter.

3.8 Grid Model

The Technical University of Denmark (DTU) and Risø National Laboratory (RNL) released an analytical report after a 13-year survey called, "mapping of grid faults and grid codes" [12] based on grid faults and their impact on grid-connected WTs. The report identified grid-connected wind turbines are more frequently subject to grid faults. Although it does not mention specifically which wind farms experienced losses due to grid faults, various grid faults can occur anywhere in the grid. Most of these faults are associated with voltage disturbance. They are usually characterised by the magnitude of the voltage fluctuation and the time period of the fault.

Only the weak grid model is used in this thesis work because oscillation phenomena are not seen with strong grid with high short-circuit ratio (SCR). A weak grid is typically defined as having an SCR < 3, as defined in the IEEE Standard 1204-1997 [142]. Typically, it is not recommended to interconnect converters (or inverters) to a weak grid for stability concerns [148]. However, in some cases, such as large wind farms, it is unavoidable to interconnect wind farms to a weak grid in rural areas.

The weak grid model used in this thesis is based on the equivalent series impedance [21], as shown in Figure 3.12. The electrical power flows from the VSI terminal to the grid. The higher SCR means the stronger grid, which indicates the strength of the grid network.

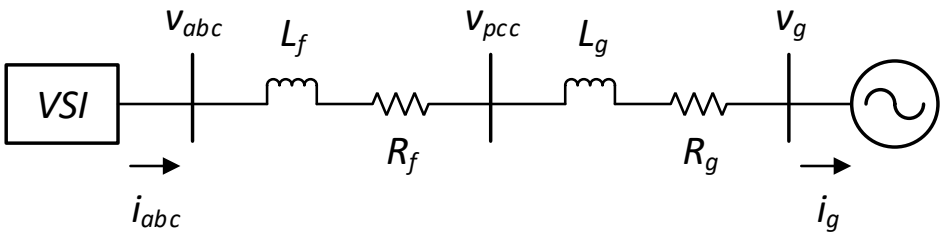

Figure 3.12: Circuit diagram of the grid model.

The total impedance of the grid network is calculated:

$$Z_f = R_f + jL_f \tag{3.48}$$

$$Z_g = R_g + jL_g \tag{3.49}$$

$$R_{total} = R_f + R_g \tag{3.50}$$

$$L_{total} = L_f + L_g \tag{3.51}$$

$$Z_{total} = \sqrt{{R_{total}}^2 + {L_{total}}^2} \tag{3.52}$$

The SCR is defined [195]:

$$SCR = \frac{v_g^2}{Z_{total} \cdot S_{nominal}}$$

where v_g is the rated grid voltage and $S_{nominal}$ is the rated power of the WTG.

3.9 Summary

This chapter defines the complete simulation model of the two-port WT system. The transient model of the back-to-back converters is described with DC quantities only. This circuit model treats the DC-link voltage and current as an inherited variables from the PMSG, rather than constant values, as seen in most small-signal models.

4
SIMULATION

This chapter introduces the oscillation problems via simulations with the system model discussed in Chapter 3. The oscillation problems can be identified as torsional oscillation (TO) or sub-synchronous control interaction (SSCI) problems, which have some similarities, but have distinct differences in the system response and disturbance characteristics. MATLAB/Simulink® is used to simulate the TO and SSCI phenomena in time domain.

4.1 Oscillation in Drivetrain

The drivetrain system is simulated to validate the mathematical model from Chapter 3. This simulation is vital to investigate any critical failure of the mechanical component where the output of the PMSG is in close proximity of the grid and impact of the DC-link on torsional oscillation (TO) is essential to the system stability because the transient interactions may cause voltage, current and frequency oscillations to appear at the PMSG terminal which is the critical component of the WT system.

The result of the o simulation has been discussed at the end of this section.

4.1.1 Drivetrain response

The system is simulated with MATLAB/Simulink® with actual data given in Appendix II. Two different cases were simulated. The first is a flexible shaft case, as shown in Figure 4.1. The second is an infinitely rigid shaft case, as shown in Figure 4.2.

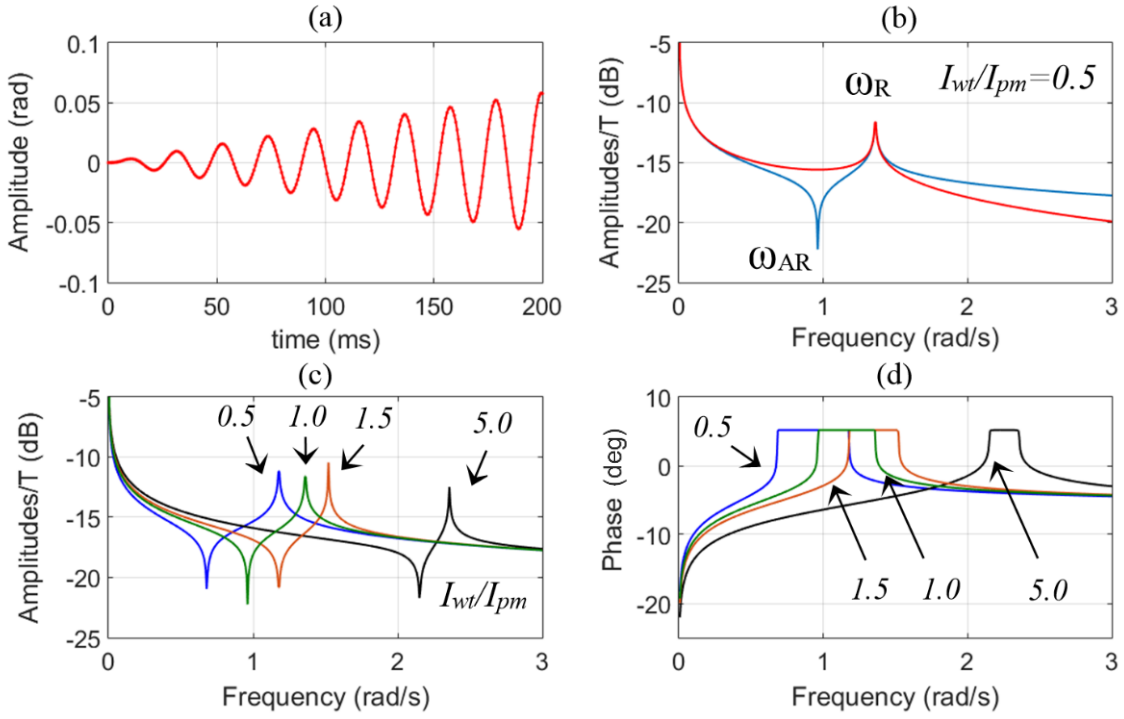

Figure 4.1: Simulation result of the flexible shaft [20]: (a) step response of shaft damping, (b) Bode plot of θ_{wt}/T_{wt} and θ_{pm}/T_{pm}, (c) Bode plot of θ_{wt}/T_{wt} with various inertia ratios and (d) phase plot of WT and PMSG with various inertia ratios.

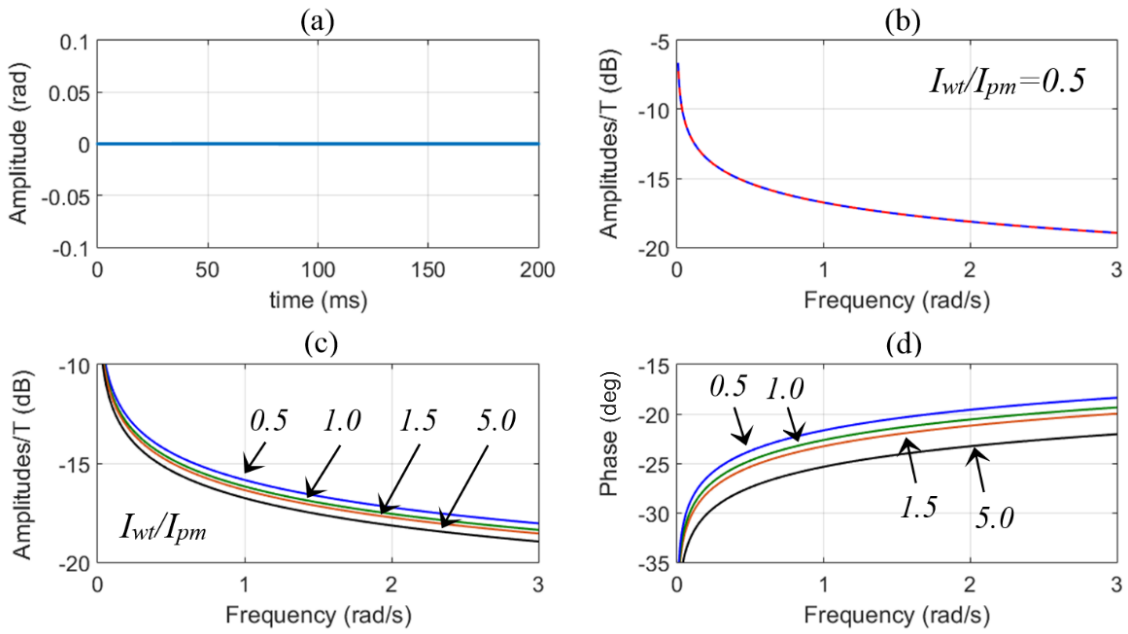

Figure 4.2: Simulation result of the rigid shaft [20]: (a) step response of shaft damping, (b) Bode plot of θ_{wt}/T_{wt} and θ_{pm}/T_{pm}, (c) Bode plot of θ_{wt}/T_{wt} with various inertia ratios and (d) phase plot of WT and PMSG with various inertia ratios.

As Figures 4.1 and 4.2 depict the simulation result of the valley at anti-resonance and resonance, they potentially interfere with the feedback control. Practically, placing a low-pass filter would remove these valleys. Adjusting the control gain parameters of the PMSG feedback controller is tuned to achieve steady-state conditions around the operating frequency. However, Figure 4.1 shows both anti-resonance and resonance occur at very low frequencies. Placing a low-pass filter (LPF) to cut-off the valleys of the anti-resonance and resonance frequencies would reduce the usable frequency bandwidth. As the inertia ratio increases, both anti-resonant and resonant valleys are significantly shifted to higher frequencies, as shown in Figure 4.1 (c). In addition, increasing the stiffness of the shaft can tie the peaks of anti-resonant and the resonant closer together (i.e. inertia ratio = 0.5 vs 5 in Figure 4.1 (c)).

Equations (3.20) and (3.21) for ω_{ar} and ω_r show the resonant frequency strongly depends on the stiffness of the shaft, and the inertia of the PMSG and WT. Figure 4.2 shows a stiffer shaft alone can significantly improve the damping response in the drivetrain system by reducing transmitted vibration. Reduction of vibration does not necessarily guarantee the overall stability of the drivetrain system, which will be discussed in Section 4.1.2. In addition, the problematic anti-resonant and resonant valleys are adequately attenuated to the desired level.

However, this simulation does not show how the drivetrain interacts with other components, such as the WT and the PMSG since the WT model is not presented in this thesis. However, it shows the oscillation problem because all shafts are flexible in reality, and there is no such shaft with infinite stiffness. The flexible shaft absorbs small torque vibrations.

4.1.2 Torsional oscillation

Case 1: flexible shaft

The drivetrain system is simulated with the flexible shaft parameters given in Appendix II to obtain the steady-state condition. The stiffness coefficient of the flexible shaft is obtained from [20]. The results of Case 1 are given in Figures 4.3 and 4.4.

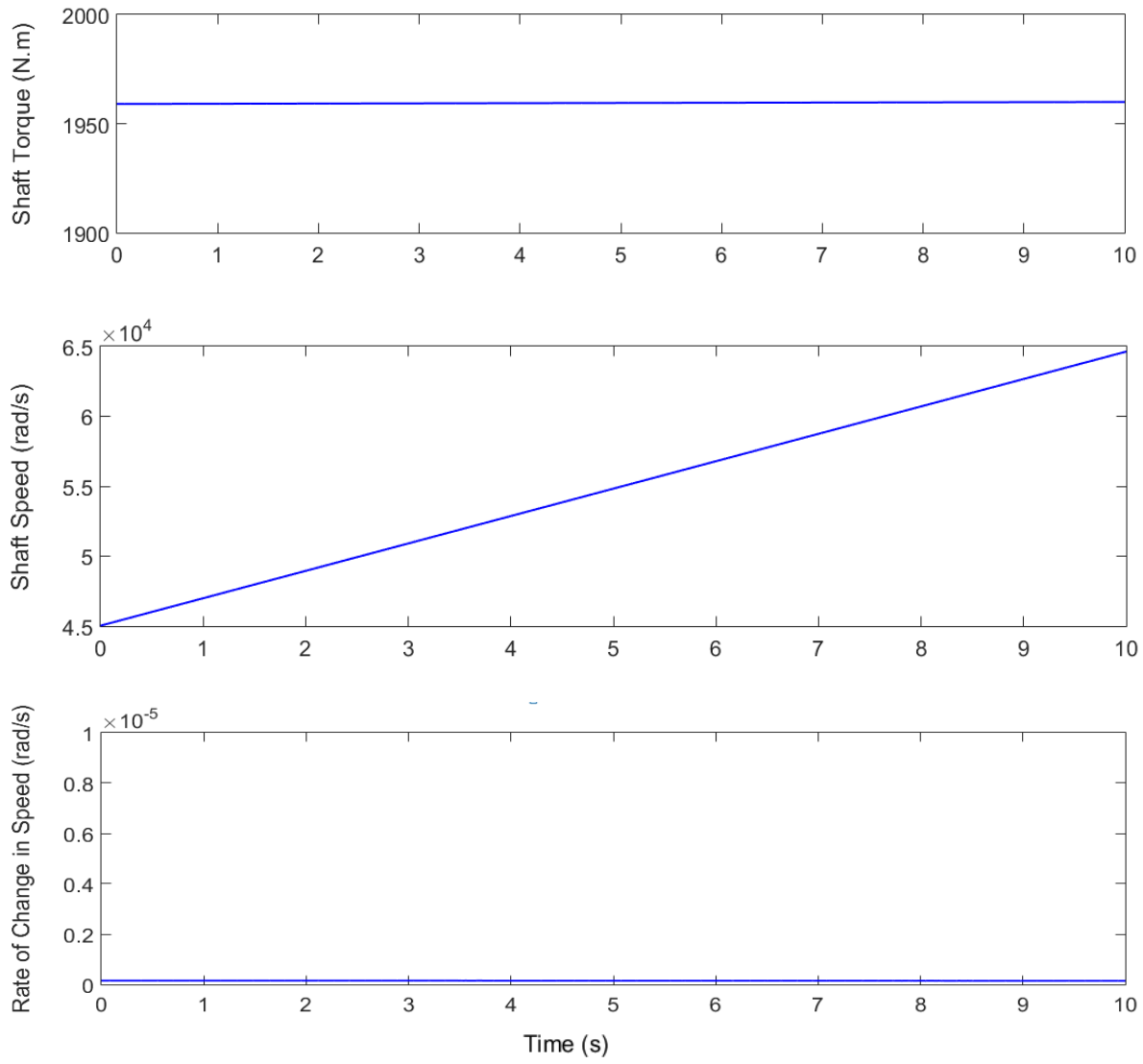

Figure 4.3: Torque, speed and derivative of angular speed of the flexible shaft [20].

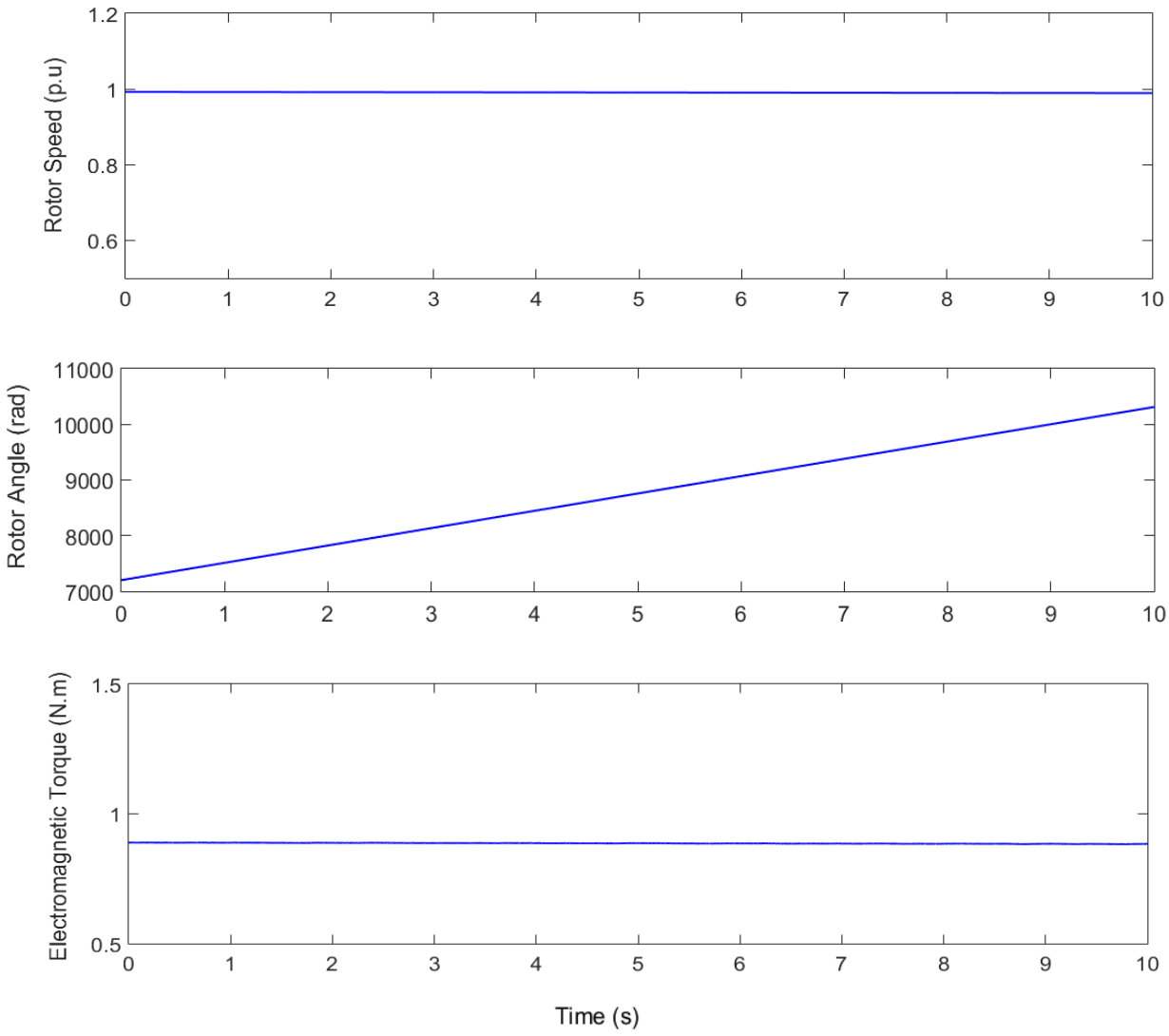

Figure 4.4: Rotor speed, angle and EM torque of the PMSG (flexible shaft) [20].

The simulation result shows the WT system converges to the steady-state condition including the drivetrain system. The control frequency can interfere with the anti-resonant and resonant frequencies, as shown in Figure 4.1. Although the interaction of the anti-resonant and resonant frequencies with the control frequency, placing an LPF within the controller and tuning the control gain should be considered to avoid interference between the controller frequency and the valleys of anti-resonance and resonance frequencies.

Case 2: rigid shaft

The stiffness coefficient of the rigid shaft is given in Appendix II. Without having an LPF, it perfectly shifts both valleys of anti-resonant and resonant to the higher frequencies in Figure 4.2. The stiffness coefficient of the rigid shaft is applied in the same WT system after Case 1. The results of Case 2 closed-loop response are given in Figures 4.5 and 4.6.

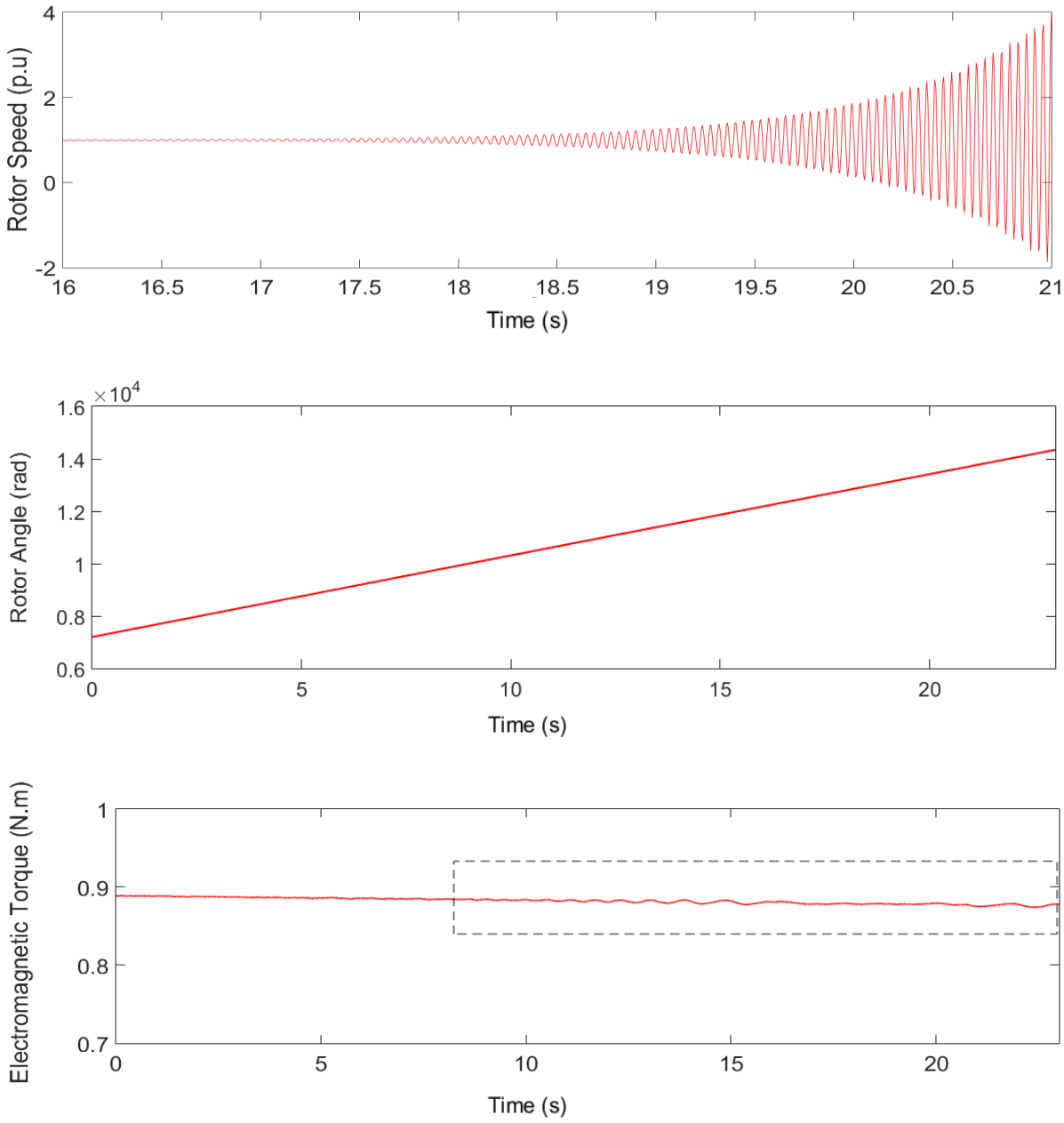

Figure 4.5: Rotor Speed, angle and EM torque of the PMSG (rigid shaft) [20].

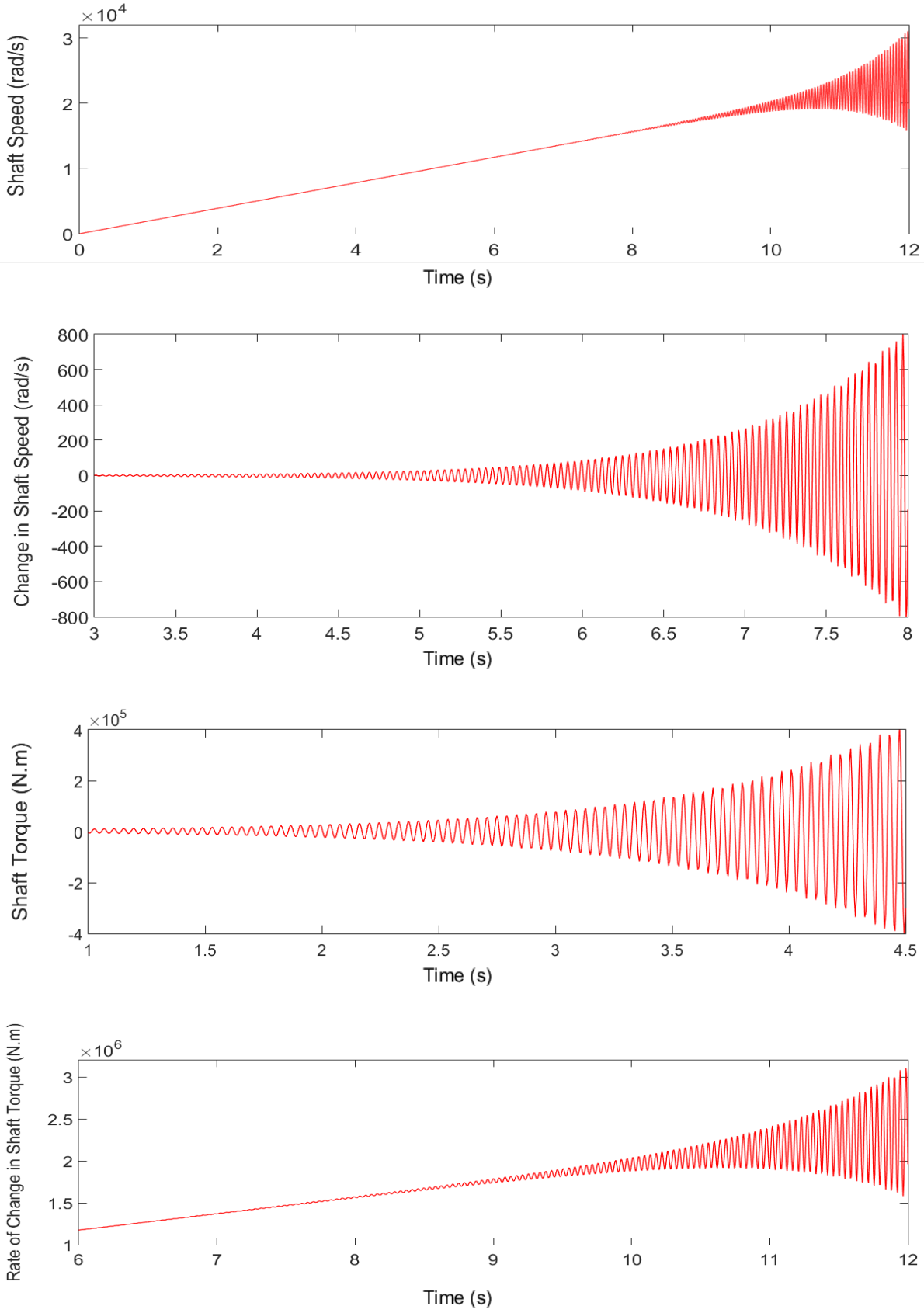

Figure 4.6: Speed, derivative of the speed, torque ($T_{sh} = T_{wt} - T_{pm}$) and derivative of the rigid shaft torque [20].

4.1.3 TO Analysis

The simulation results in Figures 4.3 to 4.6 depict the torsional oscillation between the shaft and the PMSG, which led to system instability for Case 2. As shown in Figure 3.3 from the previous chapter, the coupling torque on the shaft, T_{sh} is given in Equation (3.12). As Figure 4.2 (a) depicts, the damping response with the rigid shaft is negligible. Thus, T_{sh} determined by the angular displacement between the WT and PMSG rotors is defined:

$$T_{sh} = C_{sh}(\theta_{wt} - \theta_{pm}) \tag{4.1}$$

Assuming the friction of the WT and PMSG is negligible, Equations (3.10) and (3.11) become:

$$I_{wt}\frac{d^2\theta_{wt}}{dt^2} = T_{wt} - T_{sh} \tag{4.2}$$

$$I_{pm}\frac{d^2\theta_{pm}}{dt^2} = T_{sh} \tag{4.3}$$

Defining $\theta = \theta_{wt} - \theta_{pm}$, subtracting Equation (4.3) divided by I_{pm} from Equation (4.2) divided by I_{wt} gives:

$$\frac{d^2\theta}{dt^2} = \frac{1}{I_{wt}}T_{wt} - \frac{1}{I_{wt}}T_{sh} - \frac{1}{I_{pm}}\,T_{sh} \tag{4.4}$$

Substituting Equation (4.1) into Equation (4.4) yields:

$$I_{pm}\frac{d^2\theta}{dt^2} = \frac{1}{I_{wt}}T_{wt} - \frac{I_{wt} + I_{pm}}{I_{wt}I_{pm}}C_{sh}\theta \tag{4.5}$$

For steady-state operation, the rate of change of the angular momentum build-up in WT rotor is expressed as a function of the WT rotor speed:

$$\Delta L = \int \sum T_{wt} = f_{T_{wt}}\left(\frac{d\theta_{wt}}{dt}\right) \tag{4.6}$$

The function of the WT rotor torque is defined in Appendix V.

During torsional oscillation between the WT and PMSG rotors, the oscillating component of the larger inertia would be less likely to experience instability induced by the torsional torque. Therefore, the PMSG is referred to as the system average of the mechanical synchronous speed of the system:

$$\frac{d\theta_{wt}}{dt} = \frac{d\theta_{pm}}{dt} + \frac{d\theta}{dt}$$

$$= \omega_{pm} + \frac{d\theta}{dt} \tag{4.7}$$

A Taylor series expansion (TSE) is used for analysing the limits of this drivetrain system. Considering only the first term and discarding the higher-order terms of the TSE, the function $f_{T_{wt}}(\omega_{wt})$ at the point ω_{pm} is expressed:

$$\frac{d^2\theta}{dt^2} - \frac{\gamma}{I_{wt}}\frac{d\theta}{dt} + \frac{I_{wt} + I_{pm}}{I_{wt}I_{pm}} C_{sh}\theta = \frac{1}{I_{wt}} f_{T_{wt}}\left(\frac{d\theta_{wt}}{dt}\right) \tag{4.8}$$

where γ is the rate of change of the torque-speed curve of the PMSG, which is the numerical derivative of the torque-speed curve. It is not the same as the torque-speed curve of the WT.

The resulting eigenvalues of the shaft are then defined:

$$\lambda_{sh} = \frac{\frac{\gamma}{I_{wt}} \pm j\sqrt{-\left(\frac{\gamma}{I_{wt}}\right)^2 + 4 \cdot \frac{I_{wt} + I_{pm}}{I_{wt}I_{pm}} C_{sh}}}{2} \tag{4.9}$$

Positive $\gamma > 0$ yields the positive first term indicating the eigenvalues are on the right-half of the complex plane and unstable. Thus, the shaft undergoes negative damping and the increase in the torsion response shown in Figures 4.5 and 4.6 occurs. From Equation (4.9), the unstable torsional oscillation can be also identified in the frequency domain.

Since the i^{th} eigenvalue, λ_i, is related to the i^{th} natural frequency, the oscillation frequency f_{sh} is defined:

$$f_{sh} = \frac{\lambda_i}{2\pi} \tag{4.10}$$

Substituting Equation (4.10) into Equation (4.9) yields:

$$f_{sh} = \frac{1}{4\pi} \pm j\sqrt{-\left(\frac{\gamma}{I_{wt}}\right)^2 + 4 \cdot \frac{I_{wt} + I_{pm}}{I_{wt}I_{pm}} C_{sh}} \tag{4.11}$$

Since γ is the rate of change of torque-speed, the first term under the square root of Equation (4.11) is much smaller than the second term. Therefore, I_{wt} and C_{sh} dictate the oscillation frequency. When $I_{pm} > I_{wt}$, I_{pm} and C_{sh} dictates the oscillation frequency of the shaft. In either case, the stiffness of the shaft is always the dictating parameter in the drivetrain system.

In addition, γ is useful in torque control design of the PMSG. From Equation (3.30), assuming the rotor flux linkage is constant, the mechanical torque of the PMSG rotor only depends on the speed of the PMSG. As shown in Figure 4.5, the indication of the growth of oscillation can be seen by monitoring the rate of change in variable γ. This outcome is shown in Figure 4.7.

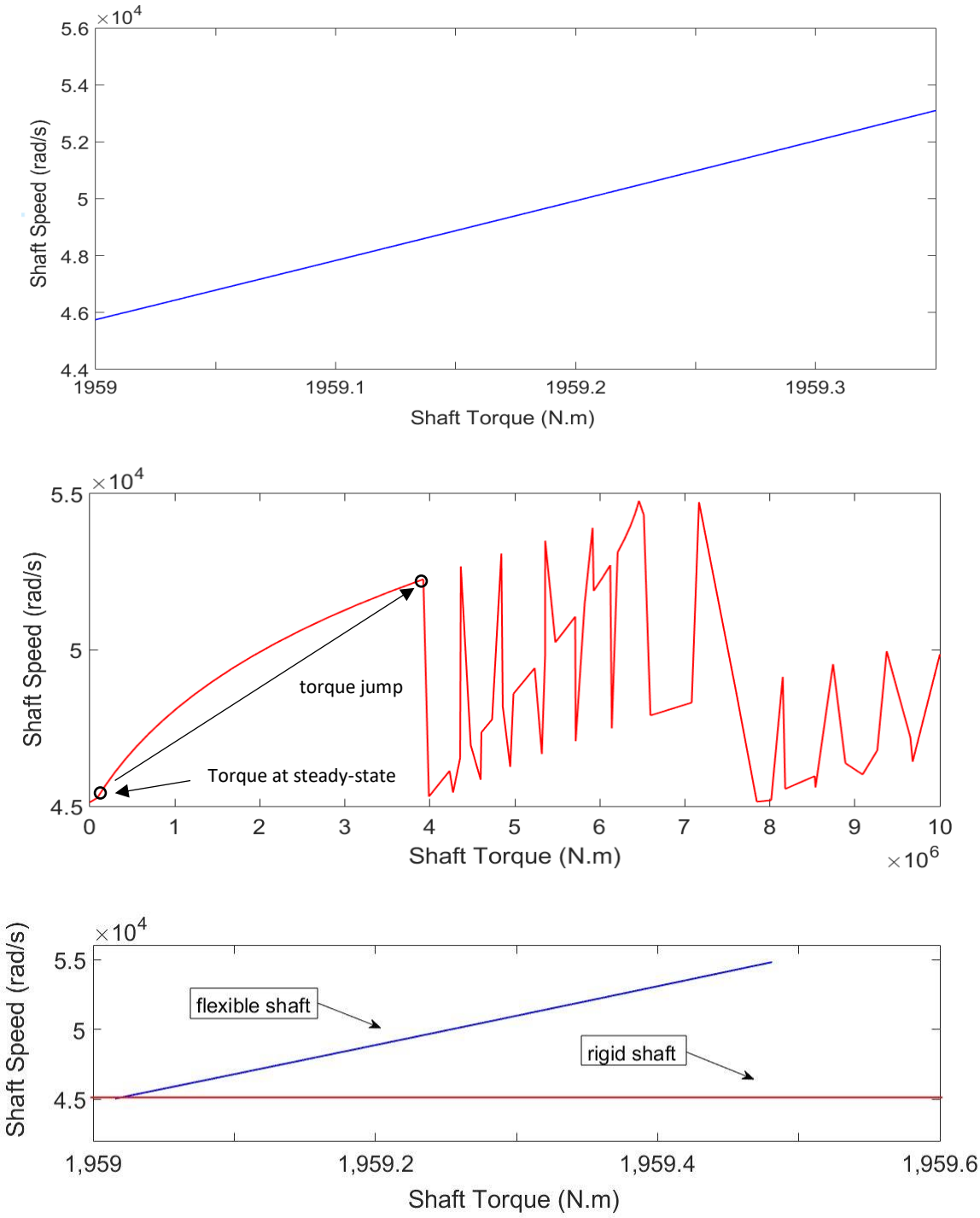

Figure 4.7: Torque-speed curve (flexible shaft), torque-speed curve (rigid shaft) and torque-speed curve of flexible shaft vs. rigid shaft (near steady-state operating point) [20].

It has been shown that when γ is positive and large, the system will result in negative damping and instability. As shown in Figure 4.7, the speed of the shaft is nearly insensitive to the change in torque. However, the oscillation of the shaft quickly builds up and exhibits negative damping, which leads to system instability. However, if γ is positive but very small (close to zero), the growth rate of the oscillation of the shaft system may be slower, although it still leads to an unstable system condition after a greater period of time.

This drivetrain simulation shows the effect of TO in the drivetrain system. The negative damping behaviour on the drivetrain system occurs due to the shaft stiffness resulting in the strong coupling between the rotating masses and the stiffness of the shaft system. The resulting oscillation in the shaft is large enough to make the system unstable in this particular WT system. The simulation shows sustained torsional oscillations result in catastrophic failure of the entire system.

4.2 Sub-Synchronous Control Interaction (SSCI)

Sub-synchronous control interaction (SSCI) is defined as the interaction between an electronic controller within a WT system and series compensated transmission system to create oscillation in the WT system and the grid [166]. The initial SSCI phenomena, which lead to voltage collapse of the grid is reported in [167] where doubly-fed asynchronous generator (DFIG) based WTs are interconnected to the weak grid. In addition, it is possible the oscillation frequency of the SSCI overlap to anti-resonant or resonant frequencies of the drivetrain system, as seen in the previous section. The SSCI phenomena between the WT and grid is simulated via three-phase grid faults, as shown in Table 4.1.

TABLE 4.1: GRID CONDITIONS AND FAULT TYPE.

Parameter	Value
System Frequency	50 Hz
SCR	2.75
Voltage	33kV
Cable Length	97km
Unit Transformer	2.5 MVA (33/0.69 kV)
Fault type / duration (t_{fault})	3ph-balanced / 400ms

A three-phase balanced fault was applied to the cable with duration of 400ms to excite a system transient, as shown in Figure 4.9. The breaker on the unit transformer was opened with 5ms delay, typical for CB actuation delay [165], after the fault is applied. The system is reconnected to the grid and synchronised at 8.4s. System oscillation was observed immediately after synchronising with the grid. This simulation model does not include protective relays and other protection devices placed in the WT system in order to observe interactions between the electrical component and the mechanical component.

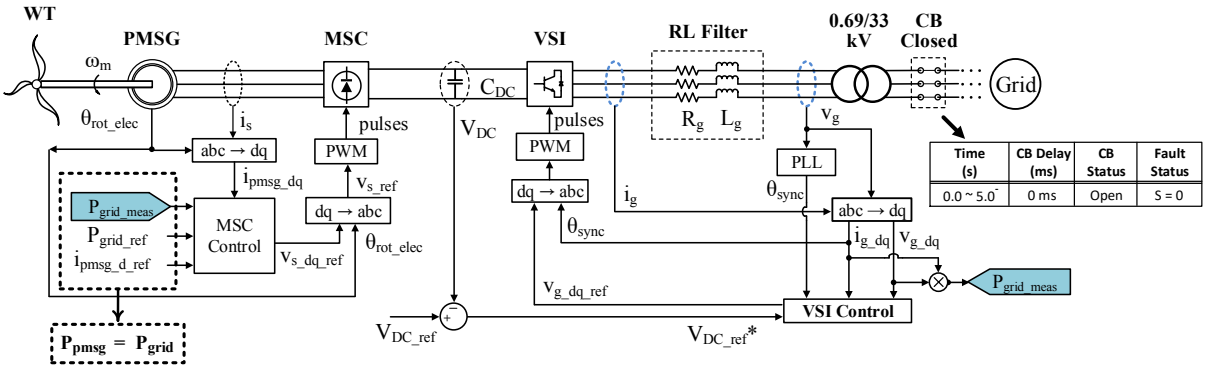

Figure 4.8: Configuration of the type-4 WT system and CB status during the steady-state operating condition.

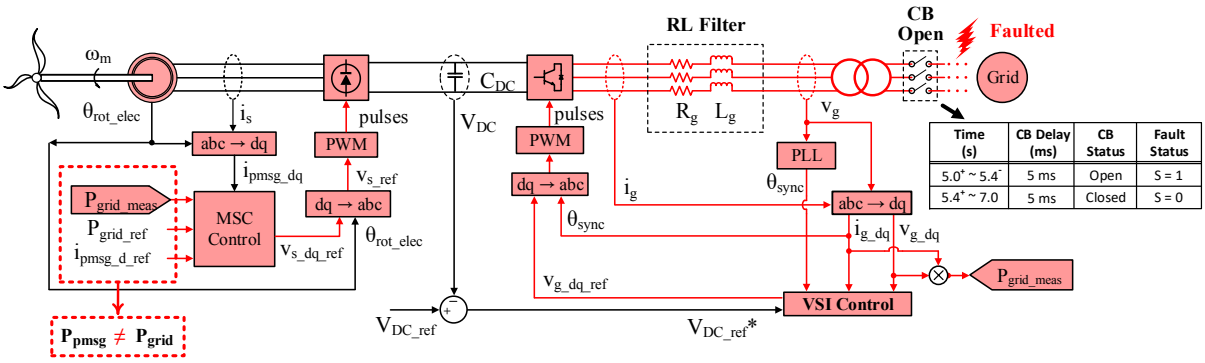

Figure 4.9: Components affected by the grid fault.

4.2.1 Simulation result – voltage and current oscillation

The simulation results of the grid fault are shown in Figures 4.10 to 4.14. Undamped oscillations develop in voltage, current, modulation index, and PMSG. The oscillations shown

in Figures 4.11 and 4.12 do not grow. The presence of the oscillation on the grid voltage is minimal, as shown in Figure 4.12.

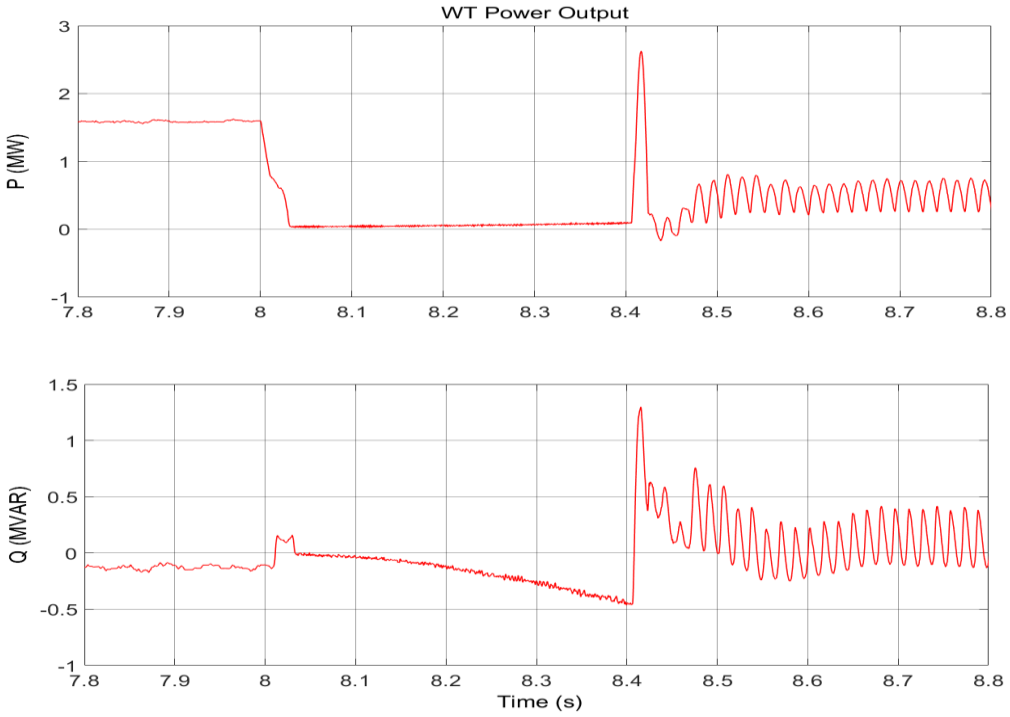

Figure 4.10: PMSG terminal real and reactive power.

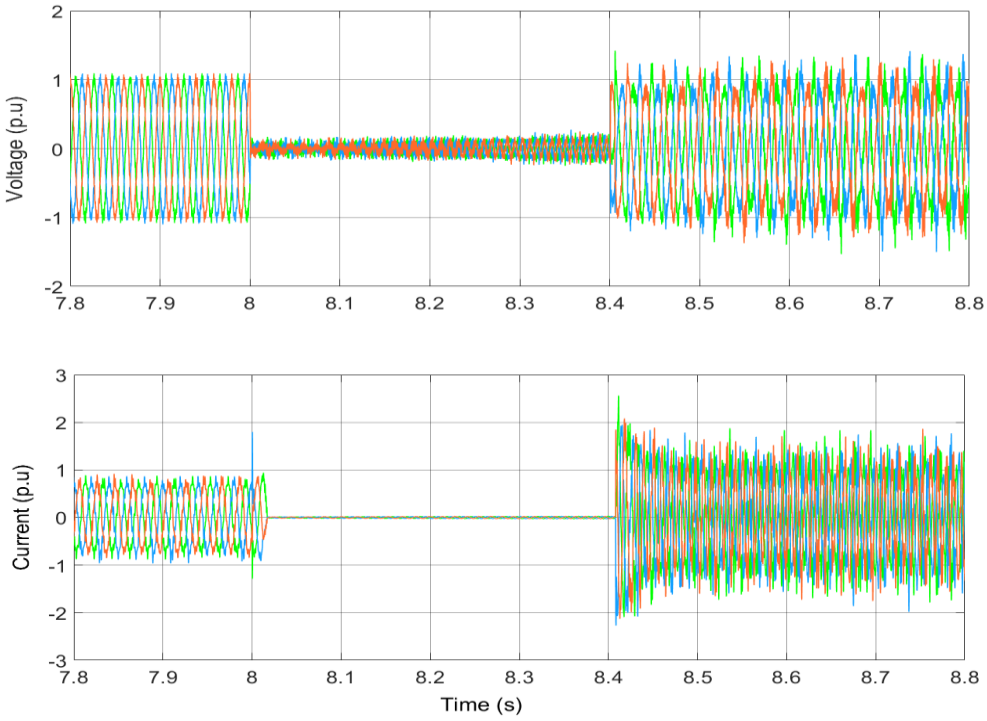

Figure 4.11: VSI terminal voltage and current.

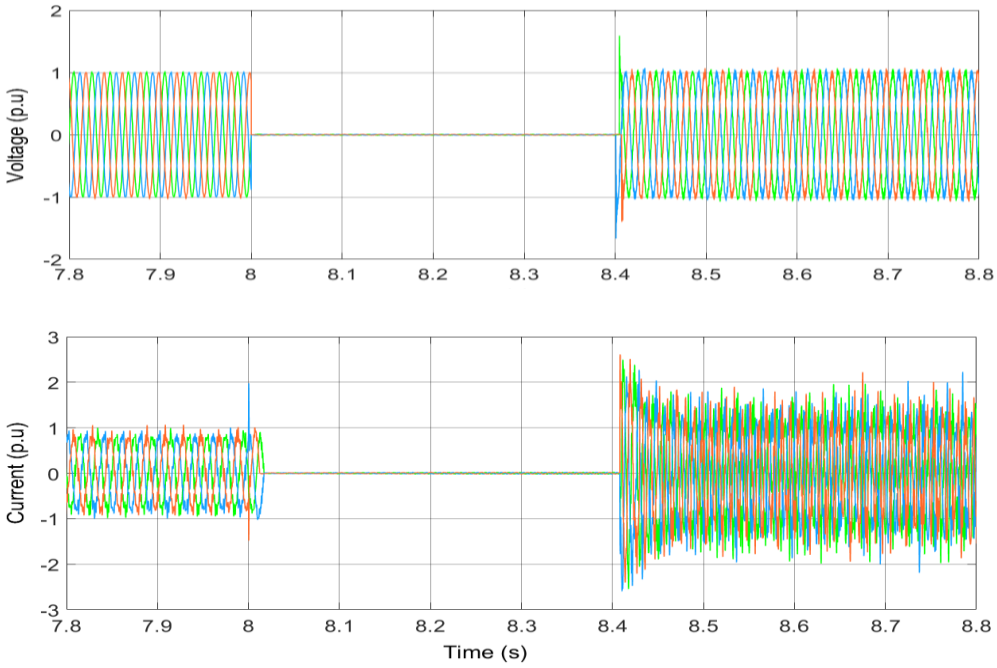

Figure 4.12: 33kV grid voltage and current.

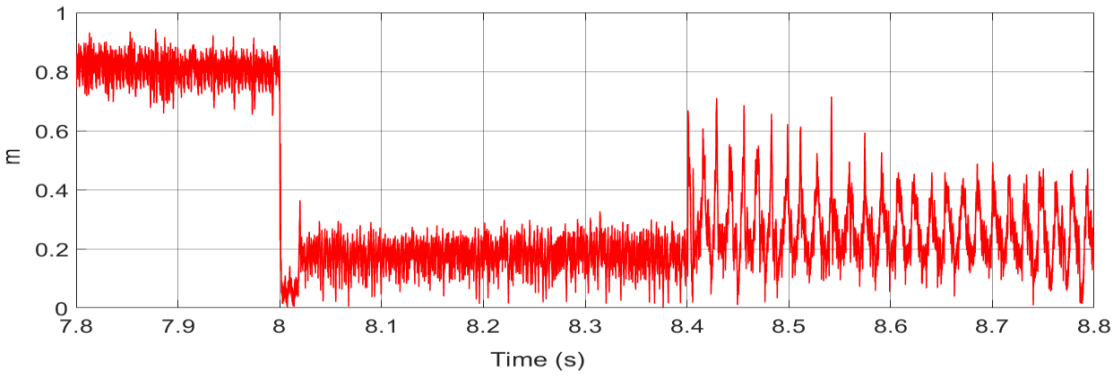

Figure 4.13: Modulation index of VSI controller.

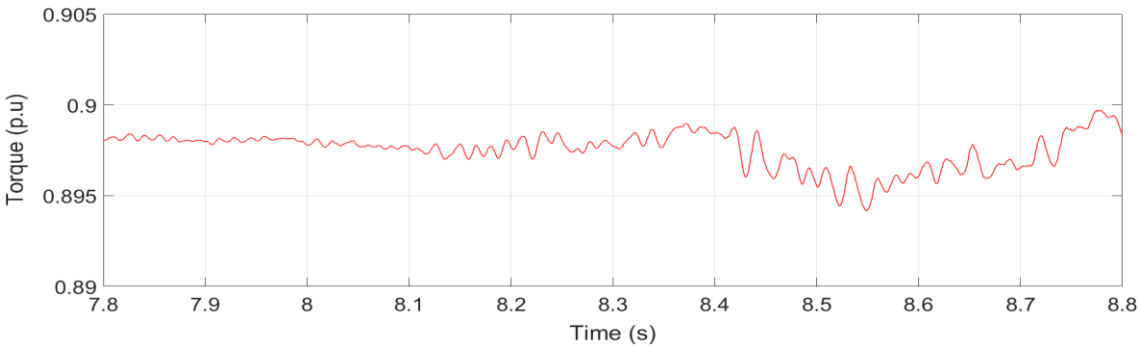

Figure 4.14: EM torque of PMSG.

The initial oscillation begins with the modulation index shown in Figure 4.13, and it fails to recover to the steady-state condition after the fault has been cleared, as shown in Figure 4.10. Figure 4.14 depicts the result of the current oscillation in the PMSG rotor. The relay would have picked up the continuous overcurrent condition, as shown in Figures 4.11 and 4.12, but it may not have picked up if the magnitude of the oscillation is small. If there is no protection operation, as in this simulation, the voltage and current oscillations continue until some component finally becomes damaged, which would require shutting down the WT for the repair. It is also possible the power quality of the weak grid is poor, so the protection system may not detect the oscillation if the variations of the voltage and current are small enough to fall into marginal thresholds of the relay setting.

This simulation shows the oscillations are most evident in the voltage, current, and modulation index, but the PMSG possibly exhibits the physical damage if the TI continues without being suppressed. The voltage oscillation is still significant up to the grid-side RL filter. However, it occurs to a much lesser extent than current oscillations.

4.2.2 Power balance equation

A vast majority of voltage source inverter (VSI) controls for wind farms use the power balance equation as the base model, as shown in Chapter 3. The DC link voltage dynamics are described using the power balance method. For wind turbine applications, the voltage on the DC-link capacitor is the voltage from the grid and the PMSG generator. This inherited capacitor voltage implies the capacitor voltage v_{Cdc} depends on both grid and generator voltages. In the majority of small-signal modelling, typically for HVDC applications, the DC link voltage is considered a constant voltage because it stays nearly constant during steady-state operating conditions.

However, for transient models, the grid voltage and the generator voltage fluctuate significantly during large-signal disturbances. The magnitude of voltage fluctuation depends on the transmission line or cable impedance and type of faults. For instance, if there is a three-phase fault on the grid side, the voltage on the grid side drops to the minimum voltage that fault ride-through requires in which the generation system must stay connected to transmission system under certain operational voltage level. In this case, the power balance equation becomes no longer valid. The WT keeps generating the power, but the grid is disconnected from the WT. As a result, the WT is isolated from the grid and operates independently.

Control of WTs is complex [149], [150] and the specific form of control method used in this simulation is typical and has been well-documented [151], and is widely used in research and

applications [149]-[155]. The typical control mechanism, and many other control algorithms, used in this simulation are not seen to be effective for an extended period of grid fault considering typical fault length of line-to-ground is 100~150ms. Their failure occurs because the location of the measurement sensors is located on the grid side. Due to the basis of the VSI control model, the cause of the oscillation is not traceable to how the system responds to the control action.

4.2.3 Phase-locked loop (PLL) and feedback control structure

Although PLL and PWM are different components, PWM is primarily affected by PLL and dependent on it, as shown in Figure 4.15. Conventional grid-side converter control systems using PLL and PWM algorithms may perform well in the steady-state and moderate transients. However, large transients of the AC system would cause nonlinear control system saturation. This control saturation adjusts the firing pulse of the phase-locked control and PWM modulation.

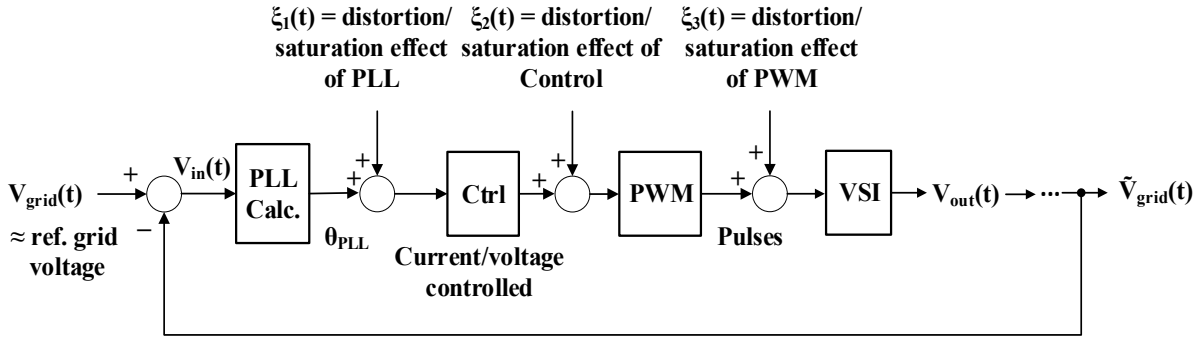

Figure 4.15: Feedback arrangement of VSI control system components.

The feedback control mechanism of the converter control shown in Figure 4.16 would maintain the system stability and function correctly in the steady-state and for small to possibly moderate disturbances. However, any large transient, such as grid fault can cause the voltage-controlled oscillator (VSO) to permanently lose synchronism with the grid because the faulted low voltage of the grid provides a large error margin, which is out of the controllable range.

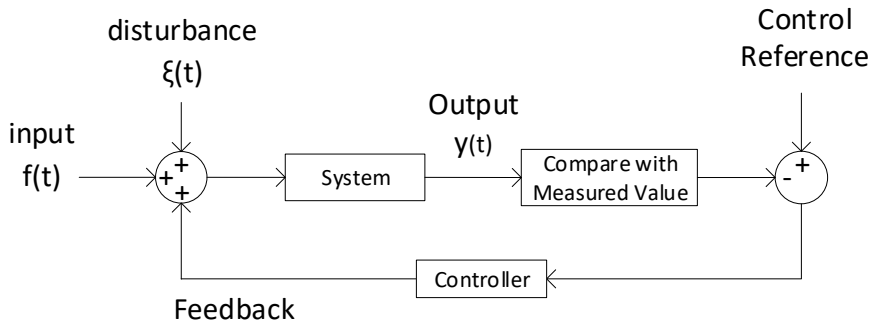

Feedback Control Mechanism

Figure 4.16: Structure of Feedback Control

Ainsworth et al. [156] discussed about "harmonic instability" where converters connected to a weak grid can lose synchronism with the grid frequency, whether those converters are based on mercury-arc valves or thyristors. He stated : "… *this is prevented by the use of phase-angle limit stops, which have a similar effect to those used on other control systems, in that two limits of firing angle, α are provided, outside the typical range (e.g., at α = 0° and α = 180°) beyond which the firing pulses cannot travel, even if voltage V, has a large positive or negative value due to saturation of the feedback loop. In consequence, in the steady state, oscillator frequency is always 6f, even if the feedback loop is saturated, and the oscillator cannot jump out of step. The limits of α = 0° and 180° operate instantly but are usually suitable only for "emergency" use in violent transients*" [157].

In short, PLLs try to synchronise with the reference signal and lock to the reference values. When the measured grid voltage exhibits large disturbances compared against the reference grid voltage, PLLs may become saturated, and the output of the PLLs may not be traceable. Ainsworth solved the problem by changing the firing angle from the converter controller. However, this solution may be used for particular small-signal harmonic problems, but may not be adequate to apply to the largely disturbed system environment like grid faults. The FFT of the simulation result shown in Figure 4.17 also clearly shows the SSCI is not a "*harmonic instability*" problem, limiting this solution's efficacy.

In particular, Figure 4.17 shows the frequency of the current oscillation at the peak magnitude is not a multiple of the fundamental frequency of 50 Hz. Instead, it shows interharmonic current characteristics [58], [158]. These results confirm it is not a harmonic instability problem.

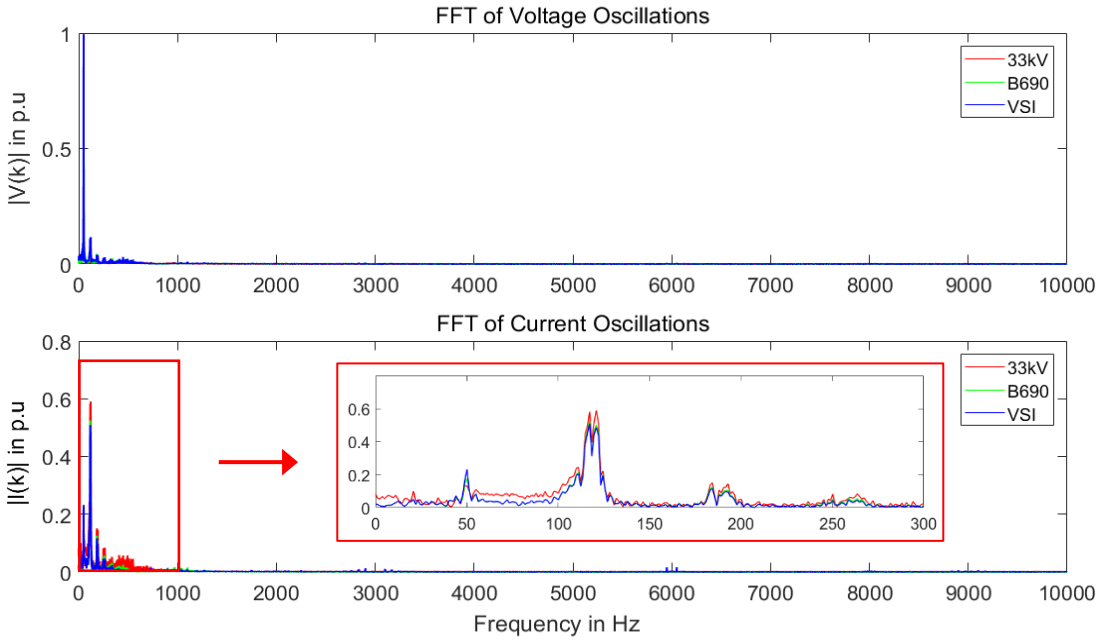

Figure 4.17: FFT of oscillating voltage and current between 8.4s and 9.0s showing interharmonic current.

Later, Göksu et al. [159] discovered the instability of grid side converters of wind turbine applications as loss of synchronisation (LOS) of PLL during large voltage transients at the point of common coupling (PCC), as shown in Figure 4.18. Their transient case study was nearly identical to Ainsworth's observation, and the step response of the voltage and current waveforms at the PCC seems very close to the measured waveform shown in [160].

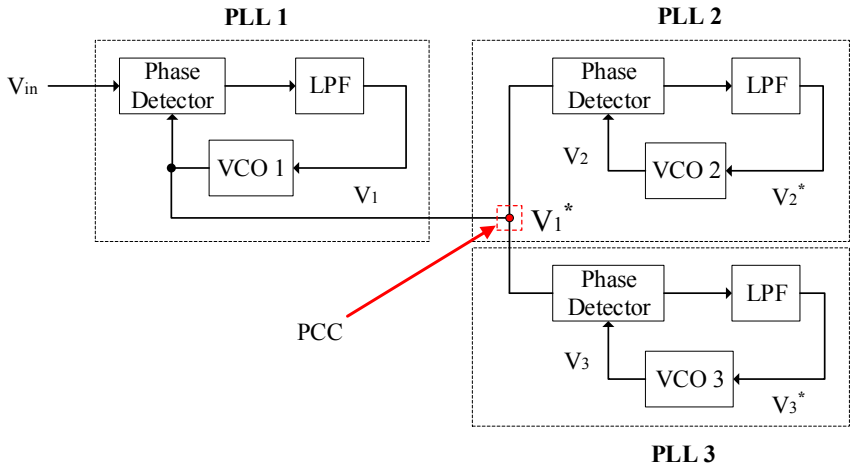

Figure 4.18: Multiple PLLs in a series and parallel connection showing LOS at PCC.

The main point is any large transient could cause the PLL to lose synchronism with the AC system due to the principle mechanism of phase-locked controls, where the reference in this case is the grid voltage, which is a large transient voltage in this case. Clearly, the LOS problem in PLLs is related to all control problems due to the feedback control structure shown in Figure 4.15. The disturbance is sustained in the converter system through closed-loop control paths, which alter the switching duty cycle [161].

To investigate the contribution by control actions, each node of components needs to be listed as a block diagram. Figure 4.15 for VSI and Figure 4.19 for MSC show the system arrangement of the feedback control system. In this figure $\xi_n(t)$ is the effect of distortion or saturation and $v(t)$ is the reference voltage.

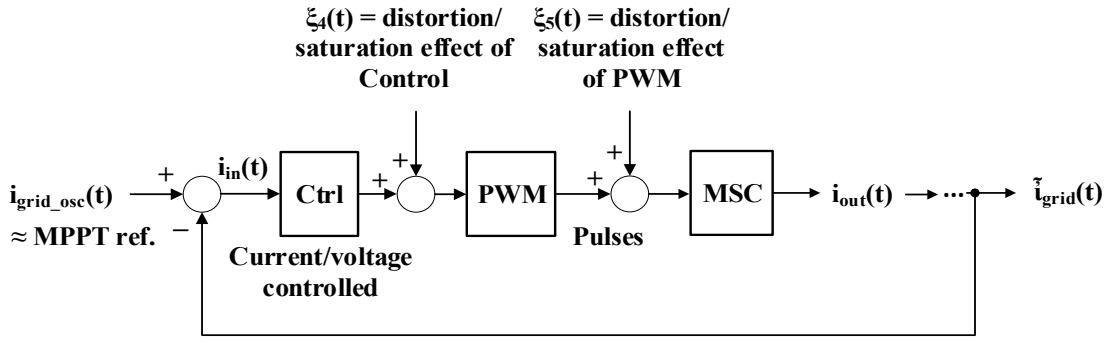

Figure 4.19: Feedback arrangement of MSC control system components

Figures 4.20 to 4.22 show the control diagrams for VSI, MSC and PLL used in this SSCI simulation. They all use the voltage and current from the grid as the input to their controllers.

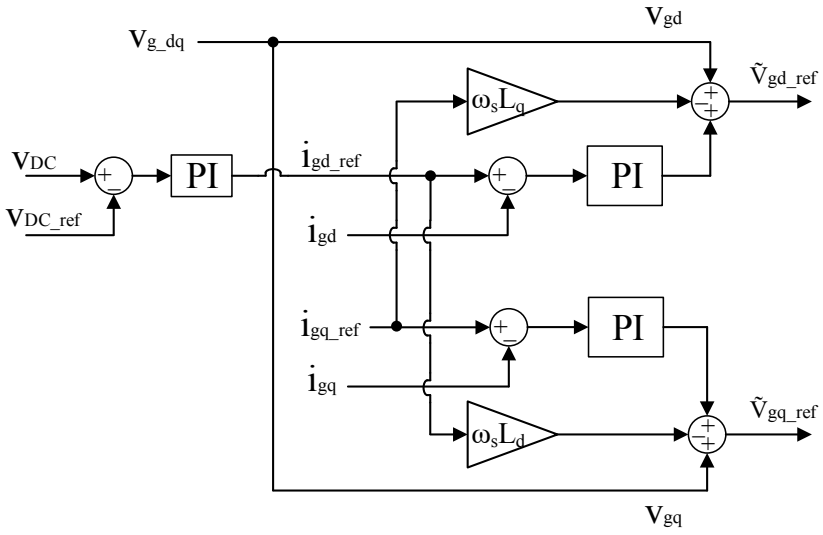

Figure 4.20: Control diagram of VSI

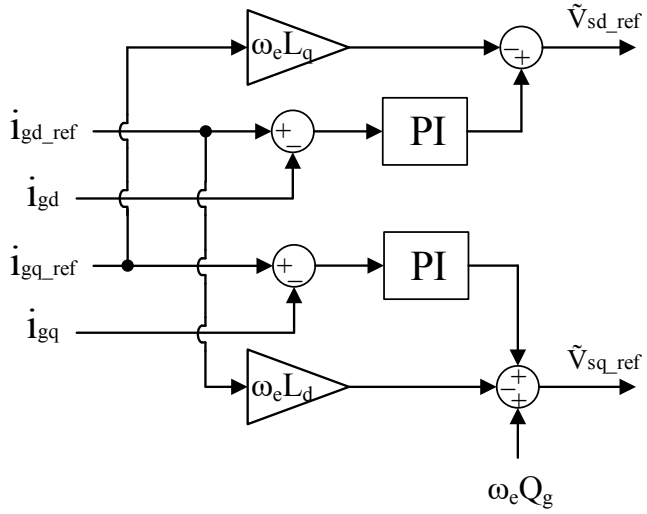

Figure 4.21: Control diagram of MSC

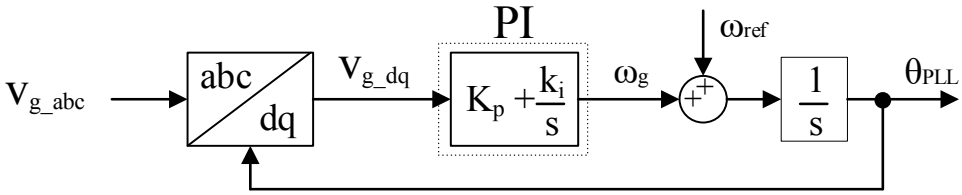

Figure 4.22: Feedback control structure of PLL

4.2.4 Current oscillation

From the control arrangement in Figure 4.15, the faulted grid voltage is sampled and enters the PLL, trying to calculate the phase difference. During the fault, the output of the PLL would not be the desired value because the input voltage is nowhere near the steady-state condition. The output of the PLL, which is another undesired value, becomes the input of the control system. This process repeats over and over during the grid fault.

The control system tries to minimise the difference between the measured and reference voltages by controlling the firing angle of the VSI. When the difference between these two voltages is large, and the fault duration is longer than typical faults ranging between 100~150ms, the output of the control system would depend on the grid voltage.

It is worth noting the grid fault problem is a large signal problem, rather than a small-signal problem. The control system possibly exhibits some saturation effects, which means the modulation index may go over the upper or lower limits the controller can handle. The saturation effects depend on the algorithms implemented in each component. Thus, every WT system can exhibit different saturation effects including limit cycles [162] on converters.

Modern WT control mechanisms include limiting functions to prevent the MSC or VSI exceeding PWM saturation [163], [164], which can cause unstable operation of the WT. The control input parameters (i.e., voltage and current) of the VSI obtained from the grid-side. The effect of the VSI control must exhibit in the control parameters including PLLs. The grid voltage and current are measured and used as the input to the VSI controller to keep the WT and grid. These controllers receive input parameters from the PLL to keep the angle between the PMSG and grid in phase.

To understand the current oscillation from the PMSG output, the control diagram of the MSC from Figure 4.21 is examined. Although the MSC and VSI controllers are independent, they both use the grid voltage and current as the control reference. Thus, if any oscillation or distortion is present in the grid, the controller tries to calculate the maximum power to generate based on the oscillating voltage. Therefore, the current starts oscillating, and the oscillating current is inherited to the PMSG input and output. This referencing of grid voltage and current from the grid is the problem with the maximum power point tracking (MPPT) control mechanism with the current control loop, as shown in Figure 4.23.

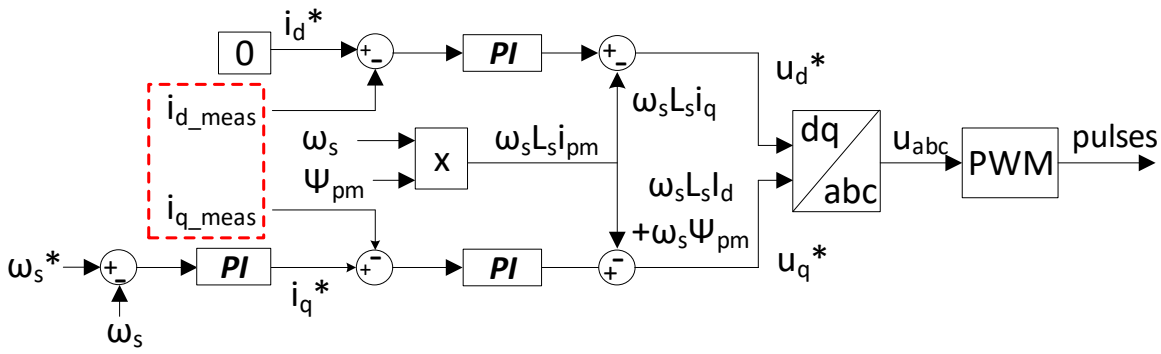

Figure 4.23: Feedback arrangement of MSC control system.

Since i_{dq_meas} is the measured and transformed from the grid current value i_{abc} to dq-axis, the difference in the magnitude from the reference current i^*_{abc} are very large due to zero power transfer via VSI. In addition, the resulting SSCI oscillation in T_{em} is shown in Figure 4.24, which has significantly different oscillatory characteristics than TO shown in the previous section.

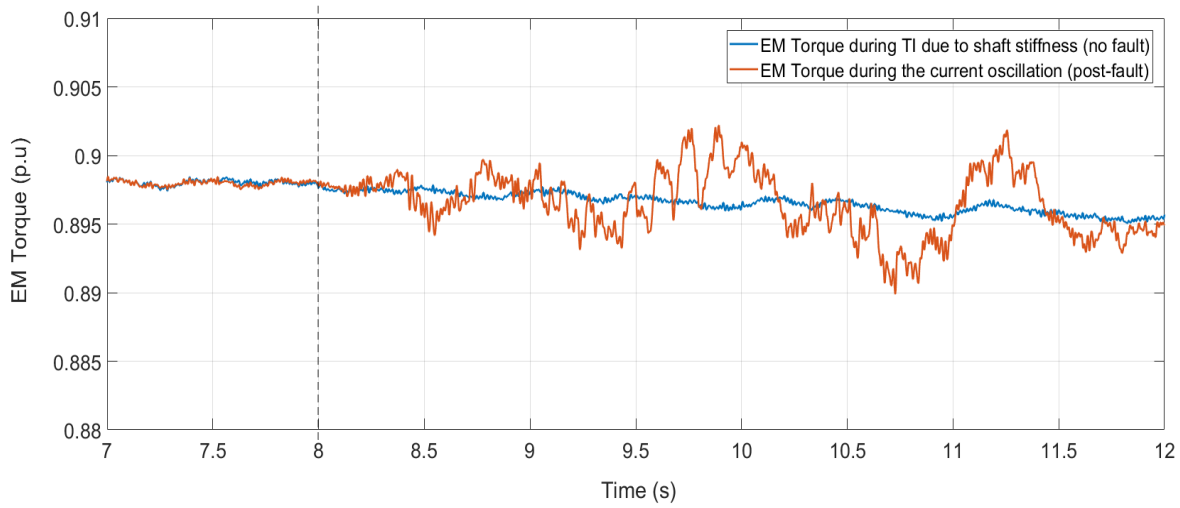

Figure 4.24: Oscillation comparison between SSCI and TO from the EM torques of PMSG.

4.3 Summary

The simulation results in this chapter show: 1) shaft failure in the drivetrain system by the TO; and 2) the system oscillation by the SSCI. The TO problem must be addressed and dealt at the system design level before energising the WT system. However, the SSCI problem is a problem

with the reference and input to the control structure using the faulted grid voltage and current values. However, changing the entire control structure of the controllers used in the WT system is not feasible because they all need to shut down. Therefore, an alternative method is proposed in the next chapter.

5
CONTROL

A novel control strategy to mitigate the post-fault oscillation due to SSCI is introduced in this chapter. The control method developed prevents oscillation build-up and extends the critical clearing time over conventional control methods [149], [150]-[155], [168]-[170]. Control system design is based on mostly steady-state operating conditions, because the interconnection between the grid and the WT and currently available control methods mentioned above are proven effective and robust in controlling harmonics for steady-state operating conditions. However, the vast majority of these controllers are not adequate to control WT systems during transient events.

Therefore, an alternative input to the controller is designed for grid fault conditions. MATLAB/Simulink® is used to design the controller. The presence of small voltage and current harmonics in the simulation model is neglected because it is not the main interest of this research.

5.1 Control Objectives

The most critical control objectives of overall WT system operation are similar in most WT control models [58], [153], [155], [170]. Many sub-synchronous control interaction papers [170]-[176] suggest and claim new control methods to mitigate the oscillation phenomena, but the oscillation they refer to does not present the same oscillation phenomena as seen in Chapter 4. Even the authors with the original SSCI recording [14] from real system measurements failed to duplicate the same post-fault oscillation from the recording. Instead, the authors presented a generic system oscillation, which is not the same phenomena as the post-fault oscillation.

Thus, the control objective, in this case, is to mitigate the post-fault oscillation, and primary to:

1) Compensate the low grid voltage during long period faults, which last much longer than the typical 100 ms. The target fault duration is 400 ms in which the oscillation occurs after the fault has been cleared.

2) Maintain the stable DC-link voltage during the grid fault without relying on DC choppers.

Compensation of the low grid voltage implies the faulted grid voltage should not be used as the reference voltage to synchronise the PMSG and VSI to the grid. All control methods for the VSI, MSC and PLL used in the WT system use the grid voltage as the input to the controller during the fault period. There are two primary components to control in this research, the PMSG and VSI.

In the VSI control, maintaining the DC-link voltage as close to the reference value as possible is considered as the primary goal. The performance of the new control strategy is compared to the control method in Chapter 4. Both steady-state and grid fault conditions, which caused the post-fault oscillation due to the SSCI, are presented in this chapter. For PMSG control, stable active power and maximum power point tracking (MPPT) values under the given wind speed are considered as the general goal. The q-axis control loop is devoted to PMSG speed and torque.

Assessing the overall system performance under steady-state conditions and transient behaviour when a three-phase fault occurs at the grid indicates the satisfying performance of both VSI and PMSG controllers in both conditions. In other words, no oscillation must be found in any grid fault condition in which the low voltage ride-though (LVRT) requirement

during the fault must be met. The controller of both controllers must fulfil the control objectives mentioned above.

5.1.1 Considerations for control strategy

I. PMSG current rise and oscillation

The measured current from the grid is compared to the maximum available power from the MPPT curve references: DC-link voltage and reference current. As the WT is isolated from the grid by the VSI during the grid fault, WT operation is not affected by the disturbance from the grid. Thus, the DC-link and the generator-side converter voltages are maintained.

This isolated WT operation causes control malfunction, as shown in Chapter 4. When the measured current from the grid is less than the available MPPT value, the controller tries to boost the current generation, as shown in Figure 5.1. Thus, when the measured current is less than the reference current value, the controller tries to boost the current generation. In other words, if the measured grid current exceeds the reference current value, the controller tries to decrease the current generation.

Therefore, it is vital to avoid the current measured from the grid and compare to the reference current values during the grid fault. Unfortunately, almost all conventional control methods mentioned above use the measurement values from the grid, which is used as the input of both controllers. This approach causes the SSCI and post-fault oscillations shown in Chapter 4. Hence, the new control input is defined and used for both VSI and PMSG in this chapter.

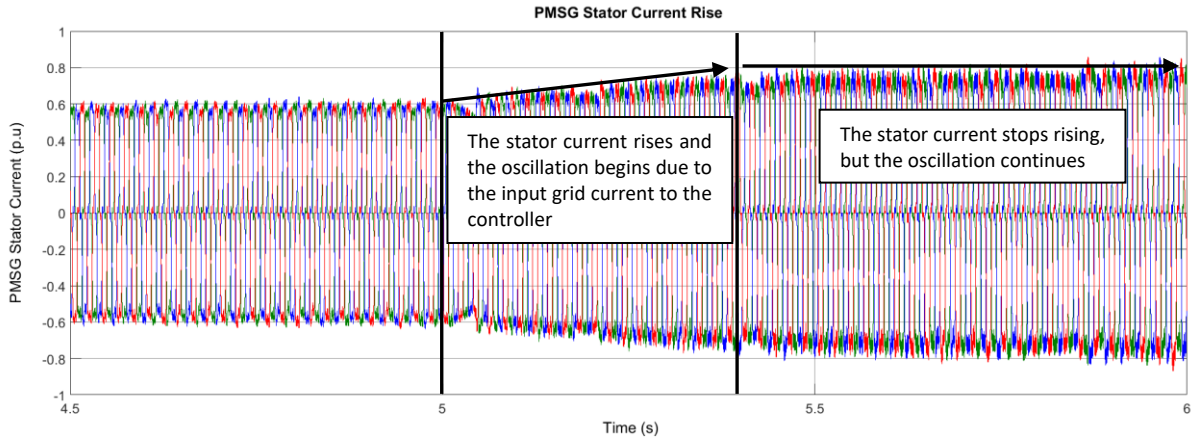

Figure 5.1: PMSG stator current rise and oscillation

II. DC-link voltage rise

Figure 5.2 depicts the DC-link voltage rise during and after the fault with the post-fault oscillation at 5.4 s. It indicates the controller fails to recover the WT system to the steady-state condition once the fault is cleared. The DC-link voltage rise can be more problematic than the oscillation if it keeps rising.

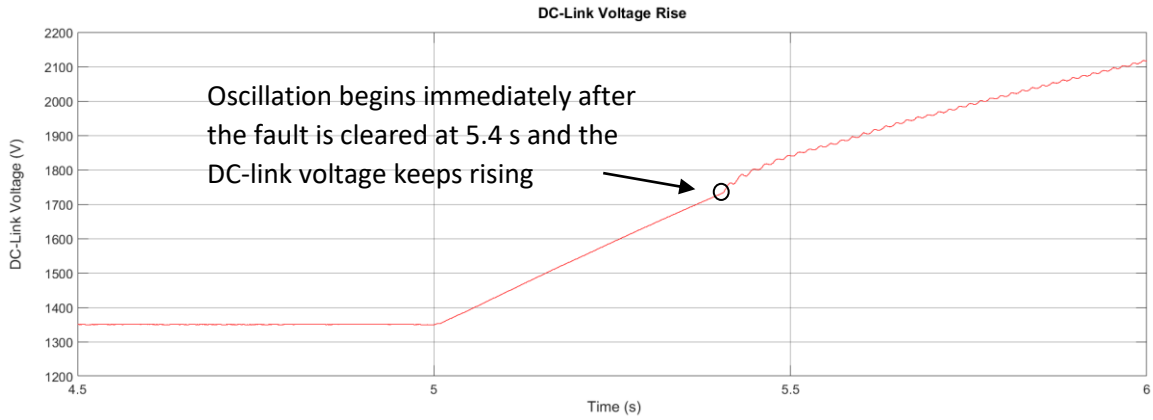

Figure 5.2: DC-link voltage rise and oscillation.

If the DC-link protection activates before any system component becomes damaged, the WT is again isolated from the grid. Rising DC-link voltage must be compensated or prevented with the crowbar/DC chopper protection, but this protection method does not prevent the oscillation. IEC 60871-1 [182] and ANSI/IEEE C37.99 [183] define the allowable voltage limit and time setting for the protection if the voltage exceeds the threshold. It provides a minimum duration at specified voltage factors, as shown in Table 5.1.

Table 5.1: IEC 60871-1 AND ANSI/IEEE C37.99 CAPACITOR OPERATION TIME.

Voltage factor Vn R.M.S (p.u)	Max. duration in the standard	Voltage conversion (Volts) * rounded up values
1.2	5 min	1620
1.3	1 min	1750*
1.4	15 s	1890*
1.7	1 s	2300
2.0	0.3 s	2700
2.2	0.15 s	2970*

In the case of a grid fault, the capacitor should withstand the specified overvoltage range during the fault for given time limits in Table 5.1. Thus, this overvoltage and time limit is also considered in the control design.

III. Voltage angles: grid and PMSG

As shown in Figure 5.3, the delay of voltage angle is even throughout the steady-state condition. It indicates the synchronism between the grid and PMSG terminal voltages.

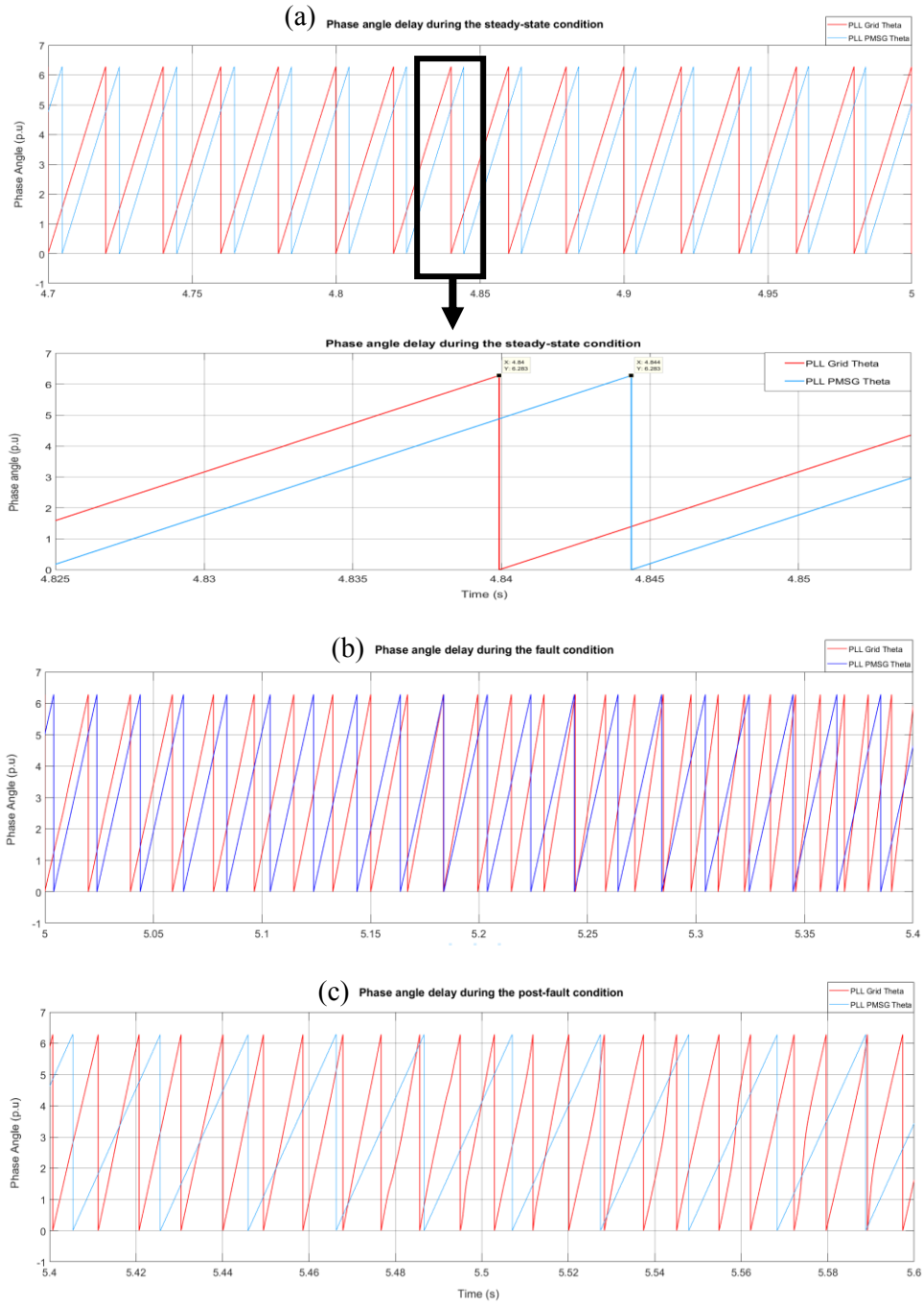

Figure 5.3: Voltage angle deviations: (a) steady-state, (b) during the fault and (c) post-fault.

During the fault, the delay angle of the grid voltage depicts random shifts of its angle in which the frequency of the voltage changes, whereas, in contrast, the PMSG voltage angle is stable. When the fault is cleared, the grid voltage fails to recover to the steady-state grid voltage and frequency. The oscillating voltage and frequency are shown in Figure 5.3 (bottom).

As shown in Figure 5.3, the phase angle delay appeared in the measurement between the PMSG terminal voltage and the grid voltage during the steady-state is uniformly constant. In contrast, the phase angle of the faulted grid voltage deviates and changes the frequency during the fault.

5.1.2 Control input definition

There are several prerequisite conditions to consider for the control design during fault conditions.

i. The actual real power from the PMSG transferred to the grid is zero, in which the power balance equation becomes no longer valid. However, the real power generated by the PMSG is NOT ZERO. ($P_{pmsg} \approx P_{grid}$ for steady-state, $P_{pmsg} \approx P_{rated} \neq P_{grid} \approx 0$ for fault conditions).
ii. DC-link voltage is maintained whereas the grid voltage is near zero at the measurement location.
iii. DC-link voltage and current rise during the fault. If the fault lasts long enough, the DC-link protection activates before any component gets damaged. The current generated by the PMSG is limited to its physical capability control threshold, as shown in Figure 5.1.
iv. The MPPT-based control mechanism should be preserved.
v. The input of PLL should NOT be the faulted grid voltage.

Conditions i and ii, are illustrated in Figure 5.4. Considering the conditions above, the operation logic is designed as shown in Figure 5.5.

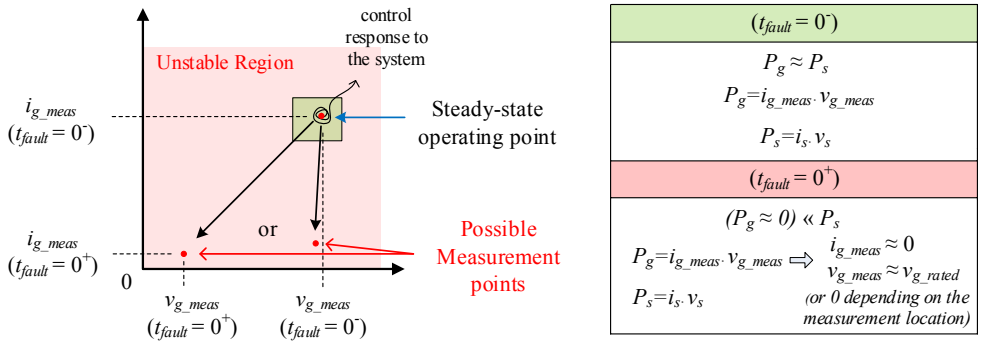

Figure 5.4: Measurement locations of the faulted grid.

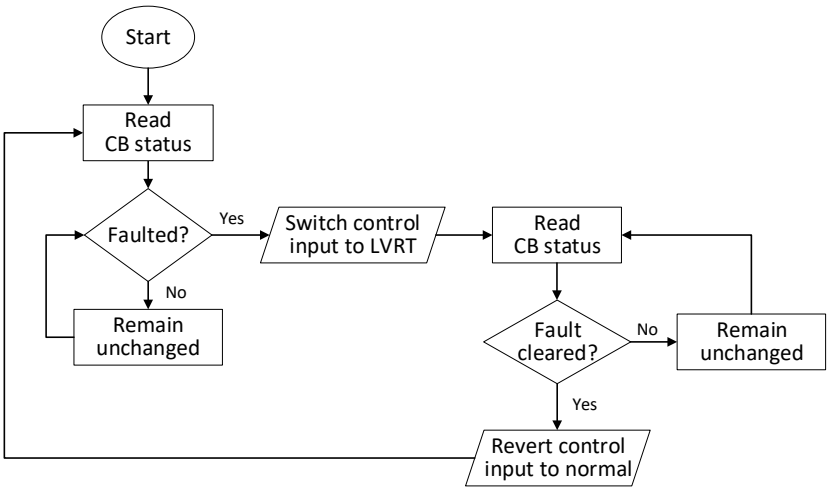

Figure 5.5: Process logic of LVRT control input switching.

5.2 Voltage Source Inverter (VSI) Control

For control of the steady-state condition, the simulation model used in Chapter 4 is employed. This control method works well with the steady-state condition with small perturbations in the system, such as ripples. For control strategy during the grid fault, the input voltage and current from the grid, as shown in Figure 5.6, are removed. This approach avoids comparing the voltage reference against the measured value of the grid voltage.

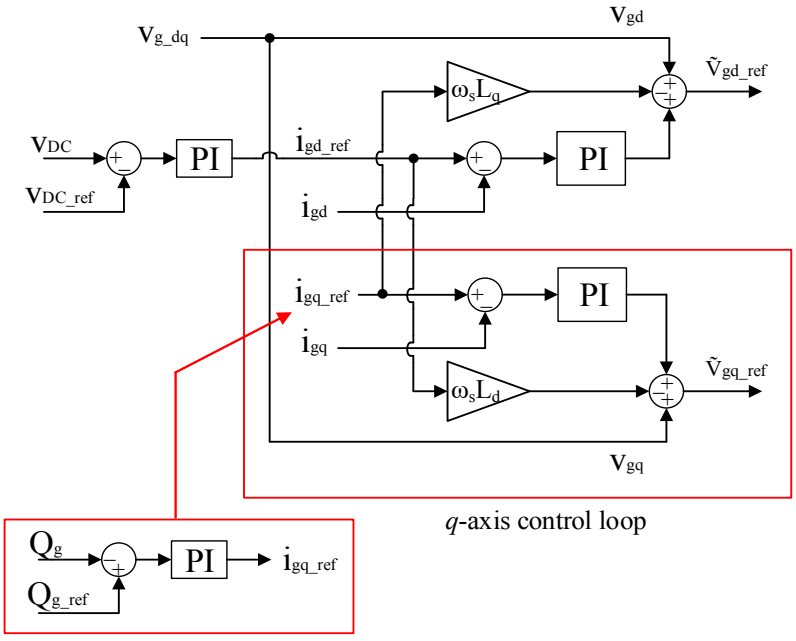

Figure 5.6: Typical control structure showing the input of the VSI.

5.2.1 Steady-state control of VSI

The typical structure of VSI control shown in Figure 5.6 works very well [184]-[189] for steady-state conditions, small-signal disturbances, and even some fault conditions when the WT is not connected to a weak grid. Although one control method may perform better than another in particular disturbance scenario, all these control approaches are still based-on the structure shown in Figure 5.6. The control equations based on Equations (3.46) and (3.45) are defined:

$$\tilde{v}_{gd} = v_{gd}^{*} - \omega_s L_{gq} i_{gq} + v_d \tag{5.1}$$

$$\tilde{v}_{gq} = v_{gq}^{*} - \omega_s L_d i_{gd} \tag{5.2}$$

The q-axis loop in Equation (5.2) controls the reactive power, and the d-axis loop of Equation (5.1) controls the DC-link voltage.

The operation of the VSI is required to stabilise the DC link voltage within a permissible operation limit. Considering the active power is the product of the DC-link voltage and the d-axis current of the grid side converter, the output signal of the DC-link is a reference signal for the d-axis current using the PI control as described in Section 3.7. By comparing d-axis current i_{gd} with its reference signal i_{gd_ref} via PI control, the reference voltage signal v_{gd}^{*} is calculated. Reactive power control is performed by the q-axis control loop when a voltage disturbance is observed at the grid. The VSI should then compensate the voltage variation by injecting reactive power to stabilise the voltage. Therefore, the reference q-axis current i_{gd}^{*} is obtained by comparing the transformed reactive power Q_{gd} with its reference Q_{gd_ref} via PI control. Finally, the decoupled voltages, $\tilde{v}_{gd}$ and $\tilde{v}_{gq}$ are obtained.

5.2.2 Transient control of VSI

The steady-state control of VSI works for all other WTs interconnected to the grid, except when it is connected to a weak grid, or the grid is faulted. Oscillating behaviours in wind farms are only observed from the interconnection to the weak grid, or grid fault has been cleared. Therefore, it is not recommended to connect VSI-based energy sources into the weak grid due to the voltage stability issues [177]. However, in some cases, interconnections to the weak grid are unavoidable, such as with the increasing number of offshore wind turbines [24].

In this case, an oscillation preventive control to mitigate the transient oscillation must be applied. The block diagram of the new control strategy is as shown in Figure 5.7.

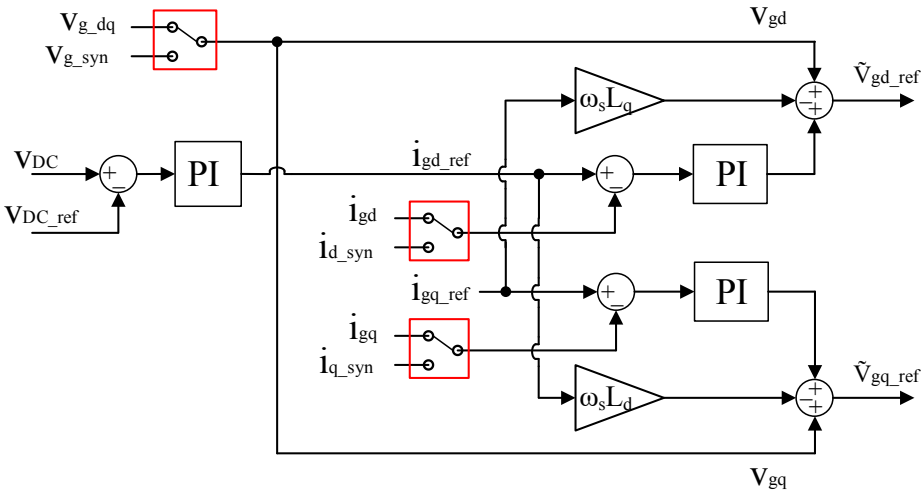

Figure 5.7: New control inputs of VSI,where the subscript syn means synthesised.

Instead of measuring the grid voltage and current, the new control signal is used as the control input. By removing the measured low voltage and nearly no zero current from the faulted grid, the controller does not try to synchronise the VSI output voltage to the faulted grid voltage.

5.3 Machine-Side Converter (MSC) Control

The output current of PMSG is controlled via speed and torque controllers. An active power control within maximum power point tracking (MPPT) value is considered in control objectives of the generator side converter [43]. Figure 5.8 shows the control loop of the MSC.

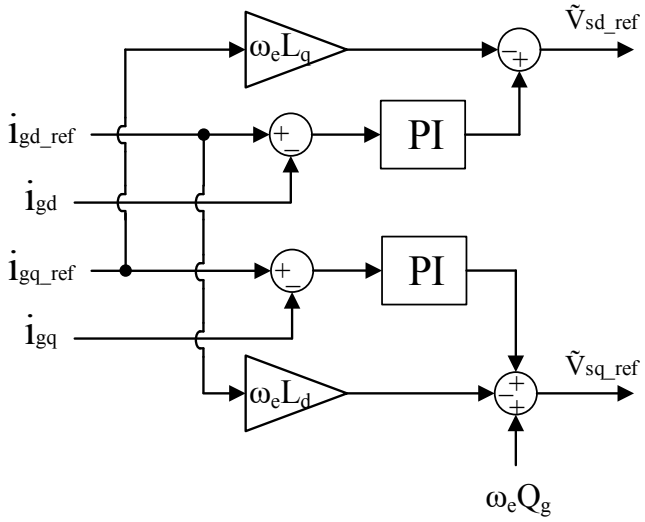

Figure 5.8: General control structure of MSC control system.

In this control diagram, the q-axis loop controls the PMSG speed and torque, and the d-axis loop controls to track the maximum available power from MPPT. The control of electromagnetic torque allows regulating the WT rotor and generator speed regulation, which enables variable speed control of the PMSG WT.

5.3.1 Steady-state control of MSC

For the steady-state condition, the same MSC model and control used in Chapter 4 is used. Based on Equations (3.24) and (3.25) in Chapter 3, the control equations are defined in terms of dq-reference frame:

$$\tilde{v}_{sd} = R_s(i_{sd}^* - i_{sd}) - \omega_e L_q i_{sq} \tag{5.3}$$

$$\tilde{v}_{sq} = R_s(i_{sq}^* - i_{sq}) - \omega_e L_d i_{sd} + \omega_s \psi_{pm} \tag{5.4}$$

As shown in Equations (5.3) and (5.4), i_{sq} and ω_s are coupled together and any change in ω_s will alter i_{sq}. The reference voltage of the q-axis, v_{sq}^*, is achieved by multiplying the stator resistance and the difference between the reference q-axis current and measured current, $R_s(i_{sq}^* - i_{sq})$. Consequently, the decoupled PMSG stator voltage equations, $\tilde{v}_{sd}$ and $\tilde{v}_{sq}$, are found from Equations (5.3) and (5.4).

5.3.2 Transient control of MSC

As shown in Figure 5.8, the MSC control structure uses the reference currents, i_{sd} and i_{sq}, to compare the power transferred from the PMSG to the grid. This approach is possible because this MSC control method is based on the assumption the grid voltage is steady-state and stable all the time. Therefore, the total power transferred from the PMSG and grid can be calculated by comparing the reference current against the measured current from the grid.

In the case of a grid fault, the current measured from the grid is nearly zero. In contrast, in this fault case, the current at the PMSG terminal is nearly the maximum current. Thus, the new control input of the MSC control is injected during the grid fault to avoid the current comparison, as shown in Figure 5.9.

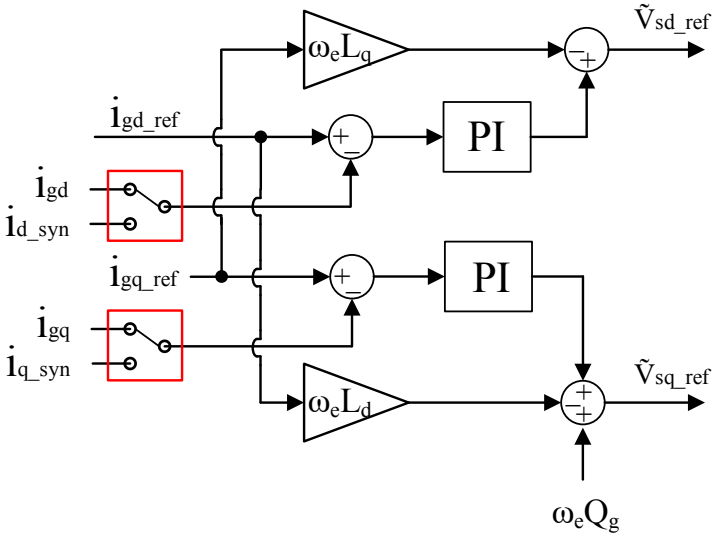

Figure 5.9: New control input, i_{dq_syn} during the grid fault.

5.4 Phase-Locked Loop (PLL)

The input voltage signal of PLL is also replaced with the synthesised signal, as shown in Figure 5.10. In particular, v_{g_syn} is the synthesised grid voltage. The input of the PLL, v_{g_abc} is switched when the CB on the grid side is tripped. More switching operations are discussed in the next section.

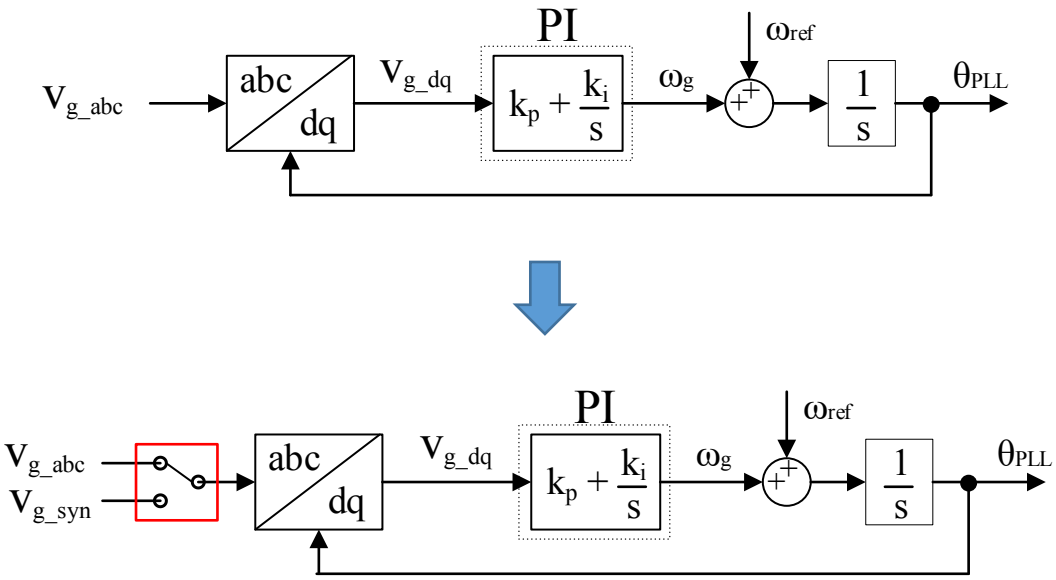

Figure 5.10: New PLL input signal, v_{dq_syn} during the grid fault.

5.5 Delay Estimation

The delay between the grid and PMSG voltage can be easily identified in the offline simulation. As seen in Figure 5.3, the delay is roughly about 4ms. However, each system has different values for the delay. Therefore, cross-correlation is used to estimate an accurate phase angle delay, and a Kalman Filter is used for tracking the actual grid voltage during the steady-state for any WT system.

The grid voltage and PMSG voltage frequencies are very stable during the steady-state condition. This condition makes it relatively straightforward to generate the synthetic grid voltage waveform with the PMSG terminal voltage, assuming the delay between the grid and PMSG voltages is nearly fixed. The estimated phase angle is used to generate a synthetic signal as the control input for both VSI and PMSG.

In many practical applications of filtering theory, the delay is mostly identified as a problem because it is not only difficult to estimate but also it irregularly changes with system dynamics. However, in this case, the phase angle delay, τ, shown in Figure 5.11, between the grid and PMSG voltages during the steady-state condition is the identification needed to generate a synthetic sinusoidal waveform to replace the grid voltage as the control input during the fault. The phase angle delay in time is also sensitive to any frequency change in the voltage, which can help identifying any system frequency issues. In the delay estimation shown in Figure 5.11, the PMSG voltage model is represented by a discrete equation for computation.

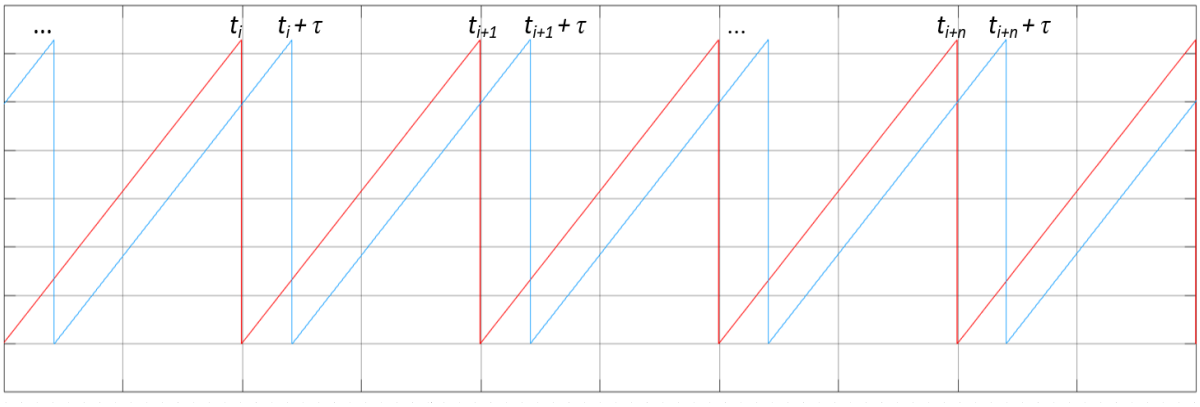

Figure 5.11: Measurement sequence of phase angle delay.

i. Cross-correlation

The voltage vector of the grid is modelled:

$$\boldsymbol{x_1}(t) = \boldsymbol{v_{g_{abc}}}(t) + \boldsymbol{n_1}(t) \tag{5.5}$$

where $\boldsymbol{v_{g\_abc}}(t)$ is the grid voltage, and $\boldsymbol{n_1}(t)$ is white Gaussian noise by the grid. The PMSG terminal voltage model is expressed:

$$\boldsymbol{x_2}(t) = \boldsymbol{v_{pmsg_{abc}}}(t - \tau) + \boldsymbol{n_2}(t) \tag{5.6}$$

where $\boldsymbol{v_{pmsg\_abc}}(t)$ is the terminal voltage of PMSG, $\boldsymbol{n_2}(i)$ is white Gaussian noise. The synthesised waveform as a new control input is processed as shown in Figures 5.12 and 5.13.

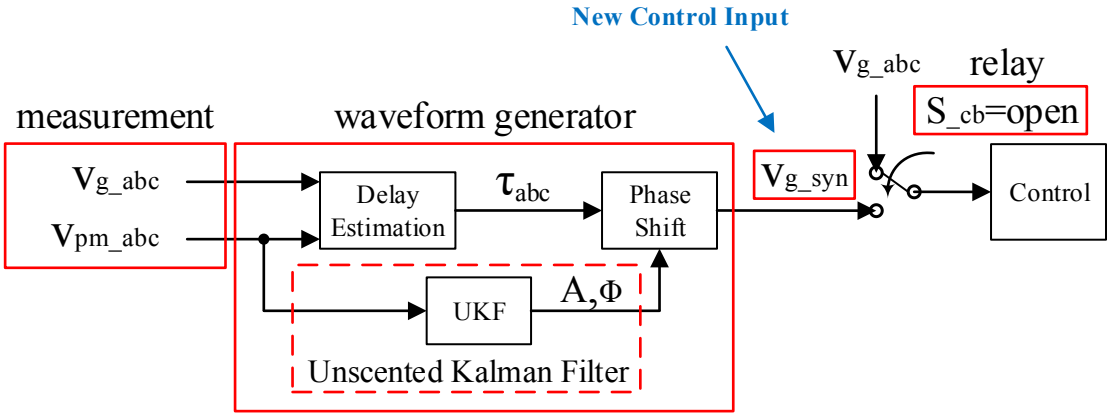

Figure 5.12: Synthesised control input in cross-correlation.

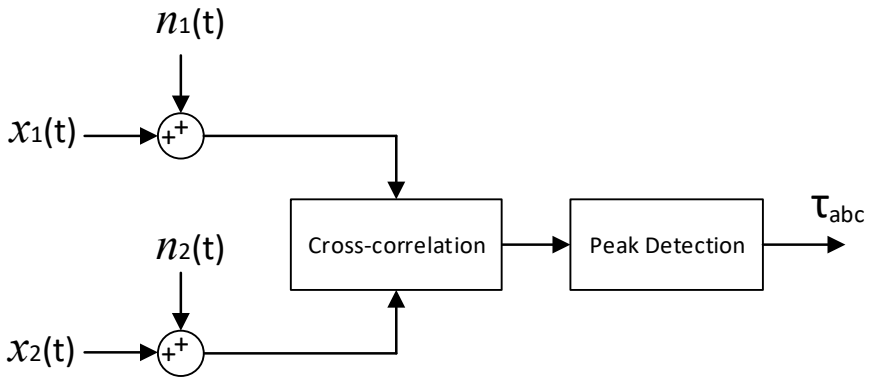

Figure 5.13: Delay estimation using cross-correlation and peak detection.

The cross-correlation [178] between the grid and PMSG voltage vectors provides the information on how much time delay exhibits between the PMSG voltage signal compared to the grid voltage signal. The cross-correlation between the grid and PMSG voltages, $\boldsymbol{x_1}(t)$ and $\boldsymbol{x_2}(t)$ is defined:

$$w(t) = \boldsymbol{x_1}(t) \otimes \boldsymbol{x_2}(t) \tag{5.7}$$

$$\triangleq \int_{-\frac{T}{2}}^{\frac{T}{2}} \boldsymbol{x_1}^*(\tau)\boldsymbol{x_2}(\tau + t)d\tau$$

$$= \int_{-T/2}^{T/2} \boldsymbol{x_1}^*(\tau - t)\boldsymbol{x_2}(\tau)d\tau \tag{5.8}$$

The complex conjugate $\boldsymbol{x_1}^*(\tau)$ in Equation (5.8) does not make any difference in the result because only the real value from the simulation is used.

In discrete form, Equation (5.8) for a time-sample lag of *m* is defined:

$$\boldsymbol{x_1}(m) \otimes \boldsymbol{x_2}(m) = \frac{1}{n}\sum_{k=0}^{k-1} x_1[k]\, x_2[k+m] \tag{5.9}$$

As shown in Figure 5.14, the PMSG signal lags about 2224 samples behind the grid voltage signal at the measurement point, which translates into 4.448ms lag at the sampling rate of 500 kHz. This cross-correlation function gives more accurate estimates than the visually estimated value from Figure 5.3.

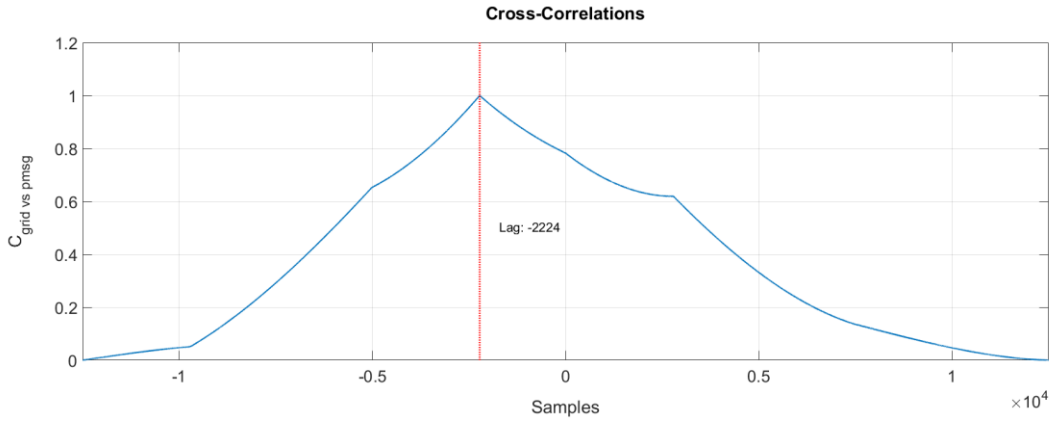

Figure 5.14: Cross-correlation between the grid and PMSG voltages (half-cycle window).

ii. Unscented Kalman Filter

The extended Kalman filter (EKF) requires Jacobian matrices to linearise the nonlinear function causing the underlying nonlinear model propagating the covariance [180]. Instead, the unscented Kalman filter (UKF) uses a deterministic sampling approach to estimate the mean and covariance matrices with a minimal set of sample points [181]. Thus, an UKF is used to generate a smoother waveform, which is nonlinear in the time-domain, from the noisy generator terminal voltage. Adding an UKF gives a few benefits, notably accuracy and adaptive frequency filterting, even if there is slight change or the fundamental frequency may be other than 50 Hz. However, adding an UKF makes the system more complex. The effect of UKF is examined later in this chapter.

The voltage signal model is expressed by using simple a UKF model [179]:

$$\boldsymbol{x}(i+1) = \boldsymbol{f}\big(\boldsymbol{x}(i), \boldsymbol{u}(i)\big) + \boldsymbol{w}(i) \tag{5.10}$$

where $\boldsymbol{x}(i)$ is the state at the time-step, i, $\boldsymbol{u}(i)$ is the control input, and $\boldsymbol{w}(i)$ is an additive white Gaussian noise by the PMSG, which is represented by covariance matrix $\boldsymbol{Q}(i)$. The function $\boldsymbol{f}(\cdot)$ is the relation function between variables between i^{th} and $i+1$ steps.

The voltage measurement equation is expressed:

$$\boldsymbol{z}(i) = \boldsymbol{H}\big(x(i)\big) + \boldsymbol{w}_m(i) \tag{5.11}$$

where $\boldsymbol{z}(i)$ is the measured voltage value, $\boldsymbol{w}_m(i)$ is an additive white Gaussian noise with covariance matrix $\boldsymbol{Q_m}(i)$, and $\boldsymbol{H}(\cdot)$ is the relation function between the state and the measured voltage value.

To apply Equation (5.11), the amplitude and frequency of the sinusoidal waveform are defined [180]:

$$x = Asin(\omega t) \tag{5.12}$$

$$\dot{x} = A\omega cos(\omega t) \tag{5.13}$$

$$\ddot{x} = -A\omega^2 sin(\omega t) \tag{5.14}$$

for given noisy phase-A voltage of PMSG.

Substituting x into $\ddot{x}$ yields:

$$\ddot{x} = -\omega^2 x \tag{5.15}$$

where $\dot{\omega} = u$.

The state matrix is thus defined:

$$\begin{bmatrix} \dot{x} \\ \ddot{x} \\ \dot{\omega} \end{bmatrix} = \begin{bmatrix} 0 & 1 & 0 \\ -\omega^2 & 0 & 0 \\ 0 & 0 & 0 \end{bmatrix} \begin{bmatrix} x \\ \dot{x} \\ \omega \end{bmatrix} + \begin{bmatrix} 0 \\ 0 \\ u \end{bmatrix} \tag{5.16}$$

Since x is a vector, it must be computed as an equation of discrete numerical values from the measurement.

$$\boldsymbol{f}(\cdot) = \frac{\partial f(\boldsymbol{x})}{\partial \boldsymbol{x}}$$

$$= \begin{bmatrix} \frac{\partial \dot{x}}{\partial x} & \frac{\partial \dot{x}}{\partial \dot{x}} & \frac{\partial \dot{x}}{\partial \omega} \\ \frac{\partial \ddot{x}}{\partial x} & \frac{\partial \ddot{x}}{\partial \dot{x}} & \frac{\partial \ddot{x}}{\partial \omega} \\ \frac{\partial \dot{\omega}}{\partial x} & \frac{\partial \dot{\omega}}{\partial \dot{x}} & \frac{\partial \dot{\omega}}{\partial \omega} \end{bmatrix}$$

$$= \begin{bmatrix} 0 & 1 & 0 \\ -\tilde{\omega}^2 & 0 & -2\tilde{\omega}\tilde{x} \\ 0 & 0 & 0 \end{bmatrix} \tag{5.17}$$

To find the fundamental matrix with two terms:

$$\boldsymbol{\Phi}(t) = I + \boldsymbol{f}(\cdot)t = \begin{bmatrix} 1 & t & 0 \\ -\tilde{\omega}^2 t & 1 & -2\tilde{\omega}\tilde{x}t \\ 0 & 0 & 1 \end{bmatrix} \tag{5.18}$$

Converting the continuous $\boldsymbol{\Phi}(t)$ to a discrete form yields:

$$\boldsymbol{\Phi}_i = \begin{bmatrix} 1 & 1 & 0 \\ -\tilde{\omega}_{i+1}^2 T_s & 1 & -2\tilde{\omega}_{i+1}\tilde{x}_{i+1}T_s \\ 0 & 0 & 1 \end{bmatrix}, \qquad i = 0, 1, 2, \dots, n \tag{5.18}$$

where T_s is the sampling time array.

The process noise represented by covariance matrix, Q, is defined:

$$Q = \begin{bmatrix} 0 & 0 & 0 \\ 0 & 0 & 0 \\ 0 & 0 & \lambda \end{bmatrix} \tag{5.19}$$

The discrete form of Q_i is defined:

$$\boldsymbol{Q_i} = \int_0^{T_s} \boldsymbol{\Phi(\tau) Q \Phi^T(\tau) dt} \tag{5.20}$$

Substituting Q, Φ and τ yields:

$$\boldsymbol{Q_i} = \int_{\boldsymbol{0}}^{\boldsymbol{T_s}} \begin{bmatrix} 1 & 1 & 0 \\ -\tilde{\omega}^2\tau & 1 & -2\tilde{\omega}\tilde{x}\tau \\ 0 & 0 & 1 \end{bmatrix} \begin{bmatrix} 0 & 0 & 0 \\ 0 & 0 & 0 \\ 0 & 0 & \lambda \end{bmatrix} \begin{bmatrix} 1 & -\tilde{\omega}^2\tau & 0 \\ \tau & 1 & 0 \\ 0 & -2\tilde{\omega}\tilde{x}\tau & 1 \end{bmatrix} d\tau, \quad i = 0, 1, 2, \dots, n$$

$$= \int_{\boldsymbol{0}}^{\boldsymbol{T_s}} \begin{bmatrix} 0 & 0 & 0 \\ 0 & 4\tilde{\omega}^2\tilde{x}^2\tau^2\boldsymbol{\Phi} & -2\tilde{\omega}\tilde{x}\tau\boldsymbol{\Phi} \\ 0 & -2\tilde{\omega}\tilde{x}\tau\boldsymbol{\Phi} & \boldsymbol{\Phi} \end{bmatrix} d\tau$$

$$= \begin{bmatrix} 0 & 0 & 0 \\ 0 & \frac{4}{3}\tilde{\omega}^2\tilde{x}^2 T_s^3\boldsymbol{\Phi} & -\tilde{\omega}\tilde{x}T_s^2\boldsymbol{\Phi} \\ 0 & -\tilde{\omega}\tilde{x}T_s^2\boldsymbol{\Phi} & T_s\boldsymbol{\Phi} \end{bmatrix} \tag{5.20}$$

The voltage measurement vector is defined:

$$\boldsymbol{x_i^*} = \underbrace{[1 \quad 0 \quad 0]}_{\boldsymbol{H}} \begin{bmatrix} x \\ \dot{x} \\ \omega \end{bmatrix} + \boldsymbol{w}_m \tag{5.21}$$

where $\boldsymbol{w}_m$ is represented as a covariance matrix $\boldsymbol{Q}_m = \boldsymbol{\sigma}_i^2$.

The complete UKF equation is defined:

$$\tilde{x}_i = \vec{x}_i + K1_i(x_i^* - \vec{x}_i) \tag{5.22}$$

$$\tilde{\dot{x}}_i = \vec{\dot{x}}_i + K2_i(x_i^* - \vec{x}_i) \tag{5.23}$$

$$\tilde{\omega}_i = \vec{x}_{i-1} + K3_i(x_i^* - \vec{x}_i) \tag{5.24}$$

where $\vec{x}_i$ is the numerically integrated value, which is not the same as the calculated values from the fundamental matrix $\boldsymbol{A}$ in Equations (5.12) – (5.14).

UKF Simulation result:

The result of estimating the PMSG voltage signal using UKF is shown in Figure 5.15.

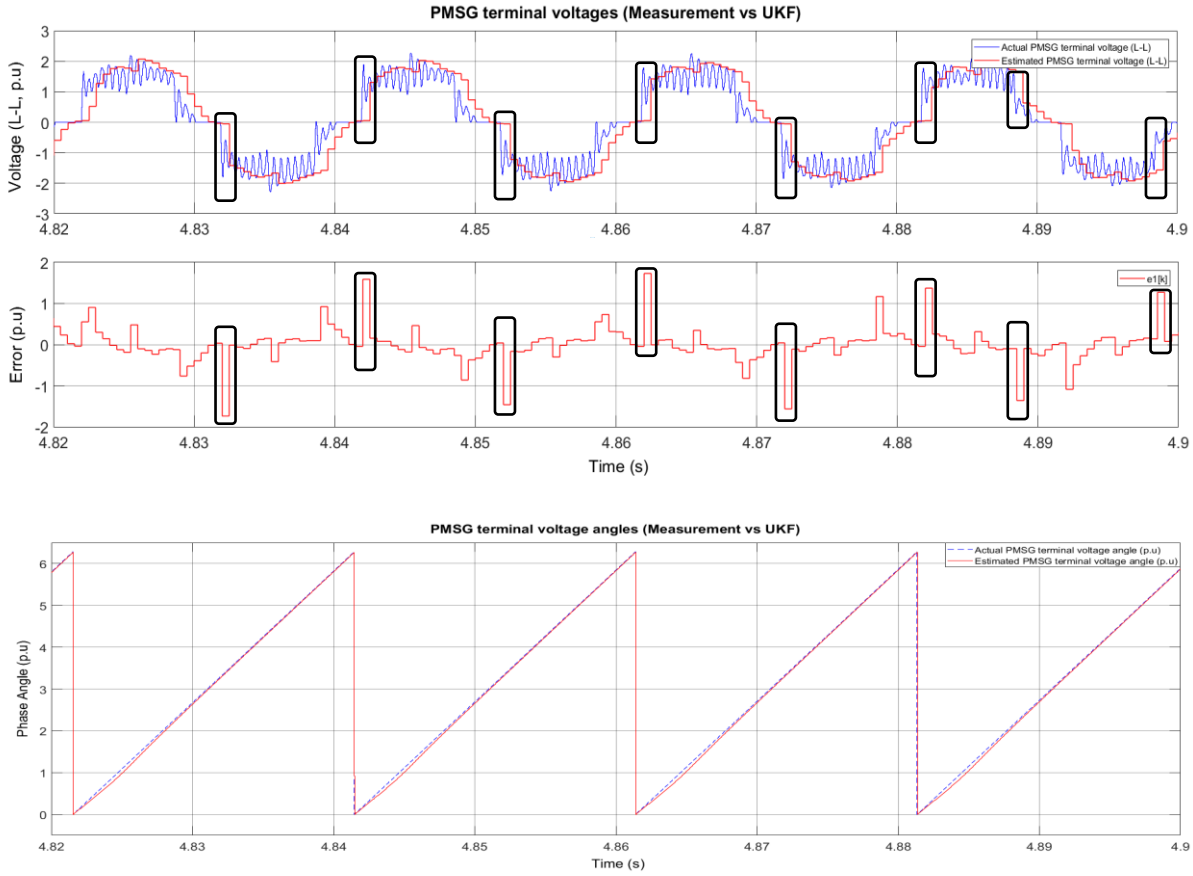

Figure 5.15: Estimated PMSG terminal voltage (top) and phase angle (bottom) using UKF.

The error values near zero-crossing are mainly due to the stiff change in the magnitude of the voltage combined with computation delays. However, this error is due to the latency of estimation combined with the presence of noise in the PMSG voltage. The actual voltage value is the raw data used in this simulation. The sampling rate of the UKF is 10 times slower than the measurement frequency in this simulation.

5.6 Initial Proof of Control Concept Using Case Studies

Three-phase grid fault simulations that create post-fault oscillation are conducted to verify and validate the control performance. A total of six cases with different system configurations are simulated, as shown in Table 5.2. For Cases 1 to 4, the WT system model developed from this thesis work has been used. For Cases 5 and 6, another WT system used to validate the general applicability of the control strategy.

The WT system used in Cases 5 and 6, has a different power rating of DFIG-based WT with a controlled converter on the generator side instead of the rectifier. The specification of this system is well documented in [190]. For the MSC converter control, the control method shown in Figure 5.9 is implemented. With the estimated voltage, the input current signal i_{dq_syn} is calculated for MSC control input. The calculation of i_{dq_syn} is shown in Appendix III.

Table 5.2 GRID FAULT SIMULATION SETUP.

	Case 1	**Case 2**	**Case 3**	**Case 4**	**Case 5**	**Case 6**
WT type	PMSG	PMSG	PMSG	PMSG	DFIG	DFIG
Rated power	2.0 MW	2.0 MW	2.0 MW	2.0 MW	1.5 MW	1.5 MW
Grid freuquency	50 Hz	50 Hz	50 Hz	50 Hz	60 Hz	60 Hz
New Control input	**No**	**No**	**Yes**	**Yes**	**No**	**Yes**
Fault starting time	5.0 s	5.0 s	5.0 s	5.0 s	6.0 s	6.0 s
Fault duration	0.4 s	0.4 s	0.4 s	0.5 s	0.5 s	0.5 s
CB actuation delay	5 ms	5 ms	5 ms	5 ms	5 ms	5 ms
Input switching delay	2 ms	2 ms	2 ms	2 ms	2 ms	2 ms
Crowbar protection	Yes	No	Yes	Yes	Yes	Yes
UKF Estimation	**No**	**No**	**Yes**	**Yes**	**No**	**Yes**
Oscillation	**Yes**	**No**	**No**	**No**	**Yes**	**No**

Figures 5.16 to 5.32 show the result of the simulations.

Case 1: Simulation result of the same system in Chapter 4. The oscillation observed in this system is the reference to Case 2 to 6.

Case 2: New control strategy with PMSG measurement data without UKF estimation is applied to Case 1. Also, the crowbar protection is not used.

Case 3: New control strategy with the synthesised control signal from UKF estimation is applied to Case 1. Also, the crowbar protection is applied to the DC-link.

Case 4: The fault duration is extended to 500ms to Case 4.

Case 5: A three-phase grid fault is applied to another WT system with a doubly-fed induction generator (DFIG). Different oscillation behaviour than Case 1 is observed.

Case 6: Case 5 with crowbar protection is applied.

Case 1 result:

System oscillations are observed from the EM torque of the PMSG, voltages and currents during the post-fault transient period, as shown in Figures 5.16 and 5.17. The undamped oscillation continues. Unlike TO, there is no oscillation growing in the speed of the PMSG. In addition, the DC-link voltage keeps rising. Also, the EM torque of the PMSG increases as the speed decreases.

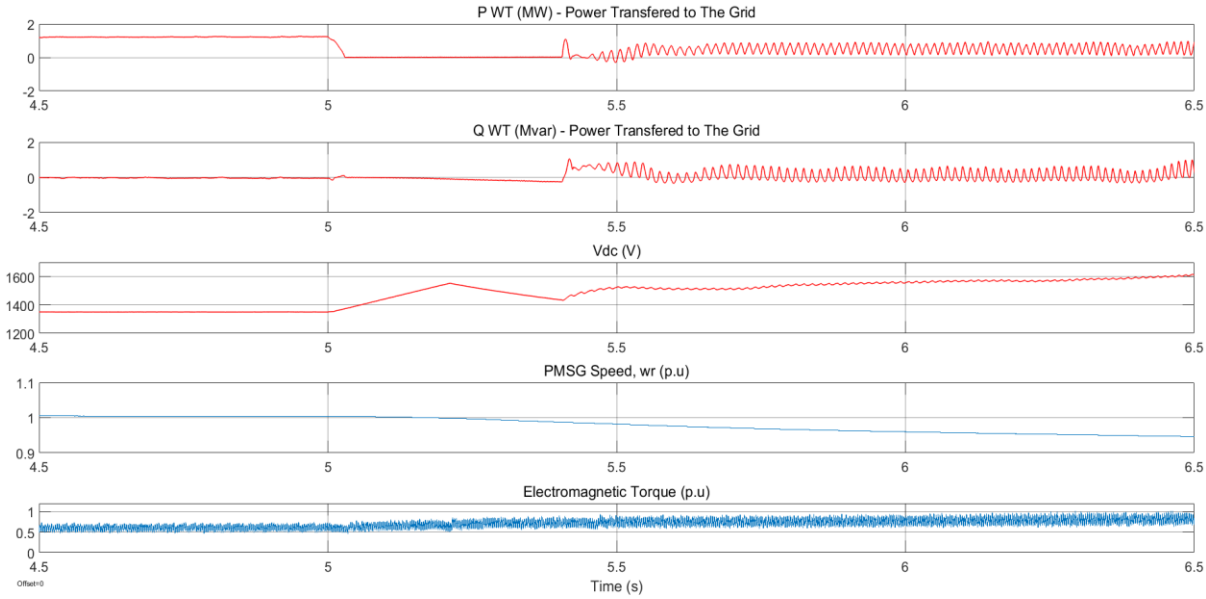

Figure 5.16: PQ transferred to the grid, Vdc, PMSG rotor speed and EM torque of PMSG.

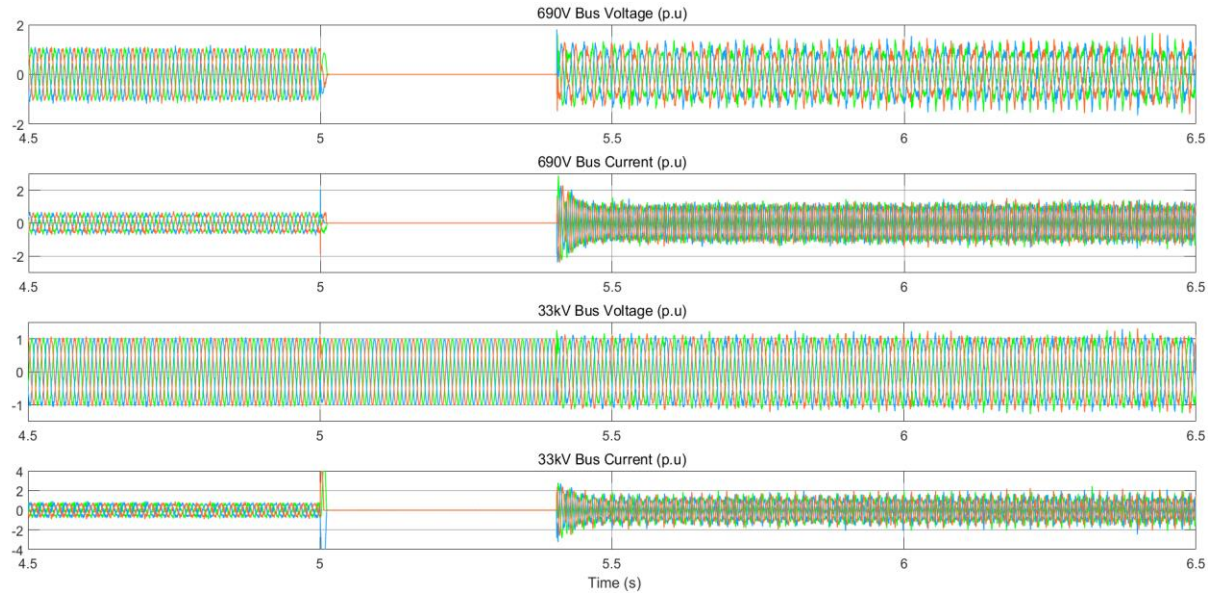

Figure 5.17: Bus V-I at the RL filter (VSI terminal) and 33kV.

Case 2 result:

The performance of the control strategy is evaluated with the length of the period that takes to recover from the transient condition to a stable operating state once the fault is cleared at 5.4 s, as shown in Table 5.3. Oscillations in the voltage and current are mitigated with the new control strategy, as shown in Figures 5.18 and 5.19. Due to the absence of crowbar protection, DC-link voltage keeps rising until the fault is cleared. In addition, the speed of the PMSG remains at the rated speed.

Table 5.3: CASE 2 - POST-FAULT TRANSIENT PERIOD BEFORE RECOVERING TO THE STEADY-STATE CONDITION.

Location	Measurement	Post-fault Transient Period (ms)
Bus 690V	690V Voltage	350
	Current	830
DC-link	Voltage	760

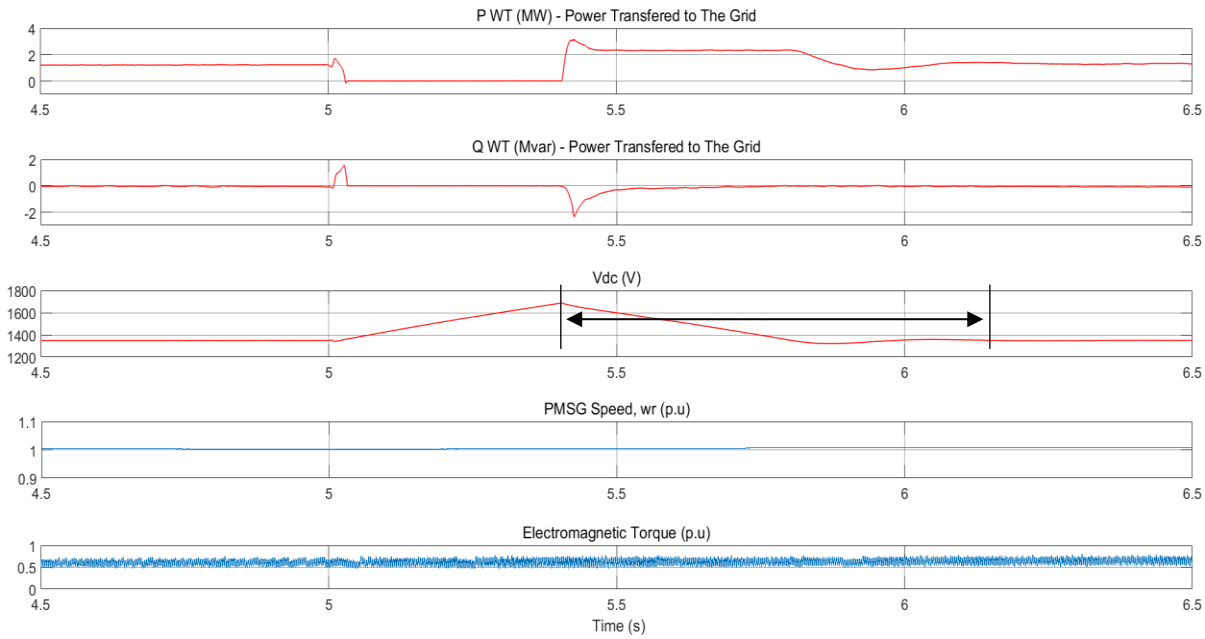

Figure 5.18: PQ transferred to the grid, Vdc, PMSG rotor speed and EM torque of PMSG.

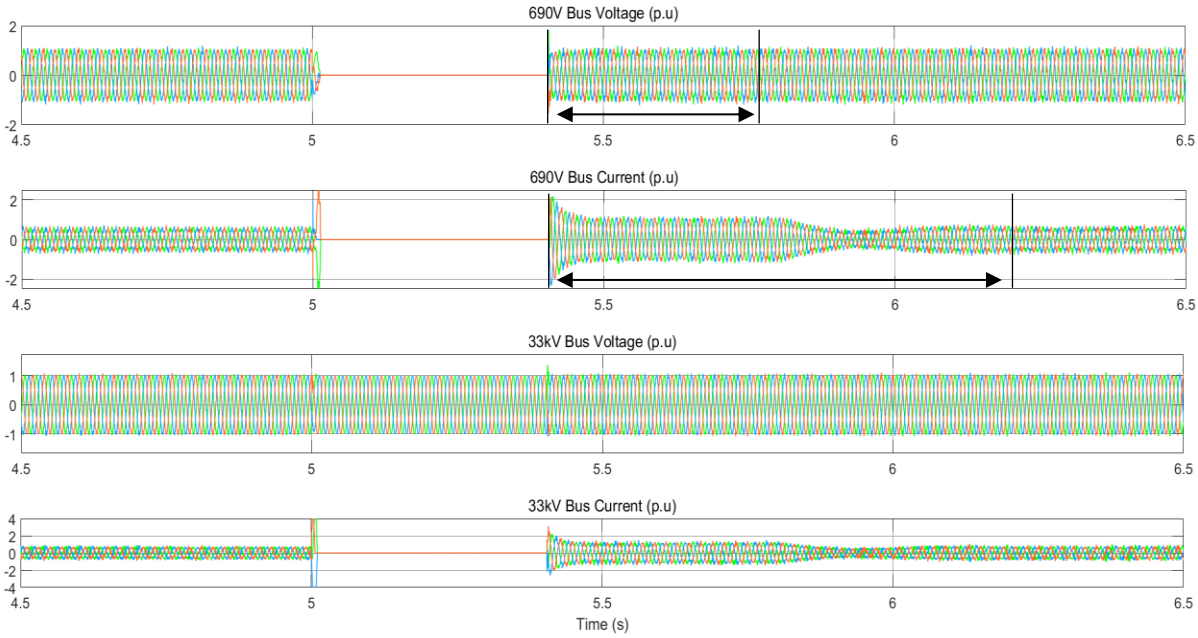

Figure 5.19: 690V bus V-I at LC filter and 33kV bus V-I.

Case 3 result:

The performance of the control strategy significantly improved from Case 2, as shown in Table 5.4. Since the current transient depends on the DC-link voltage, as shown in Figure 5.9 and Appendix III, the control input signal, i_{dq_syn}, is calculated from the measured DC-link voltage and becomes the input to the PMSG control. Therefore, the current transient is the response to the control input, i_{dq_syn}.

The PMSG keeps operating at nearly steady-state, as if it is not affected by the grid fault. The DC-link voltage recovers much quicker than in Case 2. The post-fault transient period shows almost 20% improvement with less damping in the current, as shown in Figures 5.20 and 5.21.

Table 5.4: CASE 3 - POST-FAULT TRANSIENT PERIOD BEFORE RECOVERING TO THE STEADY-STATE CONDITION.

Location	Measurement	Post-fault Transient Period (ms)
Bus 690V	690V Voltage	150
	Current	600
DC-link	Voltage	550

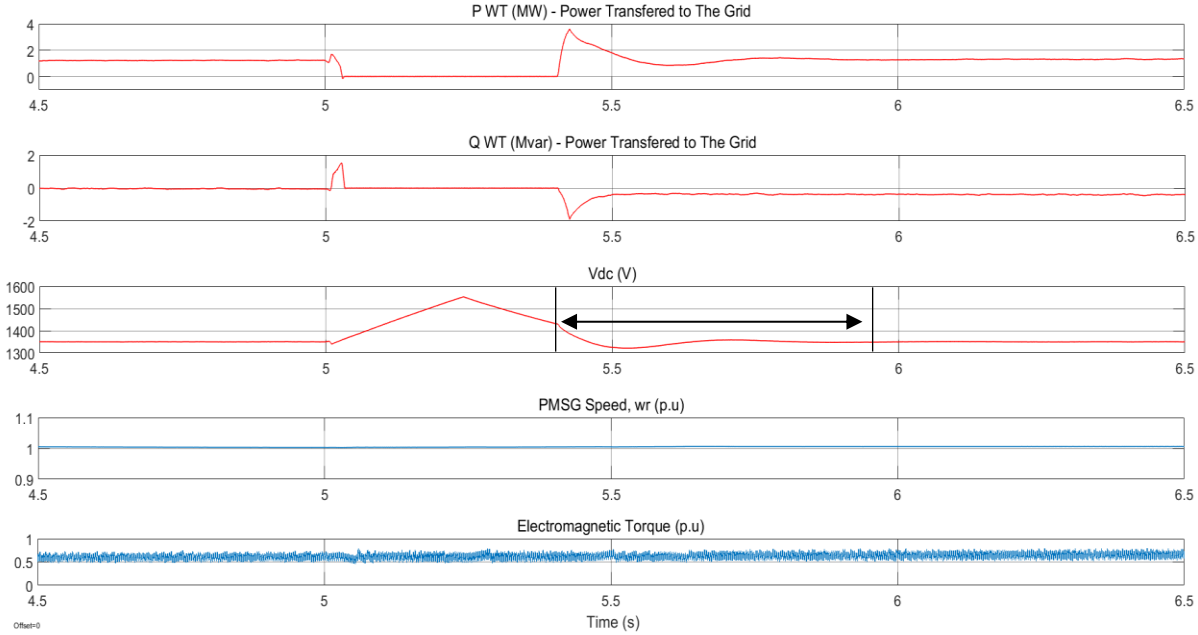

Figure 5.20: PQ transferred to the grid, Vdc, PMSG rotor speed and EM torque of PMSG.

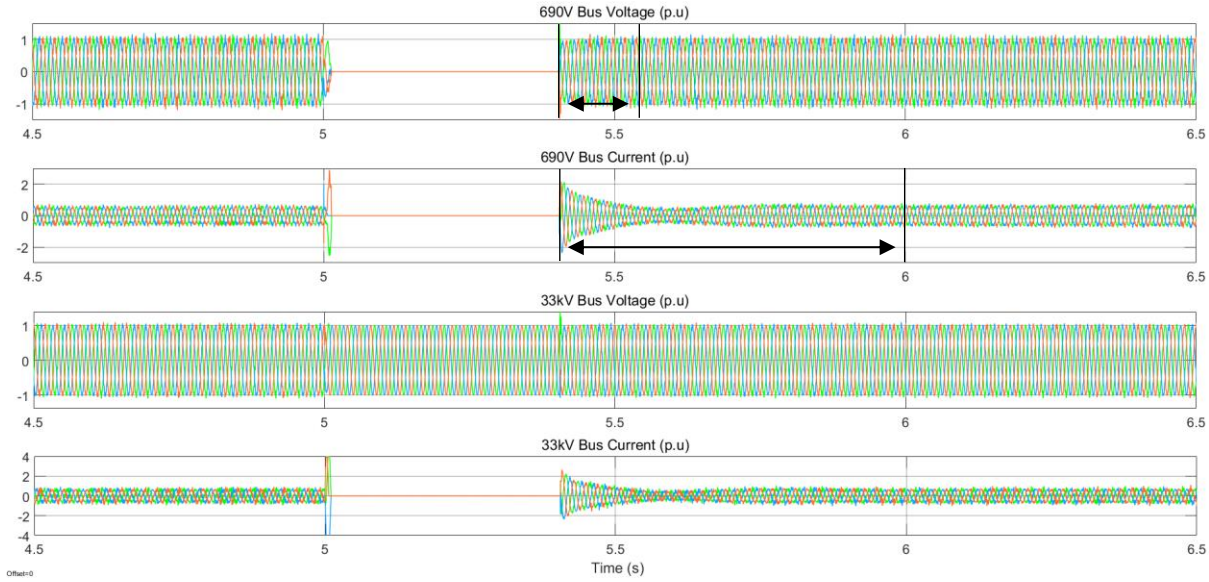

Figure 5.21: 690V bus V-I at LC filter and 33kV bus V-I.

Case 4 result:

Case 4 simulation results are shown in Figures 5.22 and 5.23, and show the control strategy can withstand an even longer three-phase grid fault by nearly 100 ms. It is a significant improvement over typical control methods, which uses faulted grid measurement values. The transient period and the system response are virtually identical to those shown in Case 3.

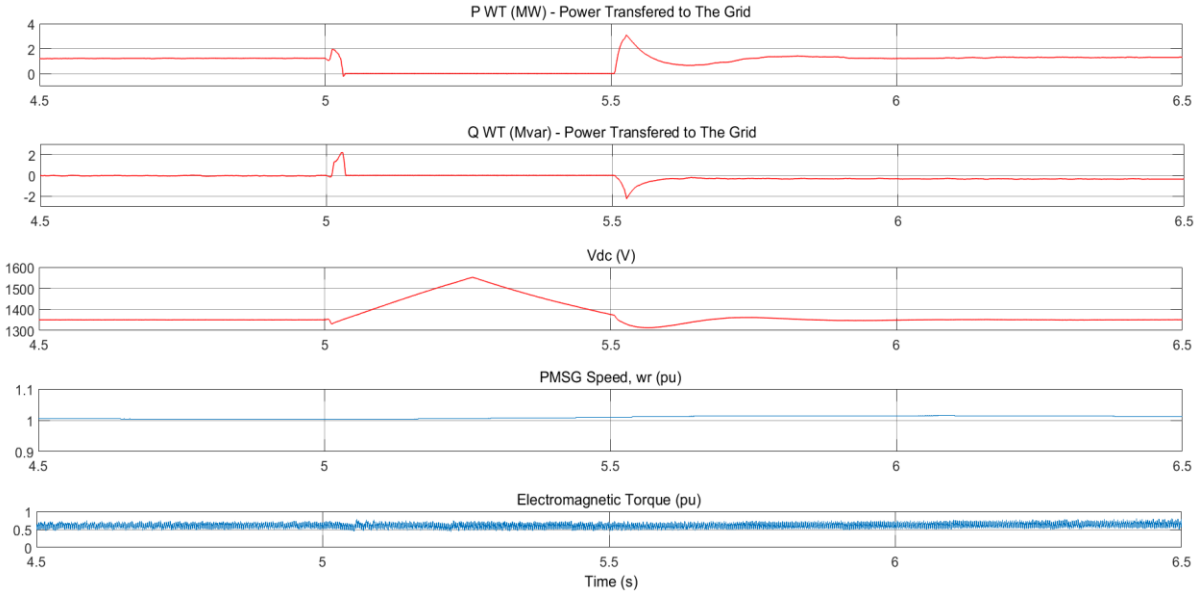

Figure 5.22: PQ transferred to the grid, Vdc, PMSG rotor speed and EM torque of PMSG.

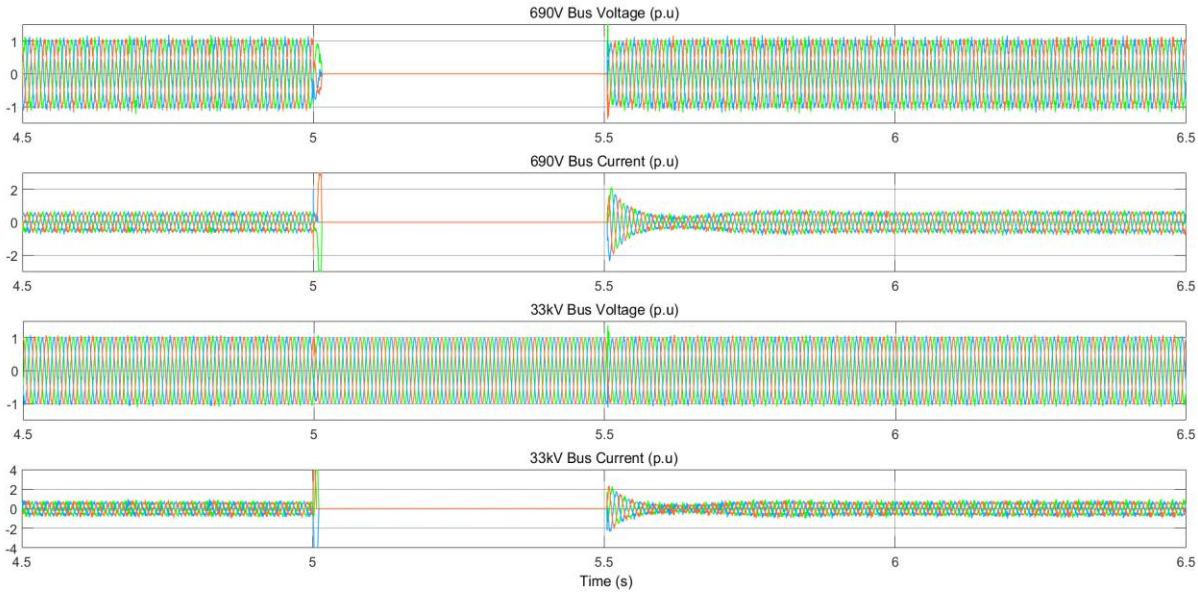

Figure 5.23: 690V bus V-I at LC filter and 33kV bus V-I.

Case 5 result:

This system shows very different oscillation characteristics than the system oscillation demonstrated in Case 1, as shown in Figures 5.24 to 5.27. The magnitude of oscillation is much larger on both voltage and current. Interestingly, the DC-link voltage initially oscillates with a high-frequency for 500 ms, then evolves with a much slower frequency afterwards.

The voltage waveform on the grid-side also exhibits nonlinear chaotic oscillation, as shown in Figure 5.24. The voltage oscillation on the grid-side in Case 1 is not as significant as Case 5. The doubly-fed induction generator (DFIG) is also affected, unlike Case 1. The EM torque and the speed fluctuate during the fault and post-fault periods.

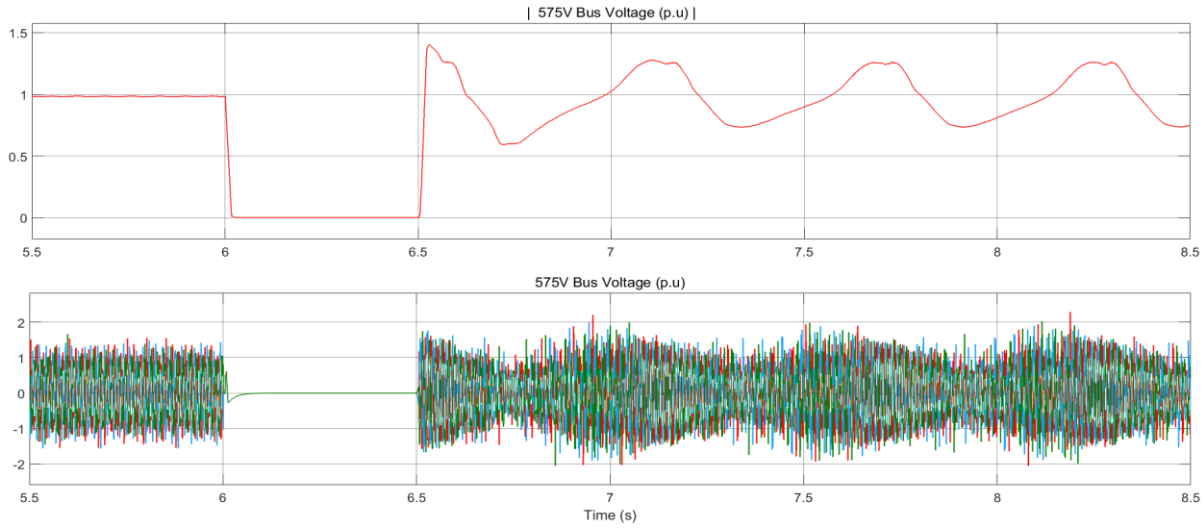

Figure 5.24: Voltage oscillation at LC filter terminal.

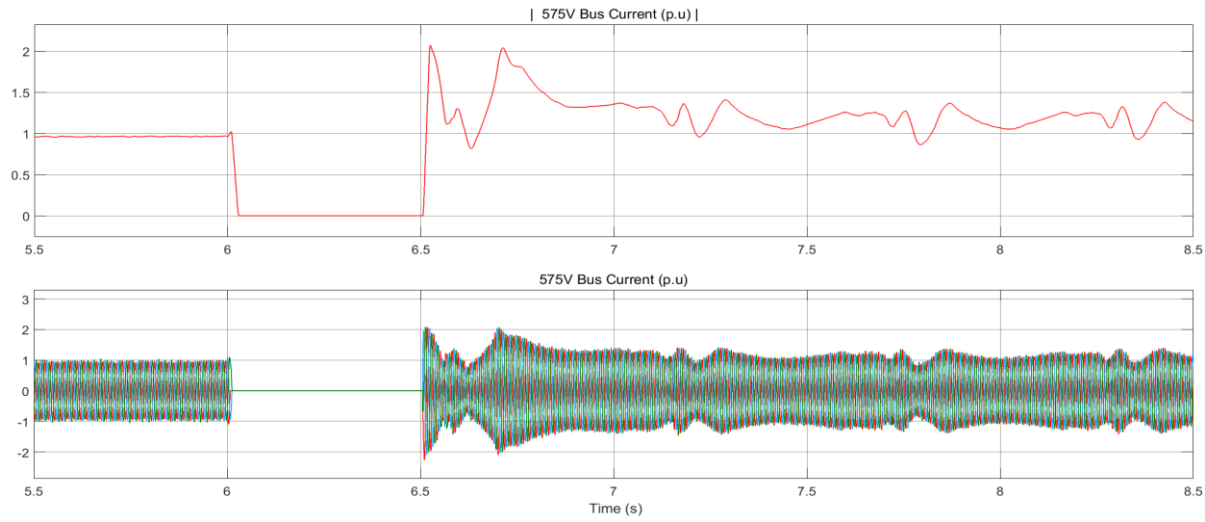

Figure 5.25: Current oscillation at LC filter terminal.

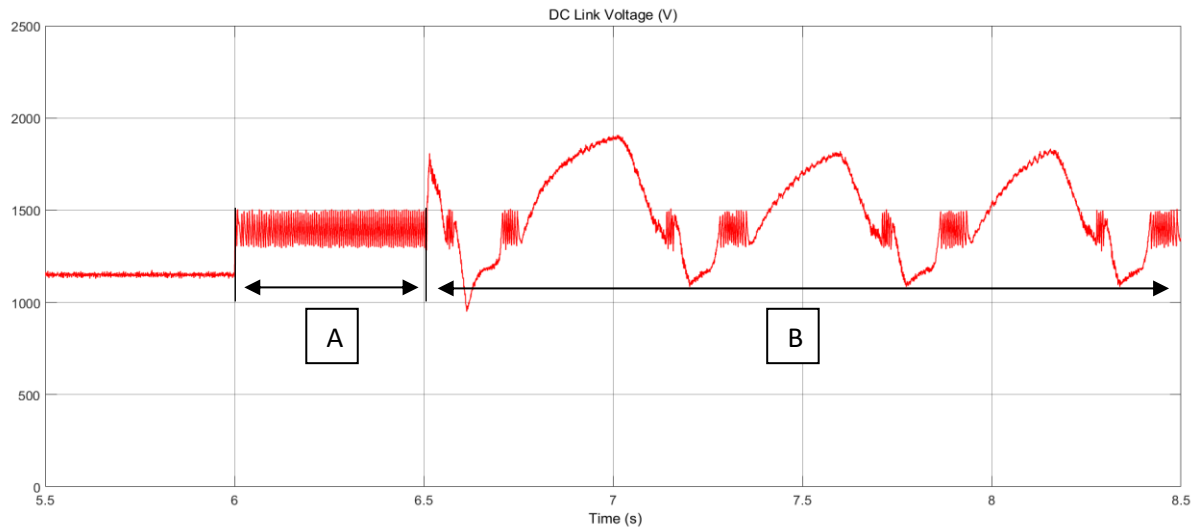

Figure 5.26: Chaotic oscillation in DC-link voltage.

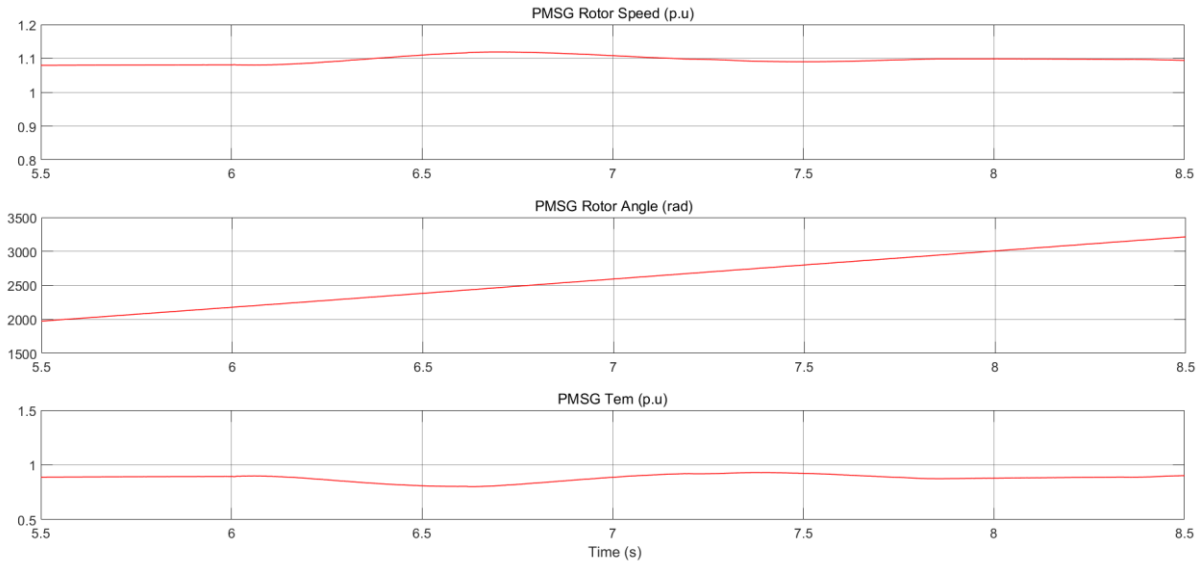

Figure 5.27: Behaviours of the DFIG during the post-fault transient.

A recent paper [191] addressed similar chaotic behaviour of a power system. However, the author does not mention how this behaviour occurs and states linear control is the cause of the chaotic oscillation. Since chaotic behaviour does not occur without applying an external force not considered in the system [192], this statement is questionable.

The WT system used in Case 5 by [190] addressed the voltage collapse due to the decrease of a DC-link voltage. In this simulation, the DC-link voltage has been oscillating between the stable and unstable regions simultaneously, as illustrated in Figure 5.28.

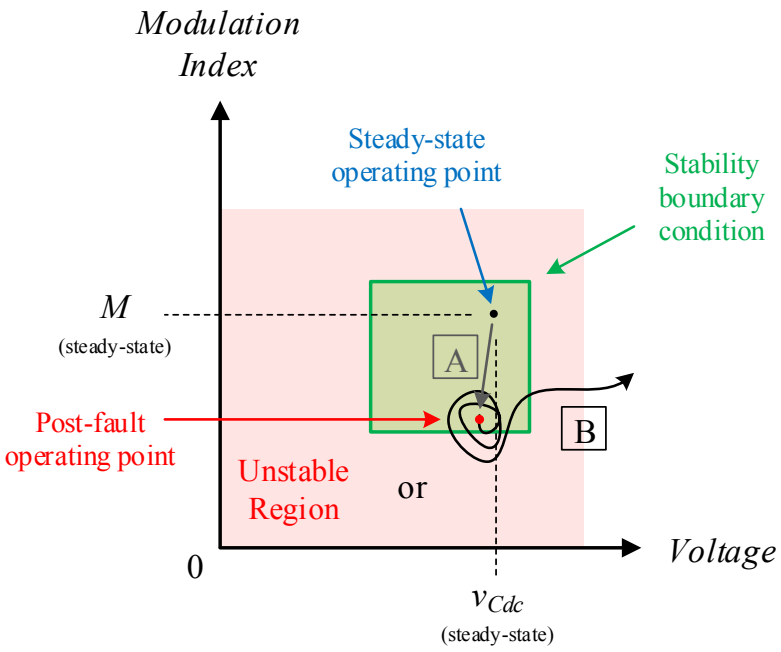

Figure 5.28: Illustration of chaotic oscillation in DC-link voltage.

Case 6 result:

This performance of the controller for Case 6 simulation is shown in Table 5.5. The chaotic oscillation behaviours are completely suppressed, as shown in Figures 5.29 to 5.32. Noticeably, the oscillating DC-link voltage during the fault period quickly recovers. In addition, it takes about 2.0 s for the DFIG stops fluctuating. The voltage waveform on the grid-side also exhibits nonlinear chaotic oscillation, as shown in Figure 5.24. The voltage oscillation on the grid-side in Case 1 is not as significant as in Case 5.

Table 5.5: CASE 6 - POST-FAULT TRANSIENT PERIOD BEFORE RECOVERING TO THE STEADY-STATE CONDITION.

Location	Measurement	Post-fault Transient Period (ms)
Bus 575V	Voltage	970
	Current	1000
DC-link	Voltage	400

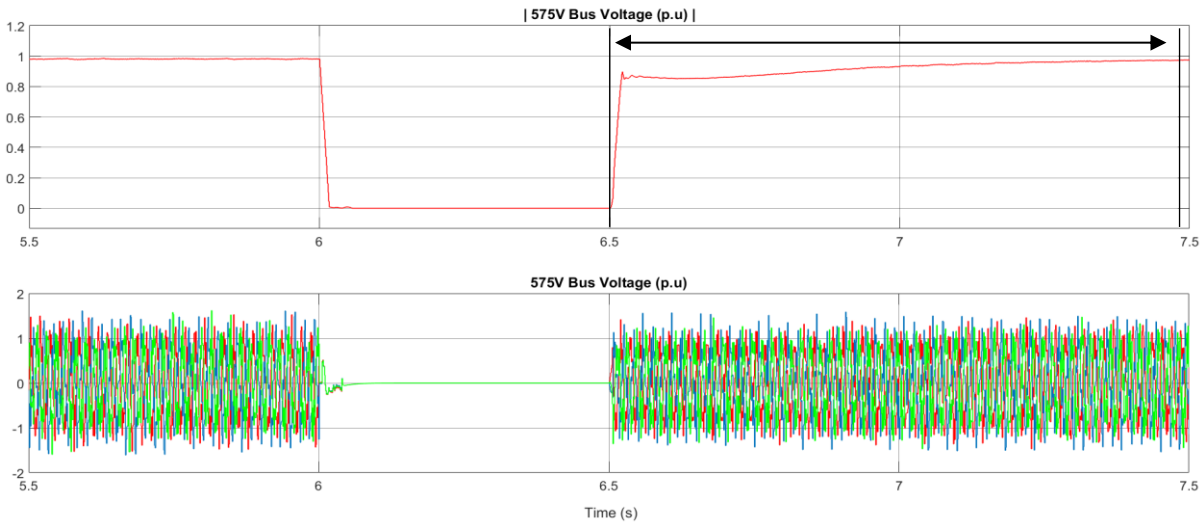

Figure 5.29: Voltage at LC filter terminal.

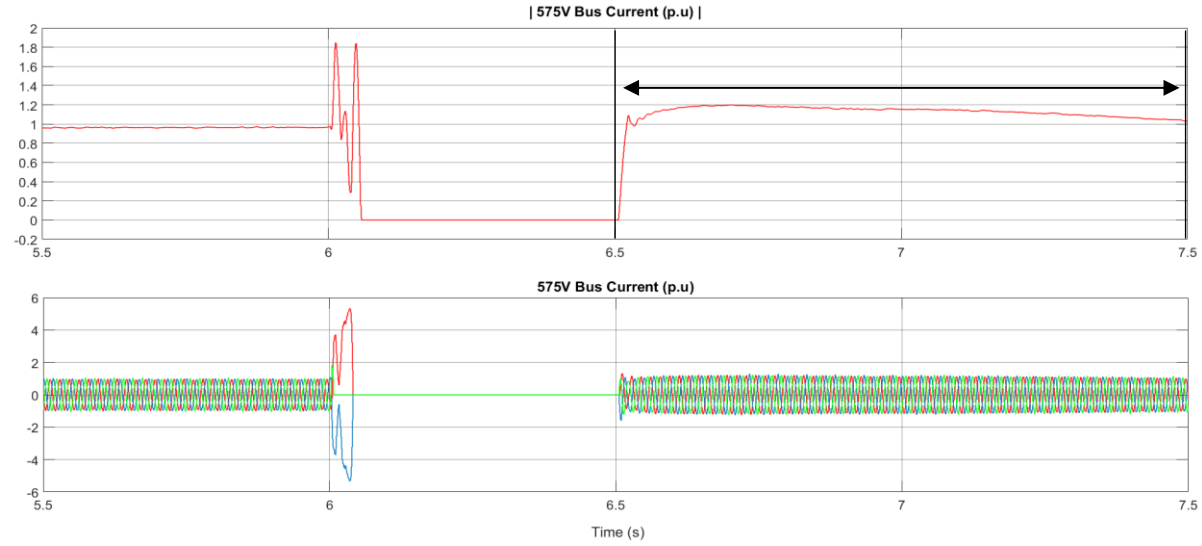

Figure 5.30: Current at LC filter terminal.

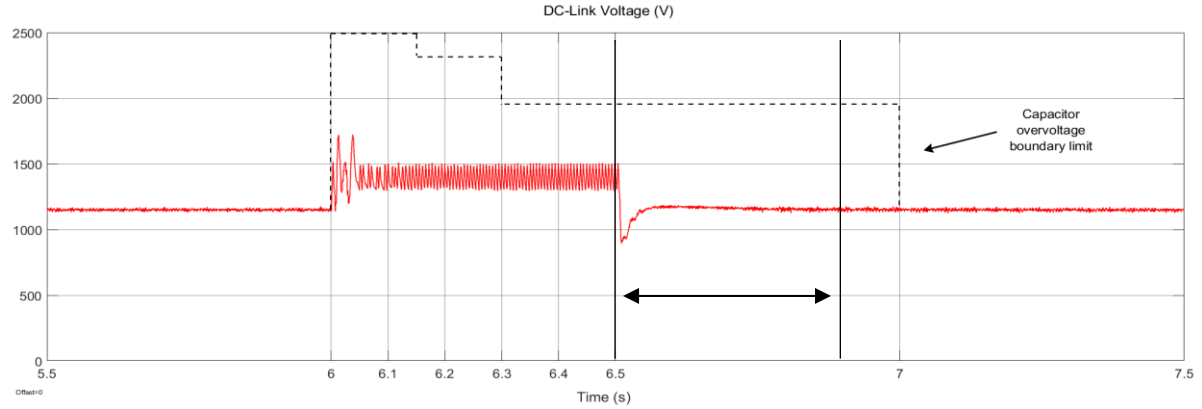

Figure 5.31: DC-link voltage and its overvoltage limit.

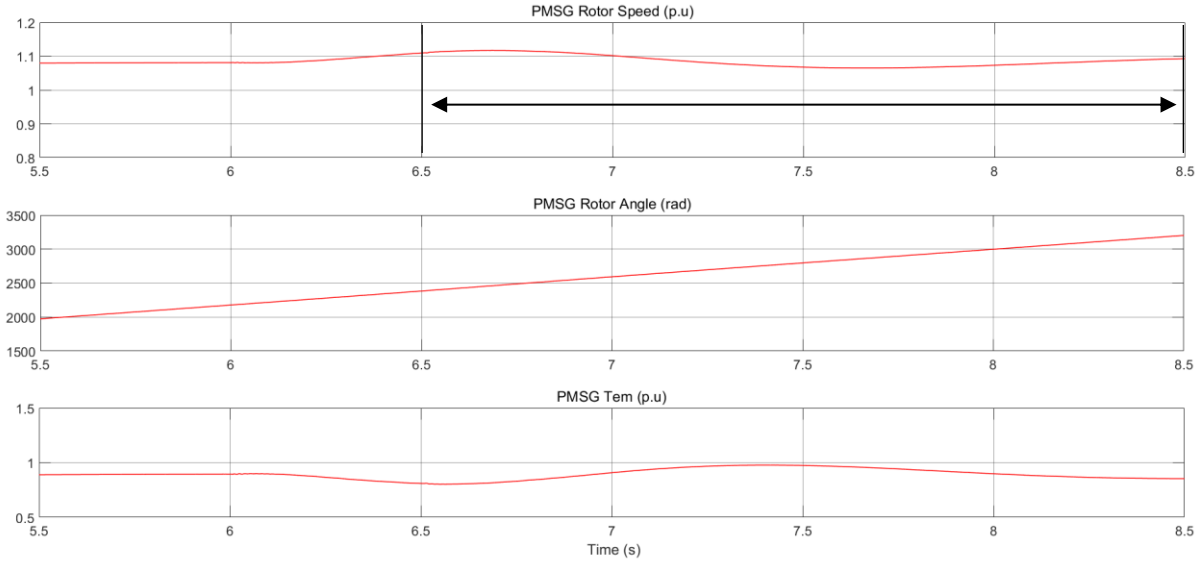

Figure 5.32: Behaviours of the DFIG during the post-fault transient.

5.7 Summary

The new transient control strategy with the synthesised input signal using UKF is applied to two different system models with oscillation instability via simulations in Cases 1 to 6.

The simulation results from Cases 1 to 6 show the post-fault oscillation is substantially mitigated without violating the maximum operation time and the permissible peak voltage of the DC-link capacitor, as shown in Table 5.1. In addition, the result of Case 4 shows the new control strategy can withstand an extended fault duration, and make the WT system recover back to the steady-state condition without any oscillating behaviour. The simulation results of Cases 3, 4 and 6 show the recovery time during the post-fault period is significantly quicker with crowbar protections to suppress overvoltage. In addition, the effect of switching transient due to the phase distortion was minimal.

In this chapter, the new control strategy with the synthesised control signal using UKF for VSI, MSC and PLL is presented. This control strategy proves its capability of mitigating the post-fault oscillation via two different PMSG-based WT simulation models. Based on the simulation result, the new control strategy designed in this chapter can be applied to any Type-4 wind turbine models, especially the WT system interconnected to weak grids.

Overall, the combination of cross-correlation and UKF methods is simple, but effective to mitigate the oscillation problem in grid fault cases. This control strategy can be possibly applied to any back-to-back converter controller as an auxiliary setup for weak grid-connected wind farm applications.

6
CONCLUSION

This chapter summarises the objective, contributions, and work presented in this research. Also, recommendations for future works are provided.

The work in this thesis contributes to the mechatronic modelling, validation, and control of a detailed model of the Type-4 WT system platform with potential system failure due to TO and SSCI.

Modelling of a full-scale Type-4 WT system with grid-interconnection is the first part of this thesis involving potential catastrophic failure and shut-down of the WT system because an accurate WT system model is the essential tool and foundation for analysis, design and control. The WT system model is validated through predominantly time-domain simulations rather than transfer-domain simulations. The simulation result provides an overview of the transient coupling through the system how it evolves.

For the TO problem, two different stiffness of the shaft shows mechanical torsion between the WT and PMSG. The stiffness of the shaft is coupled with the speed of the PMSG. To overcome the TO problem shown in this research, monitoring the rate of change in speed-torque of the shaft is proposed.

For the SSCI problem, it is shown that violation of the PBE based system model, and the control system of this system model with the input, which is measured data from the faulted grid.

Many control and filter design tasks are done in the frequency domain because the time-domain simulation is computationally intensive for large scale systems like wind farms. In cases, such as the post-fault oscillation phenomena shown in this research, proves that time-domain simulation is more effective and efficient to analyse the underlying cause of the oscillation. A new control strategy is proposed to mitigate the post-fault oscillation. The control input is synthesised using UKF to estimate the PMSG terminal voltage combined with a cross-correlation to estimate the time-sample delay.

Finally, the new control strategy is applied to two very different WT systems to validate its applicability. A full-scale WT system model in time-domain is developed with a two-port structure.

- A transient model of DC-link is developed using DC variables only.
- A new control strategy using synthetically generated control input signals of the grid voltage and current by applying a UKF and cross-correlation.
- The control strategy was validated via two different WT systems.

6.1. Future Work

The following subjects have been ongoing projects for implementing the new control strategy shown in this thesis.

6.1.1. Controller implementation

Since the computation delay is considered in the simulation model in this thesis, the implementation of this control strategy is practical in real-world applications. It requires small modifications to the control circuit board: a signal generator for the new control input signal and a switch instruction between the existing control input port and a new control input port.

6.1.2. Protective relay development

Computations used in this thesis can easily be implemented to protective relays with a small additional circuit for signal generation. Massive mathematical and computational research works cannot be implemented with available hardware due to complexities and computational delay. The control strategy used in this thesis is rather practical and implementation-ready.

REFERENCES

[1] CIGRE Committee 32, "Tentative classification and terminologies relating to stability problems of power systems," *Electra*, No. 56(8), 1978.

[2] Reder, M. D., E. Gonzalez, and J. J. Melero. "Wind Turbine Failures-Tackling current Problems in Failure Data Analysis." Journal of Physics: Conference Series. Vol. 753. No. 7. IOP Publishing, 2016.

[3] F. A. Aranda, "International Statistical Analysis on Wind Turbine Failures," Kassel, Germany, in *Annual Proceedings of the IEA Topical Expert Meeting*, pp. 117-122, 2011

[4] B. Chen, A. Shrestha, F. A. Ituzaro and N. Fischer, "Addressing protection challenges associated with Type 3 and Type 4 wind turbine generators," *in Proceedings of the 2015 68th Annual Conference for Protective Relay Engineers*, College Station, TX, 2015, pp. 335-344.

[5] M. E. Lunow, J. Holboell and M. Henriksen, "Faults in the collection grid of offshore wind farms," in *Proceedings of the 2008 Annual IEEE Student Paper Conference*, Aalborg, 2008, pp. 1-5.

[6] Sheng, Shuangwen. "Report on wind turbine subsystem reliability—A survey of various databases." *National Renewable Energy Laboratory*, Golden, CO, Tech. Rep. NREL/PR-5000-59111, 2013.

[7] P. Tavner, F. Spinato, G. J. W. van Bussel, and E. Koutoulakos, "Reliability of Different Wind Turbine Concepts with Relevance to Offshore Application," in *Proceedings of the European Wind Energy Conference*, March 31 – April 3, 2008, Brussels, Belgium.

[8] L. Pettersson, J. O. Andersson, C. Orbert, and S. Skagerman, *RAMS-Database for Wind Turbines – Pre-study*, Elforsk Report, 2010

[9] *Wind energy statistics in Finland*.
Available online: http://www.vtt.fi/proj/windenergystatistics/?lang=en.

[10] A. Stenberg and H. Holttinen, "Analysing Failure Statistics of Wind Turbines in Finland", in *Proceedings of the European Wind Energy Conference*, April 20-23, 2010, Warsaw, Poland.

[11] F. Carlsson, E. Eriksson, and M. Dahlberg, *Damage Preventing Measures for Wind Turbines – Phase 1 Reliability Data*, Elforsk Report, 2010.

[12] F. Iov, A. D. Hansen, P. Sørensen, and N. A. Cutululis, Mapping of grid faults and grid codes, Risø National Laboratory. (Denmark. Forskningscenter Risoe. Risoe-R; No. 1617(EN)).

[13] Z. Chen, "Issues of Connecting Wind Farms into Power Systems," in *Proceedings of The IEEE/PES Trans. and Distr. Conference & Exhibition*, 2005, Dalian, China

[14] A. D. Hansen, N. A. Cutululis, H. Markou, P.E. Sørensen, and F. Iov, *Grid fault and design-basis for wind turbines - Final report*, 2010
Roskilde: Danmarks Tekniske Universitet, Risø Nationallaboratoriet for Bæredygtig Energi. (Denmark. Forskningscenter Risoe. Risoe-R; No. 1714(EN)).

[15] Y. Sun, *Advances in Power and Energy Engineering,* in *Proceedings of the 8th Asia-Pacific Power and Energy Engineering Conference* in Suzhou, China, April 15-17, CRC PRESS, ISBN-13: 978-1138028463, pp 470-476, 2016

[16] O. S. Adio, X. Lin, J. Sun, F. Zhao and D. Yang, "Field studies for transient stability in continuous operation and contingency condition during 3−Φ short circuit at PCC for grid-connected 10MW Kastina wind farm," in *Proceedings of the 2013 IEEE PES Asia-Pacific Power and Energy Engineering Conference (APPEEC)*, Kowloon, 2013.

[17] G. Brauner, M. Heidl, D. Tiefgraber, M. Weniger and H. Haidvogl, "Voltage collapse phenomena in wind parks," *CIRED 2005* - in *Proceedings of the 18th International Conference and Exhibition on Electricity Distribution*, Turin*, Italy, 2005*

[18] G. D. Irwin, A. K. Jindal, A. L. Issacs, "Sub-synchronous control interaction between type 3 wind turbines and series compensated AC transmission systems", in *Proc. 2011 IEEE PES General Meeting*, pp. 1-6.

[19] A. A. Fouad, V. Vittal, "Power system response to a large disturbance: energy associated with separation," *in Proc. PICA*, pp. 116-122, 1983.

[20] H. Y. Min and N. R. Watson, "Torsional Interactions in Drivetrain System of Permanent Magnet Synchronous Generators Based Wind Farms," in *Proceedings of The IPST - International Conference on Power Systems Transients*, Seoul, Korea, 2017.

[21] M. Pavella, D. Ernst and D. Ruiz-Vega, *Transient Stability of Power Systems: A Unified Approach to Assessment*, Springer, USA, 2000, ISBN 978-1-4615-4319-0.

[22] T. Sun, Z. Chen, and F. Blaabjerg, "Transient stability of DFIG wind turbines at an external short-circuit fault," *Wind Energy*, vol. 8, Issue 3, July/September 2005, pp. 345-360.

[23] Q. Wu, Y. Sun, *Modeling and Modern Control of Wind Power*, Wiley-IEEE, 2018, ISBN 978-1-1192-3626-9.

[24] Bill Chun Piu Lau, Eden Wai Man Ma and M. Pecht, "Review of offshore wind turbine failures and fault prognostic methods," *Proceedings of the IEEE 2012 Prognostics and System Health Management Conference (PHM-2012 Beijing)*, Beijing, 2012, pp. 1-5.

[25] L. Bouzidi, "Wind power variability: Deterministic and probabilistic forecast of wind power production," in *Proceedings of the 2017 Saudi Arabia Smart Grid (SASG)*, Jeddah, 2017, pp. 1-7.

[26] H. E. Brown and C. L. DeMarco, “Synthetic inertia and small signal instability,” in *Proceedings of the 2016 North American Power Symposium (NAPS)*, Denver, CO, 2016, pp. 1-6.

[27] J. Hu, Q. Hu, B. Wang, H. Tang and Y. Chi, “Small Signal Instability of PLL-Synchronized Type-4 Wind Turbines Connected to High-Impedance AC Grid During LVRT,” in *IEEE Transactions on Energy Conversion*, vol. 31, no. 4, pp. 1676-1687, Dec. 2016.

[28] M. Sahni, D. Muthumuni, B. Badrzadeh, A. Gole and A. Kulkarni, “Advanced screening techniques for Sub-Synchronous Interaction in wind farms,” in *Proceedings of the PES T&D 2012*, Orlando, FL, 2012, pp. 1-9.

[29] R. Arrieta, M. A. Rios and A. Torres, “Contingency Analysis and Risk Assessment of Small Signal Instability,” in *Proceedings of the 2007 IEEE Lausanne Power Tech*, Lausanne, 2007, pp. 1741-1746.

[30] H. A. Mohammadpour and E. Santi, “Sub-synchronous resonance analysis in DFIG-based wind farms: Definitions and problem identification — Part I,” in *Proceedings of the 2014 IEEE Energy Conversion Congress and Exposition (ECCE)*, Pittsburgh, PA, 2014, pp. 812-819.

[31] “IEEE Standard Definitions in Power Operations Terminology,” in *IEEE Std 858-1993*, vol., no., pp.0_1-, 1993.

[32] “IEEE Guide for Synchronous Generator Modeling Practices in Stability Analyses,” in *IEEE Std 1110-1991*, vol., no., pp.1-96, 18 Nov. 1991.

[33] M. Zhang, Q. Li, C. Liu and J. Zhang, “An Aggregation Modeling Method of Large-scale Wind Farms in Power System Transient Stability Analysis,” in *Proceedings of the 2018 International Conference on Power System Technology (POWERCON)*, Guangzhou, 2018, pp. 1351-1356.

[34] Z. Liu, C. Liu, Y. Ding and G. Li, “Transient stability studies of power system with shared transmission of wind power and thermal power,” in *Proceedings of the 2nd IET Renewable Power Generation Conference (RPG 2013)*, Beijing, 2013, pp. 1-4.

[35] J. T. De Oliveira, M. F. De Medeiros and C. B. M. Oliveira, “Development of Modules for Transient Stability Studies of Power Systems with Wind Turbines in Different Simulation Platforms,” in *Proceedings of the 2006 IEEE/PES Transmission & Distribution Conference and Exposition: Latin America*, Caracas, 2006, pp. 1-6.

[36] H. Pingping, D. Ming and L. Binbin, “Study on transient stability of grid-connected large scale wind power system,” in *Proceedings of the 2nd International Symposium on Power Electronics for Distributed Generation Systems*, Hefei, 2010, pp. 621-625.

[37] S. Stanković and L. Söder, “Identification of reactive power provision boundaries of a distribution grid with DFIGs to a transmission grid,” in *Proceedings of the 2017 IEEE PES Innovative Smart Grid Technologies Conference Europe (ISGT-Europe)*, Torino, 2017, pp. 1-6.

[38] H. K. Karegar and S. Saberi, “Investigating of wind turbines effects on recloser operation in distribution networks,” in *Proceedings of the 2010 IEEE International Conference on Power and Energy*, Kuala Lumpur, 2010, pp. 523-526.

[39] M. Asmine *et al*., “Model Validation for Wind Turbine Generator Models, ” in *IEEE Transactions on Power Systems*, vol. 26, no. 3, pp. 1769-1782, Aug. 2011.

[40] P. Sørensen, B. Andresen, J. Fortmann and P. Pourbeik, “Modular structure of wind turbine models in IEC 61400-27-1, ” in *Proceedings of the 2013 IEEE Power & Energy Society General Meeting*, Vancouver, BC, 2013, pp. 1-5.

[41] M. Y. W. Teow, H. K. Chiu and R. H. G. Tan, “A computational modelling of wind turbine mechanical power and its improve factor determination,” in *Proceedings of the 4th IET Clean Energy and Technology Conference (CEAT 2016)*, Kuala Lumpur, 2016, pp. 1-8.

[42] M. Xu, T. Gu, J. Xu, K. Wang, G. Li and F. Guo, “Electromechanical Modeling of the Direct-Driven Wind Turbine Generator Considering the Stochastic Component of Wind Speed,” in *Proceedings of the 2018 2nd IEEE Conference on Energy Internet and Energy System Integration (EI2)*, Beijing, 2018, pp. 1-4.

[43] R. C. Portillo *et al*., “Modeling Strategy for Back-to-Back Three-Level Converters Applied to High-Power Wind Turbines,” in *IEEE Transactions on Industrial Electronics*, vol. 53, no. 5, pp. 1483-1491, Oct. 2006.

[44] J. Lee, K. Lee and F. Blaabjerg, “Open-Switch Fault Detection Method of a Back-to-Back Converter Using NPC Topology for Wind Turbine Systems,” in *IEEE Transactions on Industry Applications*, vol. 51, no. 1, pp. 325-335, Jan.-Feb. 2015.

[45] I. Jlassi and A. J. Marques Cardoso, “Fault-Tolerant Back-to-Back Converter for Direct-Drive PMSG Wind Turbines using Direct Torque and Power Control Techniques,” in *IEEE Transactions on Power Electronics*.

[46] Y. j. Ko, H. Jedtberg, G. Buticchi and M. Liserre, “Analysis of DC-Link Current Influence on Temperature Variation of Capacitor in a Wind Turbine Application,” in *IEEE Transactions on Power Electronics*, vol. 33, no. 4, pp. 3441-3451, April 2018.

[47] W. Hu, Z. Chen, Y. Wang and Z. Wang, “Flicker Mitigation by Active Power Control of Variable-Speed Wind Turbines With Full-Scale Back-to-Back Power Converters,” in *IEEE Transactions on Energy Conversion*, vol. 24, no. 3, pp. 640-649, Sept. 2009.

[48] J. Yao, H. Li, Y. Liao and Z. Chen, “An Improved Control Strategy of Limiting the DC-Link Voltage Fluctuation for a Doubly Fed Induction Wind Generator,” in *IEEE Transactions on Power Electronics*, vol. 23, no. 3, pp. 1205-1213, May 2008.

[49] R. F. M. Brandão, J. A. B. Carvalho and F. P. M. Barbosa, “Forced outage time analysis of a portuguese wind farm,” in *Proceedings of the 2009 44th International Universities Power Engineering Conference (UPEC)*, Glasgow, 2009, pp. 1-4.

[50] L. Cheng, J. Lin, Y. Sun, C. Singh, W. Gao and X. Qin, “A Model for Assessing the Power Variation of a Wind Farm Considering the Outages of Wind Turbines," in *IEEE Transactions on Sustainable Energy*, vol. 3, no. 3, pp. 432-444, July 2012.

[51] S. Sulaeman, M. Benidris, J. Mitra and C. Singh, “A wind farm reliability model considering both wind variability and turbine forced outages,” *2017 IEEE Power & Energy Society General Meeting*, Chicago, IL, 2017, pp. 1-1.

[52] S. Yang, Y. Wu, H. Lin and W. Lee, "Integrated Mechanical and Electrical DFIG Wind Turbine Model Development," in *IEEE Transactions on Industry Applications*, vol. 50, no. 3, pp. 2090-2102, May-June 2014.

[53] Devashish, A. Thakur, S. Panigrahi and R. R. Behera, "A review on wind energy conversion system and enabling technology," in *Proceedings of the 2016 International Conference on Electrical Power and Energy Systems (ICEPES)*, Bhopal, 2016, pp. 527-532.

[54] J. C. Das, *Understanding Symmetrical Components for Power System Modeling*. Wiley Online, 2016, pp. 103-105, ISBN: 9781119226895.

[55] R. K. Antar, "Multilevel inverter with unequal and selected DC voltage sources using modified absolute sinusoidal PWM technique," in *Proceedings of the 2018 1st International Scientific Conference of Engineering Sciences - 3rd Scientific Conference of Engineering Science (ISCES)*, Diyala, 2018, pp. 62-67.

[56] Y. A. I. Mohamed and E. F. El-Saadany, "A Control Scheme for PWM Voltage-Source Distributed-Generation Inverters for Fast Load-Voltage Regulation and Effective Mitigation of Unbalanced Voltage Disturbances," in *IEEE Transactions on Industrial Electronics*, vol. 55, no. 5, pp. 2072-2084, May 2008.

[57] X. Li, H. Zhang, M. B. Shadmand and R. S. Balog, "Model Predictive Control of a Voltage-Source Inverter With Seamless Transition Between Islanded and Grid-Connected Operations," in *IEEE Transactions on Industrial Electronics*, vol. 64, no. 10, pp. 7906-7918, Oct. 2017.

[58] A. Abdelhakim, P. Mattavelli, V. Boscaino and G. Lullo, "Decoupled Control Scheme of Grid-Connected Split-Source Inverters," in *IEEE Transactions on Industrial Electronics*, vol. 64, no. 8, pp. 6202-6211, Aug. 2017.

[59] M. R. J. Oskuee, M. Karimi, S. N. Ravadanegh and G. B. Gharehpetian, "An Innovative Scheme of Symmetric Multilevel Voltage Source Inverter With Lower Number of Circuit Devices," in *IEEE Transactions on Industrial Electronics*, vol. 62, no. 11, pp. 6965-6973, Nov. 2015.

[60] L. Guo, N. Jin, C. Gan, L. Xu and Q. Wang, "An Improved Model Predictive Control Strategy to Reduce Common-Mode Voltage for Two-Level Voltage Source Inverters Considering Dead-Time Effects," in *IEEE Transactions on Industrial Electronics*, vol. 66, no. 5, pp. 3561-3572, May 2019.

[61] L. Guo, X. Zhang, S. Yang, Z. Xie and R. Cao, "A Model Predictive Control-Based Common-Mode Voltage Suppression Strategy for Voltage-Source Inverter," in *IEEE Transactions on Industrial Electronics*, vol. 63, no. 10, pp. 6115-6125, Oct. 2016.

[62] R. Gurunathan and A. K. S. Bhat, "Zero-Voltage Switching DC Link Single-Phase Pulsewidth-Modulated Voltage Source Inverter," in *IEEE Transactions on Power Electronics*, vol. 22, no. 5, pp. 1610-1618, Sept. 2007.

[63] S. M. Seyyedzadeh and A. Shoulaie, "Accurate Modeling of the Nonlinear Characteristic of a Voltage Source Inverter for Better Performance in Near Zero Currents," in *IEEE Transactions on Industrial Electronics*, vol. 66, no. 1, pp. 71-78, Jan. 2019.

[64] D. Lu, X. Wang and F. Blaabjerg, "Impedance-Based Analysis of DC-Link Voltage Dynamics in Voltage-Source Converters," in *IEEE Transactions on Power Electronics*, vol. 34, no. 4, pp. 3973-3985, April 2019.

[65] E. Tetsuro and L. O. Chua, “Chaos from Phase-Locked Loops,” *IEEE Trans. Circuits Systems*, CAS-35(8), 987-1003.

[66] *Siemens D7 platform – 6.0-MW and 7.0-MW direct drive wind turbines*, available on the Available online: http://www.energy.siemens.com/hq/en/renewable-energy/wind-power/platforms/d7-platform/wind-turbine-swt-6-0-154.htm, Siemens AG, 2015.

[67] R. D. Middlebrook and S. Cuk, “A General Unified Approach to Modeling Switching-Converter Power Stages”, *IEEE Power Electronics Specialists Conference Records*, pp. 18-34, 1976.

[68] J. R. Orillaza, *Harmonic state space model of three phase thyristor controlled reactor*, PhD Thesis, University of Canterbury, New Zealand, 2012

[69] J. E. Ormrod, *Harmonic state-space modelling of voltage source converters*, MSc Thesis, University of Canterbury, New Zealand, 2013.

[70] S. P. Hwang, *Harmonic state-space modelling of an HVdc converter with closed-loop control*, PhD Thesis, University of Canterbury, New Zealand, 2013.

[71] M. Hwang, B. Das, A. Wood, N. Watson, and Y. Liu, “Experimental validation of the harmonic state-space model of a Graetz bridge converter,” *International Transactions on Electrical Energy System*, Vol. 24, Issue 9, pp. 1343-1355, Sept. 2014.

[72] S. R. Sanders, J. M. Noworolske, X. Z. Liu, and G.C. Verghese, “Generalized Averaging Method for Power Conversion Circuits,” *IEEE Transactions on Power Electronics*, vol. 6, No. 2, Apr. 1991.

[73] B. Lehmann and R.M. Bass, “Switching Frequency-Dependent Averaged Models for PWM DC-DC Converters,” *IEEE Transactions on Power Electronics*, vol. 11, No. 1, Jan. 1996.

[74] A. Semlyen, E. Acha, J. Arrillaga, "Newton-type algorithms for the harmonic phasor analysis of nonlinear power circuits in periodical steady-state with special reference to magnetic nonlinearities", *IEEE Trans. Power Delivery*, vol. 3, no. 3, pp. 1090-1097, July 1988.

[75] M. S.-P. Hwang, A. R. Wood, "A new modelling framework for power supply networks with converter based loads and generators - The harmonic state-space", *Proc. IEEE Int. Conf. Power Syst. Technol.*, pp. 1-6, 2012.

[76] G.C. Verghese, M. E. Elbuluk and J.G. Kassakian, "A general approach to sampled-data modeling for power electronic circuits," *IEEE Transactions on Power Electronics*, pp. 76-89, Apr. 1986.

[77] P. W. Lehn, "Exact modeling of the voltage source converter," in *IEEE Transactions on Power Delivery*, vol. 17, no. 1, pp. 217-222, Jan 2002. doi: 10.1109/61.974210.

[78] G. Valderrama, P. Mattavelli, and A. Stankovic, "Reactive power and unbalanced compensation using statcom with dissipativity-based control," 133, *IEEE Trans. on Control System Technology*, vol. 9, pp. 718–727, Sept. 2001.

[79] R. H. Park, "Two-Reaction Theory of Synchronous Machines: Generalized Method of Analysis - Part I," *Transactions of the AIEE*. 48: 716–730, 1929, (Retrieved December 13, 2012).

[80] T. Wildi, *Electrical Machines, Drives and Power Systems*, 6th Ed., ISBN: 9781292037325, Pearson, 2013.

[81] N. M. Wereley and S. R. Hall, "Frequency response of linear time-periodic systems," in *Proceedings of the 29th IEEE Conference on Decision and Control,* Honolulu, HI, 1990, pp. 3650-3655, vol. 6, doi: 10.1109/CDC.1990.203516

[82] J. B. Kwon, X. Wang, F. Blaabjerg, C. L. Bak, A. R. Wood and N. R. Watson, "Harmonic Instability Analysis of a Single-Phase Grid-Connected Converter Using a Harmonic State-Space Modeling Method," in *IEEE Transactions on Industry Applications*, vol. 52, no. 5, pp. 4188-4200, Sept.-Oct. 2016.

[83] M. Schroedl, "Sensorless control of AC machines at low speed and standstill based on the 'INFORM' method," in *Proc. Industrial Applications Conf. 31st IAS Annu. Meeting*, vol. 1. Oct. 1996, pp. 270–277.

[84] M. Linke, R. Kennel, and J. Holtz, "Sensorless position control of permanent magnet synchronous machines without limitation at zero speed," in *Proceedings of The 28th Annu. Conf. Ind. Electron. Soc.*, Nov. 2002, pp. 674–679.

[85] J. Ribrant and L. M. Bertling, "Survey of failures in wind power systems with focus on Swedish wind power plants during 1997–2005," *IEEE Trans. Energy Convers*., vol. 22, no. 1, pp. 167–173, Mar. 2007.

[86] T. Sebastian and G. R. Slemon. "Transient modeling and performance of variable-speed permanent-magnet motors." *IEEE Transactions on Industry Applications* 25.1 (1989): 101-106.

[87] N. Huang, "Simulation of power control of a wind turbine permanent magnet synchronous generator system," MS Thesis, Marquette University, USA, 2013.

[88] Z. Zhang, Y. Zhao, W. Qiao and L. Qu, "A discrete-time direct-torque and flux control for direct-drive PMSG wind turbines," *2013 IEEE Industry Applications Society Annual Meeting*, Lake Buena Vista, FL, 2013.

[89] R. Goebel and M. Subbotin, "Continuous-time linear quadratic regulator with control constrains via convex duality," *IEEE Trans. on Automatic Control*, vol. 52, no. 5, pp. 886–892, May 2007.

[90] J. J. Slotine and W. Li, *Applied Nonlinear Control*, Prentice-Hall, Englewood Cliffs, NJ, 1991.

[91] A. Kojima and M. Morari, "LQ control for constrained continuous-time systems," *Automatica*, vol. 40, no. 7, pp. 1143–1155, July 2004.

[92] S. W. H. De Haan and H. Huisman, "Novel operation and control modes for series-resonant converters," in *IEEE Transactions on Industrial Electronics*, vol. IE-32, no. 2, pp. 150-157, May 1985.

[93] D. P. Carroll, S. S. Abd-El-Hamid and F. Nozari, "A Simplified Analytical Model for a Current-Fed Force-Commutated Converter," in *IEEE Transactions on Industry Applications*, vol. IA-16, no. 4, pp. 501-513, July 1980.

[94] S. D. Sudhoff and O. Wasynczuk, "Analysis and average-value modeling of line-commutated converter-synchronous machine systems," in *IEEE Transactions on Energy Conversion*, vol. 8, no. 1, pp. 92-99, March 1993.

[95] C. -. Pan and T. -. Chen, "Modelling and analysis of a three phase PWM AC-DC convertor without current sensor," in *IEE Proceedings B - Electric Power Applications*, vol. 140, no. 3, pp. 201-208, May 1993.

[96] Yan-Fei Liu and P. C. Sen, "A general unified large signal model for current programmed DC-to-DC converters," in *IEEE Transactions on Power Electronics*, vol. 9, no. 4, pp. 414-424, July 1994.

[97] F. D. Rodriguez and J. E. Chen, "A refined nonlinear averaged model for constant frequency current mode controlled PWM converters," in *IEEE Transactions on Power Electronics*, vol. 6, no. 4, pp. 656-664, Oct. 1991.

[98] R. J. Dirkman, "Generalized state space averaging," in *Proceedings of the 1983 IEEE Power Electronics Specialists Conference*, Albuquerque, New Mexico, USA, 1983, pp. 283-294.

[99] D. Somayajula and M. Ferdowsi, "Small-signal modeling and analysis of the double-input buckboost converter," in *Proceedings of the 2010 Twenty-Fifth Annual IEEE Applied Power Electronics Conference and Exposition (APEC)*, Palm Springs, CA, 2010, pp. 2111-2115.

[100] M. Evzelman and S. Ben-Yaakov, "Average modeling technique for switched capacitor converters including large signal dynamics and small signal responses," in *Proceedings of the 2011 IEEE International Conference on Microwaves, Communications, Antennas and Electronic Systems (COMCAS 2011)*, Tel Aviv, 2011, pp. 1-5.

[101] M. Das and V. Agarwal, "Generalized small signal modeling of coupled inductor based high gain, high efficiency DC-DC converters," in *Proceedings of the 2015 IEEE Applied Power Electronics Conference and Exposition (APEC)*, Charlotte, NC, 2015, pp. 2691-2695.

[102] H. Prasad and T. Maity, "Design of a stable and efficient Z-source AC-AC converter using small signal analysis," in *Proceedings of the 2015 IEEE Power, Communication and Information Technology Conference (PCITC)*, Bhubaneswar, 2015, pp. 190-194.

[103] K. Khatun and A. K. Rathore, "Small Signal Modeling, Closed Loop Design, and Transient Results of Snubberless Naturally-Clamped Soft-Switching Current-Fed Half-bridge DC/DC Converter," in *Proceedings of the 2019 IEEE 28th International Symposium on Industrial Electronics (ISIE)*, Vancouver, BC, Canada, 2019, pp. 2571-2576.

[104] Z. Zhang, S. Tian and K. D. T. Ngo, "Small-Signal Equivalent Circuit Model of Quasi-Square-Wave Flyback Converter," in *IEEE Transactions on Power Electronics*, vol. 32, no. 8, pp. 5885-5888, Aug. 2017.

[105] D. Maksimovic and R. Zane, "Small-Signal Discrete-Time Modeling of Digitally Controlled PWM Converters," in *IEEE Transactions on Power Electronics*, vol. 22, no. 6, pp. 2552-2556, Nov. 2007.

[106] D. C. Hamill, J. H. B. Deane and D. J. Jefferies, "Modeling of chaotic DC-DC converters by iterated nonlinear mappings," in *IEEE Transactions on Power Electronics*, vol. 7, no. 1, pp. 25-36, Jan. 1992.

[107] S. Bacha, I. Munteanu, A. I. Bratu, *Power Electronic Converters Modeling and Control*, Springer, 2014.

[108] F. Blaabjerg, *Control of Power Electronic Converters And Systems – Volume I*, Academic Press, 2018.

[109] T. Suntio, T. Messo, and J. Puukko, *Power Electronic Converters: Dynamics and Control in Conventional and Renewable Energy Applications*, Weinheim, WILEY-VCH, 2018.

[110] P. C. Krause, "The Method of Symmetrical Components Derived by Reference Frame Theory," in *IEEE Transactions on Power Apparatus and Systems*, vol. PAS-104, no. 6, pp. 1492-1499, June 1985.

[111] W. Qiao, X. Yang and X. Gong, "Wind Speed and Rotor Position Sensorless Control for Direct-Drive PMG Wind Turbines," in *IEEE Transactions on Industry Applications*, vol. 48, no. 1, pp. 3-11, Jan.-Feb. 2012.

[112] M. E. Haque, Y. C. Saw and M. M. Chowdhury, "Advanced Control Scheme for an IPM Synchronous Generator-Based Gearless Variable Speed Wind Turbine," in *IEEE Transactions on Sustainable Energy*, vol. 5, no. 2, pp. 354-362, April 2014.

[113] W. Qiao, W. Zhou, J. M. Aller and R. G. Harley, "Wind Speed Estimation Based Sensorless Output Maximization Control for a Wind Turbine Driving a DFIG," in *IEEE Transactions on Power Electronics*, vol. 23, no. 3, pp. 1156-1169, May 2008.

[114] Z. Zhang, Y. Zhao, W. Qiao and L. Qu, "A Space-Vector-Modulated Sensorless Direct-Torque Control for Direct-Drive PMSG Wind Turbines," in *IEEE Transactions on Industry Applications*, vol. 50, no. 4, pp. 2331-2341, July-Aug. 2014.

[115] Y. Zhao, C. Wei, Z. Zhang and W. Qiao, "A Review on Position/Speed Sensorless Control for Permanent-Magnet Synchronous Machine-Based Wind Energy Conversion Systems," in *IEEE Journal of Emerging and Selected Topics in Power Electronics*, vol. 1, no. 4, pp. 203-216, Dec. 2013.

[116] M. Benadja and A. Chandra, "Adaptive Sensorless Control of PMSGs-Based Offshore Wind Farm and VSC-HVdc Stations," in *IEEE Journal of Emerging and Selected Topics in Power Electronics*, vol. 3, no. 4, pp. 918-931, Dec. 2015.

[117] X. T. Garcia, B. Zigmund, A. Terlizzi, R. Pavlanin, L. Salvatore, "COMPARISON BETWEEN FOC AND DTC STRATEGIES FOR PERMANENT MAGNET SYNCHRONOUS MOTORS," in *Proc. Advances in Electrical and Electronic Engineering*, Vol. 5, pp. 75-80. Mar. 2006.

[118] R. E. Ziemer, W. H. Tranter and D. R. Fannin, *Signals And Systems: Continuous And Discrete*, Pearson, ISBN 9781292026602, 2013.

[119] M. Anghel, F. Milano and A. Papachristodoulou, "Algorithmic Construction of Lyapunov Functions for Power System Stability Analysis," in *IEEE Transactions on Circuits and Systems I: Regular Papers*, vol. 60, no. 9, pp. 2533-2546, Sept. 2013.

[120] J. Kwon, X. Wang, C. L. Bak and F. Blaabjerg, "Analysis of harmonic coupling and stability in back-to-back converter systems for wind turbines using Harmonic State Space (HSS)," in *Proc. 2015 IEEE Energy Conversion Congress and Exposition (ECCE)*, Montreal, QC, 2015, pp. 730-737.

[121] J. R. C. Orillaza and A. R. Wood, "Reduced harmonic state space model of TCR," *Proceedings of 14th International Conference on Harmonics and Quality of Power - ICHQP 2010*, Bergamo, 2010, pp. 1-5.

[122] J. Lyu, X. Zhang, J. Huang, J. Zhang and X. Cai, "Comparison of Harmonic Linearization and Harmonic State Space Methods for Impedance Modeling of Modular

Multilevel Converter," in *Proc. 2018 International Power Electronics Conference (IPEC-Niigata 2018 -ECCE Asia)*, Niigata, 2018, pp. 1004-1009.

[123] A. C. Gondhalekar, *Strategies For Non-Liner System Identification*, PhD Thesis, Imperial College London, United Kingdom, 2009.

[124] Z. Sun and S. S. Ge, *Switched Linear Systems – Control and Design*, Springer, 2005, ISSN 0178-5354.

[125] B. M. Chen, Z. Lin and Y. Shamash, *Linear Systems Theory: A Structural Decomposition Approach*, Berlin, Springer, 2004, ISBN 0-8176-3779-6.

[126] W. J. Rugh, *Nonlinear System Theory: The Volterra/Wiener Approach*, Johns Hopkins University Press, Baltimore, 1981.

[127] E. Mostacciuolo, F. Vasca and S. Baccari, "Differential Algebraic Equations and Averaged Models for Switched Capacitor Converters with State Jumps," in *IEEE Transactions on Power Electronics*, vol. 33, no. 4, pp. 3472-3483, April 2018.

[128] P. Drąg and K. Styczeń, "A new procedure for solving differential-algebraic equations," in *Proc. 2019 20th International Carpathian Control Conference (ICCC)*, Krakow-Wieliczka, Poland, 2019, pp. 1-5.

[129] Shun-Hsien Huang, John Schmall, Jose Conto, John Adams, Yang Zhang, Cathey Carter, "Voltage control challenges on weak grids with high penetration of wind generation: ERCOT experience", in *Proc. Power and Energy Society General Meeting 2012 IEEE*, pp. 1-7, 2012.

[130] L. Trajković, “Nonlinear Circuits,” in Electrical Engineering Handbook, Academic Press, 2005, pp. 75-81, ISBN 9780121709600,

[131] Byeong Rim Jo, Hee Wook Ahn and Myung Joong Youn, "Multi-variable sliding mode control of quantum boost SRC," in *IEEE Transactions on Control Systems Technology*, vol. 2, no. 2, pp. 148-150, June 1994.

[132] P. Singh and S. Purwar, "Sliding mode controller for PWM based Buck-Boost DC/DC converter as state space averaging method in continuous conduction mode," in *Proc. 2012 2nd International Conference on Power, Control and Embedded Systems*, Allahabad, 2012, pp. 1-5.

[133] J. Mahdavi, A. Emadi and H. A. Toliyat, "Application of state space averaging method to sliding mode control of PWM DC/DC converters," in *Proc. IAS '97. Conference Record of the 1997 IEEE Industry Applications Conference Thirty-Second IAS Annual Meeting*, New Orleans, LA, USA, 1997, pp. 820-827 vol.2.

[134] Zhou Yue, "Study of buck-boost photovoltaic inverter based on discrete sliding mode control strategy," in *Proc. 2011 Second International Conference on Mechanic Automation and Control Engineering*, Hohhot, 2011, pp. 1643-1647.

[135] J. Mahdavi, M. R. Nasiri, A. Agah and A. Emadi, "Application of neural networks and State-space averaging to DC/DC PWM converters in sliding-mode operation," in *IEEE/ASME Transactions on Mechatronics*, vol. 10, no. 1, pp. 60-67, Feb. 2005.

[136] L. Fingersh, M. Hand, and A. Laxson, "Wind Turbine Design Cost and Scaling Model," Technical Report, NREL/TP-500-40566, December 2006.

[137] J. F. Manwell, J. G. McGowan, and A. L. Rogers, *Wind energy explained: Theory, Design and Application*. John Wiley & Sons, 2010.

[138] M. H. Hansen, A. Hansen, T. J. Larsen, S. Øye, P. Sørensen, and P. Fuglsang, "Control design for a pitch-regulated, variable speed wind turbine," Risø National Laboratory, Roskilde, Denmark, Tech. Rep. Risø-R-1500(EN), Jan. 2005.

[139] J. S. Rao, Rotor dynamics, New Age International, pp. 37-40, 1996.

[140] F. Wahl, G. Schmidt, and L. Forrai, "On the Significance of Antiresonance Frequencies in Experimental Structural Analysis", Journal of Sound and Vibration, vol. 219(3), pp. 379–394, 1999.

[141] L. Y. Pao and K. E. Johnson, "A Tutorial on the Dynamics and Control of Wind Turbines and Wind Farms," Proc. Amer. Ctrl. Conf., June 2009.

[142] IEEE Committee Report, "Terms, Definitions and Symbols for Subsynchronous Oscillations", in *IEEE Trans. Power Apparatus and Systems*, vol. PAS-104, no. 6, pp. 1326-1334, June 1985.

[143] J. Bladh, P. Sundqvist and U. Lundin, "Torsional Stability of Hydropower Units Under Influence of Subsynchronous Oscillations," in *IEEE Transactions on Power Systems*, vol. 28, no. 4, pp. 3826-3833, Nov. 2013.

[144] S. Rehman, Md. M. Alam and L. M. Alhems, "A review of wind-turbine structural stability, failure and alleviation," in *Adv. In Civil, Environ. & Mat Research ACEM*, August 2018.

[145] L. W. Cai, *Fundamentals of Mechanical Vibrations*, John Wiley & Sons, 2016, p. 307-313.

[146] L. Zhang, D. Hu, D. Jiang, D. Zhao and Y. Liu, "Modeling and implementation of direct-drive permanent magnet wind turbine based on generator parameter conversion," in *Proc. 2015 5th International Conference on Electric Utility Deregulation and Restructuring and Power Technologies (DRPT)*, Changsha, 2015, pp. 1948-1953.

[147] M. Rashid, *Power Electronics Handbook*, 3rd Ed., Elsevier, Inc., 2011, ISBN 978-0-12-382036-5.

[148] M. Brenna, F. Foiadelli and D. Zaninelli, "The Impact of The Wind Generation Connected to Weak Grids," in *Proc. 2008 International Symposium on Power Electronics, Electrical Drives, Automation and Motion*, Ischia, 2008, pp. 1481-1485.

[149] Y. Huang, X. Zhai, J. Hu, D. Liu and C. Lin, "Modeling and Stability Analysis of VSC Internal Voltage in DC-Link Voltage Control Timescale," in *IEEE Journal of Emerging and Selected Topics in Power Electronics*, vol. 6, no. 1, pp. 16-28, March 2018.

[150] Y. Wang J. Meng X. Zhang L. Xu "Control of PMSG-based wind turbines for system inertial response and power oscillation damping," *IEEE Trans. Sustainable Energy*, vol. 6 no. 2 pp. 565-574 Jan. 2015.

[151] A. Yazdani and R. Iravani, *Voltage-sourced converters in power systems – Modeling, control, and applications*, John Wiley & Sons, New Jersey, 2010.

[152] M. Castilla J. Miret A. Camacho L. G. Vicuna J. Matas "Modeling and design of voltage support control scheme for three-phase inverters operating under unbalanced grid conditions" *IEEE Trans. Power Electron*. vol. 29 no. 11 pp. 6139-6150 Nov. 2014.

[153] H. Geng D. Xu B. Wu G. Yang "Unified power control for PMSG based WECS operating under different grid conditions" *IEEE Trans. Energy Conversion,* vol. 26 no. 3 pp. 822-830 Sep. 2011.

[154] Z. Zhang Y. Zhao W. Qiao L. Qu "A discrete-time direct torque control for direct-drive PMSG-based wind energy conversion systems" in *IEEE Trans. Industry Applications,* vol. 51 no. 4 pp. 3504-3514 Jul./Aug. 2015.

[155] I. Erlich *et al*., "New Control of Wind Turbines Ensuring Stable and Secure Operation Following Islanding of Wind Farms," in *IEEE Transactions on Energy Conversion*, vol. 32, no. 3, pp. 1263-1271, Sept. 2017.

[156] J. D. Ainsworth, "Harmonic instability between controlled static convertors and a.c. networks," in *Proceedings of the Institution of Electrical Engineers*, vol. 114, no. 7, pp. 949-957, July 1967.

[157] J. D. Ainsworth, "The Phase-Locked Oscillator-A New Control System for Controlled Static Convertors," *IEEE Trans. on Power Appar. and Systems*, Vol. PAS-87, No. 3, March 1968.

[158] J. R. Macedo, J. W. Resende, C. A. Bissochi, D. Carvalho and F. C. Castro, "Proposition of an interharmonic-based methodology for high-impedance fault detection in distribution systems," *IET Generation, Transmission & Distribution*, vol. 9, no. 16, pp. 2593-2601, 3 12 2015.

[159] Ö. Göksu, R. Teodorescu, C. L. Bak, F. Iov and P. C. Kjær, "Instability of Wind Turbine Converters During Current Injection to Low Voltage Grid Faults and PLL Frequency Based Stability Solution," in *IEEE Transactions on Power Systems*, vol. 29, no. 4, pp. 1683-1691, July 2014.

[160] G. D. Irwin, A. K. Jindal, A. L. Issacs, "Sub-synchronous control interaction between type 3 wind turbines and series compensated AC transmission systems", *Proc. 2011 IEEE PES General Meeting*, pp. 1-6.

[161] P. Midya, and P. T. Krein, “Noise properties of pulsewidth-modulated power converters - Open-loop effects,” in *IEEE Trans. Power Electronics*, vol. 15, pp. 1134-1143, Nov. 2000.

[162] S. R. Sanders, "On limit cycles and the describing function method in periodically switched circuits", *IEEE Trans. Circuits and Systems I: Fundamental Theory and Applications*, vol. 40, no. 9, pp. 564-572, Sept. 1993.

[163] D. Diallo, G. Champenois and J. -. Rognon, "Two management strategies to deal with PWM inverter's control variable saturation", *IEEE Trans. Industry Applications*, vol. 30, no. 3, pp. 717-722, May-June, 1994.

[164] M. F. M. Arani and Y. A. I. Mohamed, "Analysis and Mitigation of Undesirable Impacts of Implementing Frequency Support Controllers in Wind Power Generation," in *IEEE Transactions on Energy Conversion*, vol. 31, no. 1, pp. 174-186, March 2016.

[165] B. Kasztenny and J. Rostron, "Circuit breaker ratings — A primer for protection engineers," in *Proc. 2018 71st Annual Conference for Protective Relay Engineers (CPRE)*, College Station, TX, 2018, pp. 1-13.

[166] J. Adams, C. Carter, S. -H. Huang, "ERCOT experience with subsynchronous control interaction and proposed remediation", in *Proc. IEEE PES Transmiss. Distrib. Conf. Expo.*, pp. 1-5, 2012.

[167] J. Adams, V. A. Pappu and A. Dixit, "Ercot experience screening for Sub-Synchronous Control Interaction in the vicinity of series capacitor banks," *2012 IEEE Power and Energy Society General Meeting*, San Diego, CA, 2012, pp. 1-5.

[168] F. Iov and F. Blaabjerg, "Power electronics and control for wind power systems," in *Proc. 2009 IEEE Power Electronics and Machines in Wind Applications*, Lincoln, NE, 2009, pp. 1-16.

[169] L. Sainz, L. Monjo, J. Pedra, M. Cheah-Mane, J. Liang and O. Gomis-Bellmunt, "Effect of wind turbine converter control on wind power plant harmonic response and resonances," in *IET Electric Power Applications*, vol. 11, no. 2, pp. 157-168, 2017.

[170] S. K. Chaudhary, R. Teodorescu, P. Rodriguez and P. C. Kjaer, "Control and operation of wind turbine converters during faults in an offshore wind power plant grid with VSC-HVDC connection," In *Proc. 2011 IEEE Power and Energy Society General Meeting*, Detroit, MI, USA, 2011.

[171] D. Zhang and K. J. Tseng, "Design and modelling of grid-connected PMSG-based wind energy conversion through diode rectifier, DC/DC and DC/AC converters," in *Proc. 2014 Australasian Universities Power Engineering Conference (AUPEC)*, Perth, WA, 2014.

[172] Y. Wang, C. Wang, Z. Liu, X. Song, L. Wang and Q. Jiang, "STATCOM-Based SSCI Mitigation Algorithm for DFIG-Based Wind Farms," in *Proceedings of the 2018 IEEE International Power Electronics and Application Conference and Exposition (PEAC)*, Shenzhen, 2018

[173] H. K. Nia, F. Salehi, M. Sahni, N. Karnik and H. Yin, "A filter-less robust controller for damping SSCI oscillations in wind power plants," in *Proc. 2017 IEEE Power & Energy Society General Meeting*, Chicago, IL, 2017.

[174] X. Xie, W. Liu, H. Liu, Y. Du and Y. Li, "A System-Wide Protection Against Unstable SSCI in Series-Compensated Wind Power Systems," in *IEEE Transactions on Power Delivery*, vol. 33, no. 6, pp. 3095-3104, Dec. 2018.

[175] G. Revel and D. M. Alonso, "Subsynchronous control interactions in power systems with several wind farms," in *Proc. 2017 XVII Workshop on Information Processing and Control (RPIC)*, Mar del Plata, 2017.

[176] M. Ghafouri, U. Karaagac, J. Mahseredjian and H. Karimi, "SSCI Damping Controller Design for Series-Compensated DFIG-Based Wind Parks Considering Implementation Challenges," in *IEEE Transactions on Power Systems*, vol. 34, no. 4, pp. 2644-2653, July 2019.

[177] Integrating Inverter Based Resources into Low Short Circuit Strength Systems – Reliability Guideline, NERC, December 2007.

[178] T. G. Kincaid and R. C. Rustay, "Complex signal theory and the cross-correlation of two nonstationary signals," in *Proceedings of the IEEE*, vol. 57, no. 6, pp. 1198-1198, June 1969.

[179] S. Haykin, *Kalman Filtering and Neural Networks*, Vol. 47, John Wiley & Sons, Hoboken, 2004.

[180] P. Zarchan and H. Musoff, *Fundamentals of Kalman Filtering: A Practical Approach,* Progress in Astronautics and Aeronautics Series Vol. 246, 3rd ed., American Institute of Aeronautics and Astronautics, Virginia, USA. 2015. Pp 579-595, ISBN 978-1-62410-276-9.

[181] Wan, E. A., and R. van der Merwe, *The Unscented Kalman Filter for Nonlinear Estimation*, in *Proceedings of Symposium 2000 on Adaptive Systems for Signal Processing, Communication and Control (AS-SPCC)*, IEEE Press, 2000.

[182] IEC Standard 60871-1, *Shunt capacitors for AC power systems having a rated voltage above 1 000 V - Part 1: General*, International Electrotechnical Committee, May 2014.

[183] ANSI/IEEE Standard C37.99, *IEEE Guide for the Protection of Shunt Capacitor Banks*, IEEE Press, 2012.

[184] Feng Wu, Xiao-Ping Zhang and Ping Ju, "Modeling and control of the wind turbine with the Direct Drive Permanent Magnet Generator integrated to power grid," in *Proc. 2008 Third International Conference on Electric Utility Deregulation and Restructuring and Power Technologies*, Nanjing, 2008, pp. 57-60.

[185] F. Wu, X. P. Zhang, K. Godfrey and P. Ju, "Small signal stability analysis and optimal control of a wind turbine with doubly fed induction generator," in *IET Generation, Transmission & Distribution*, vol. 1, no. 5, pp. 751-760, September 2007.

[186] J. Hu, H. Yuan and X. Yuan, "Modeling of DFIG-Based WTs for Small-Signal Stability Analysis in DVC Timescale in Power Electronized Power Systems," in *IEEE Transactions on Energy Conversion*, vol. 32, no. 3, pp. 1151-1165, Sept. 2017.

[187] M. Zhao, X. Yuan and J. Hu, "Modeling of DFIG Wind Turbine Based on Internal Voltage Motion Equation in Power Systems Phase-Amplitude Dynamics Analysis," in *IEEE Transactions on Power Systems*, vol. 33, no. 2, pp. 1484-1495, March 2018.

[188] J. Morató, T. Knüppel and J. Østergaard, "Residue-Based Evaluation of the Use of Wind Power Plants With Full Converter Wind Turbines for Power Oscillation Damping Control," in *IEEE Transactions on Sustainable Energy*, vol. 5, no. 1, pp. 82-89, Jan. 2014.

[189] D. Gautam, V. Vittal and T. Harbour, "Impact of Increased Penetration of DFIG-Based Wind Turbine Generators on Transient and Small Signal Stability of Power Systems," in *IEEE Transactions on Power Systems*, vol. 24, no. 3, pp. 1426-1434, Aug. 2009.

[190] R. C. Portillo, M. M. Prats, J. I. León, J. A. Sanchez, J. M. Carrasco, E. Galvan, et al., "Modeling strategy for back-to-back three-level converters applied to high-power wind turbines," in *IEEE Transactions on industrial electronics*, vol. 53, pp. 1483-1491, 2006.

[191] J. Ruan *et al*., "Transient Stability of Wind Turbine Adopting a Generic Model of DFIG and Singularity-Induced Instability of Generators/Units With Power–Electronic Interface," in *IEEE Transactions on Energy Conversion*, vol. 30, no. 3, pp. 1069-1080, Sept. 2015.

[192] J. Wang and Y. Yu, "Chaotic Oscillation Control in Power System based on Adaptive Linear Feedback Sliding Mode Control," in *Proceedings of the 2018 Chinese Automation Congress (CAC)*, Xi'an, China, 2018, pp. 3384-3388.

[193] Leonov G.A.; Kuznetsov N.V. (2013). "Hidden attractors in dynamical systems. From hidden oscillations in Hilbert–Kolmogorov, Aizerman, and Kalman problems to hidden chaotic attractor in Chua circuits," *International Journal of Bifurcation and Chaos*, 23 (1): art. no. 1330002, 2010.

[194] Bill Chun Piu Lau, Eden Wai Man Ma and M. Pecht, "Review of offshore wind turbine failures and fault prognostic methods," in *Proceedings of the IEEE 2012 Prognostics and System Health Management Conference (PHM-2012 Beijing)*, Beijing, 2012, pp. 1-5.

[195] S. Grunau and F. W. Fuchs, "Effect of Wind-Energy Power Injection into Weak Grids," in *Annual Proceedings of the European Wind Energy Association*, 2012.

[196] X. Tang, M. Yin, C. Shen, Y. Xu, Z. Y. Dong and Y. Zou, "Active Power Control of Wind Turbine Generators via Coordinated Rotor Speed and Pitch Angle Regulation," in *IEEE Transactions on Sustainable Energy*, vol. 10, no. 2, pp. 822-832, April 2019.

APPENDIX I

WT and PMSG Specifications

TABLE A.1: WT SIMULATION PARAMETERS

Parameters	Value	Unit
Blade Length	37.5	m
Rated Speed	23	rpm
Inertia	6.34 x 10^6	kg·m^2
Viscous Friction	0.008	N·m·s
Viscous Damping	0.114	N·m/s
Wind Speed	12.0	m/s

TABLE A.2: PMSG SIMULATION PARAMETERS (CASE 1 TO 4)

Parameters	Value	Unit
Rated Power	2.0	MW
Efficiency	92	%
Terminal Voltage (L-L)	690	V
Rated Stator Current	1870	A
Pole Pairs	62	
Inertia	3.47 x 10^6	kg·m^2
Viscous Damping	0.1	N·m·s
Terminal Voltage	690	V
Rated Stator Current	1870	A
Stator Resistance	1.85	p.u
Inductance: X_d, X_d' X_d'' X_q X_q' X_q'' X_l	1.81, 0.3, 0.23, 1.76, 0.65, 0.25, 0.15	p.u

APPENDIX II

Drivetrain Simulation Data

DRIVETRAIN SIMULATION PARAMETERS

$$K = \frac{1}{8.2 \times 10^{6}}$$

$$\tau = 5.28 \times 10^{-4}$$

$$\zeta_R = 4.295 \times 10^{-4}$$

$$\omega_{AR} = 1.302\ rad/s$$

$$\omega_R = 1.627\ rad/s$$

$$\omega_d = \omega_R\sqrt{1-\zeta_R} = 1.302\ rad/s$$

TABLE A.3: SHAFT PARAMETERS

Parameters	Value	Unit
Shaft Stiffness	flexible: 5.9×10^{6} rigid: 6.2×10^{10}	N·m
Damping	3.1×10^{3}	N·m·s

APPENDIX III

Control Parameters

Reference Signal i_{syn_dq} Calculation

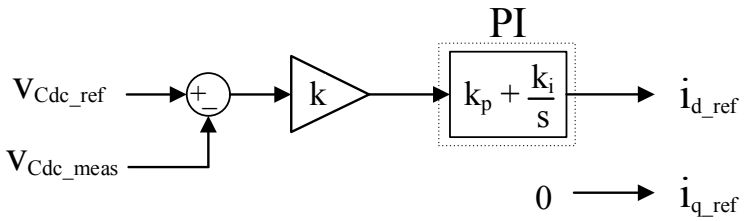

Figure A.1: Reference current, i_{dq_syn} generation block diagram.

$$k = \frac{10}{v_{Cdc\_rated}} \approx 0.007246$$

$$K_p = 1.1$$

$$K_i = 27.5$$

VSI Control Parameters

$$K_p = 1.0$$

$$K_i = 50$$

PWM frequency = 3000 Hz

VAR Regulator of VSI

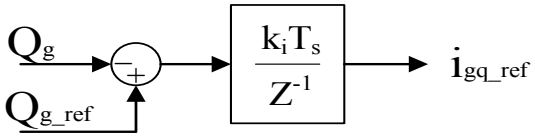

Figure A.2: VAR regulator block diagram

$$K_i = 0.05$$

MSC Control Parameters

PWM frequency = 1650 Hz

Kp=0.1361

Ki=2.7221

K=0.5131

MSC Control Parameter Limits

From the Equation (3.29),

$$T_{pm\_EM} = K\omega_s^2$$

where T_{pm_EM} = electromagnetic PMSG torque to be controlled, K = control gain, which is given in Equation (3.30), and ω_s = the speed of the PMSG rotor.

From the Equation (3.30),

$$K = \frac{1}{2}\rho\pi R^5 \left(\frac{C_{p\_max}}{\lambda_{pm^*}^3}\right)$$

Assuming $\omega_{s\_ref} = \omega_{s\_meas}$, the torque control given by Equations (3.29) and (3.30) can be expressed [196] with a 1DOF system:

$$\frac{d\omega_s}{dt} = \frac{1}{I_{pm}}\left(T_{wt} - T_{pm}\right)$$

Combining Equations (3.1), (3.4), (3.5), (3.29), and (3.30) gives:

$$\frac{d\omega_s}{dt} = \frac{1}{2I_{pm}}\rho\pi R^5\omega_s^2\left(\frac{C_{p\_meas}}{\lambda_{pm}^3} - \frac{C_{p\_max}}{\lambda_{pm^*}^3}\right)$$

Thus, the limiting conditions of the speed of the PMSG rotor are expressed:

$$\frac{d\omega_s}{dt} < 0 \quad \rightarrow \quad C_{p\_meas} < \frac{C_{p\_max}}{\lambda_{pm^*}^3}\lambda_{pm}^3$$

$$\frac{d\omega_s}{dt} > 0 \quad \rightarrow \quad C_{p\_meas} > \frac{C_{p\_max}}{\lambda_{pm^*}^3}\lambda_{pm}^3$$

PLL Parameters

$$K_p = 4.1$$

$$K_i = 25$$

APPENDIX IV

Simulation Environment

TABLE A.4: SIMULATION PARAMETERS

Parameters	Value	Unit
Simulation sample time	50	μs
UKF sample time	500	μs
Control computation delay	2	ms
CB mechanical actuation delay (three-phase, 0.5 cycle)	5	ms
Crowbar protection setting	ON: 15 OFF: 5	%
Solver type	fixed step – discrete	

APPENDIX V

Angular Momentum Function

The definition of the angular momentum of the WT rotor

$$\Delta L = \int T_{wt} = f_{T_{wt}}\left(\frac{d\theta_{wt}}{dt}\right)$$

From Equation (4.5),

$$I_{pm}\frac{d^2\theta}{dt^2} = \frac{1}{I_{wt}}T_{wt} - \frac{I_{wt}+I_{pm}}{I_{wt}I_{pm}}C_{sh}\theta$$

$$I_{pm}\frac{d^2\theta}{dt^2} + \frac{I_{wt}+I_{pm}}{I_{wt}I_{pm}}C_{sh}\theta = \frac{1}{I_{wt}}T_{wt}$$

$$I_{pm}I_{wt}\frac{d^2\theta}{dt^2} + I_{wt}\frac{I_{wt}+I_{pm}}{I_{wt}I_{pm}}C_{sh}\theta = T_{wt}$$

$$I_{pm}I_{wt}\int\frac{d^2\theta}{dt^2} + I_{wt}\frac{I_{wt}+I_{pm}}{I_{wt}I_{pm}}C_{sh}\int\theta = \int T_{wt}$$

Let $\Gamma = I_{pm}I_{wt}$,

$$\Gamma\left[\frac{d\theta}{dt} + constant_1\right] + I_{wt}\frac{I_{wt}^2+\Gamma}{\Gamma}C_{sh}\left[\frac{1}{2}\theta^2 + constant_2\right] = \Delta L$$

The constant terms can be added.

$$\underbrace{\Gamma\frac{d\theta}{dt}}_{1^{st}\text{ order numerical integration}} + \underbrace{I_{wt}\frac{I_{wt}^2+\Gamma}{2\Gamma}C_{sh}\theta^2}_{\text{Constant} = \eta_1} + \underbrace{constant_{1+2}}_{\text{Constant} = \eta_2} = \Delta L$$

Thus, the function of angular momentum is defined in terms of the WT speed.

$$\Gamma\frac{d\theta}{dt} + \eta_1\theta^2 + \eta_2 = \Delta L$$